Floating Solar

A hydroelastic method

T.A. Beinema

Floating Solar

A hydroelastic method

by

T.A. Beinema

to obtain the degree of Master of Science
at Delft University of Technology

Student number:	4250206	
Project duration:	February 1, 2021 – April 26, 2022	
Thesis committee:	Dr. -Ing. S. Schreier,	TU Delft
	Dr. H. Seyffert,	TU Delft
	Dr. O. Colomes-Gene,	TU Delft
	Ing. B. Van den Berg,	Bluewater Energy Services, supervisor
	Ir. V. Pels,	Bluewater Energy Services, supervisor

TU Delft

Summary

Bluewater Energy Services BV. (Bluewater) participates in a Joint Industry Project (JIP) called Solar@SeaII which is focussed on the development of a flexible floating PV structure and mooring line system for application at sea. This structure allows for countries with a high population density to move their renewable energy production to sea.

The JIP structure is designed to negate the difficulties found for Very Large Floating Structure (VLFS) in terms of manufacturing, transport and installation. This goal is pursued in the form of smaller inflatable flexible floating structures. The structure is constructed from a lightweight flexible material, thin PV film is applied to the top surface, and hoops at the fairlead positions are added to allow for connection to the mooring line solution. Combining multiple structures of this kind would allow for the same operational PV footprint as a VLFS, without the previously mentioned difficulties.

The interaction of the flexible structure, the water, and the mooring line system leads to a complex system response to the environmental forces. To design a mooring line system the motions of the fairlead points need to be determined. The theory describing the interaction between the structural behavior and fluid named hydroelasticity, is a relatively new concept. The two-way interaction between the mooring line system and a flexible structure has not been found to be implemented yet. Bluewater is therefore interested in the development of a method that is able to model this complex interaction. The numerical method described in the thesis focuses on the development of a numerical model that is able to determine the motions of the flexible structure at the fairlead points. In the development of this method the interaction with the mooring line system is researched and taken into account, but not implemented. The method should be computationally efficient and accurate enough for the initial design stages of the combined mooring line and structure system.

To achieve the complex interaction, ANSYS APDL code is used in Python to determine the structural mesh via the Finite Element Method (FEM). The hydrostatic and hydrodynamic interaction of the fluid and structure is determined by means of a lower order frequency domain panel method (BEM) by Katz and Plotkin, and implementation of the script provided by Telste and Noblesse. The mooring line system is to be modelled via the OrcFxAPI by OrcaFlex. The intended two-way interaction of the floating structure and the mooring line system is pursued by allowing for coupling the system at the location of the fairlead points of the system. The method can be considered a FEM-BEM solution to the coupled problem, and valid for deep water situations.

The fluid-structure interaction of the numerical method is verified for the structural mass and stiffness matrices. The implementation of the deep water regular wave in the method is verified by comparing it with analytical values. The hydrostatic stiffness is verified by comparing the response of the structure to a long-crested wave. The difference in phase and peak time between measurement points is used to determine the correct implementation of the measurement method in the model. A convergence test is executed for the coefficients of the added mass, damping and exciting wave force coefficients. The coefficient for the added mass was compared to one calculated with the program HydroSTAR. The method performed well for these individual tests.

The numerical method is validated by comparing the numerical result with experimentally determined responses of a 1:1 scale JIP structure to incident regular deep water waves as measured by MARIN. Suitable deep water test cases were determined from the MARIN data. The undisturbed numerical wave was compared with the undisturbed deep water wave as measured by MARIN. Finally, three test cases were selected for the validation of the interaction of the structure and the wave.

The first test case, consisted of a wave almost twice the length of the structure. The numerical method was able to model the global dominated motion within an error range of 12 percent depending on the location of the measurement points. The second test case consisted of a wave slightly shorter than the structure, local deformation effects were expected and found. From the test data a distortion of the wave, both in terms of amplitude and wavelength due to structure interaction was found. This effect is likely caused by the ballast bags and the stiffness of the structure. The increase and decrease in amplitude is more pronounced closer to the center of the structure. The last test case consisted of very short waves with respect to the length of the structure. The numerical method had a large error with respect to experimental results. This error is likely due the nonlinear interaction of the ballast bags. This could not be confirmed from the available MARIN data.

The work as presented in this thesis is part of a larger intended method which is not finished yet. Satisfactory results were found for the components considered in the verification. The validation provided some points for improvement for the current numerical method. In general, the work done provides a foundation for future work. As it is possible to determine the reaction of the structure to longer than structure waves, which can be expected at sea.

The recommendations for future work are therefore as follows. The influence of the ballast bags needs to be researched further as it likely has significant impact on higher wave frequency motions. The structure is currently meshed in ANSYS by means of SOLID186 elements, it is expected that implementation of shell elements can result in a computationally more efficient method.

Contents

List of Figures

List of Tables

1

Introduction

1.1. Renewable energy technologies

Due to climate agreements, such as the Paris Agreement [65] and the European Green Deal [10], countries need to reduce their carbon footprint and increase their renewable energy production. As a result of this increased and persisting demand for renewable energy, the interest in and innovation of renewable energy technologies has increased considerably over the last decade [13].

For countries with a high population density, energy projects based on for example photovoltaics and wind turbines take up valuable landmass [53], [64] and [41]. Wind turbines have therefore shifted towards application at sea and now photovoltaics (PV) is in the process of doing the same.

The recent innovation in floating PV structures has resulted in a broad range in concepts and realized designs for offshore PV. These designs can roughly be divided into three distinct groups: the rigid body single structure, a multi-body rigid structure, and flexible structures. An example for the rigid body single structure is the system by Nemo Eng, which relies on a metal frame on which the PV panels are mounted, see Figure 1.1a. An example for the multi-body rigid structure is the design by Solaris, see Figure 1.1b. Examples of flexible structures are more scarce, but Ocean Sun has implemented a design using a flexible membrane, see Figure 1.1c.

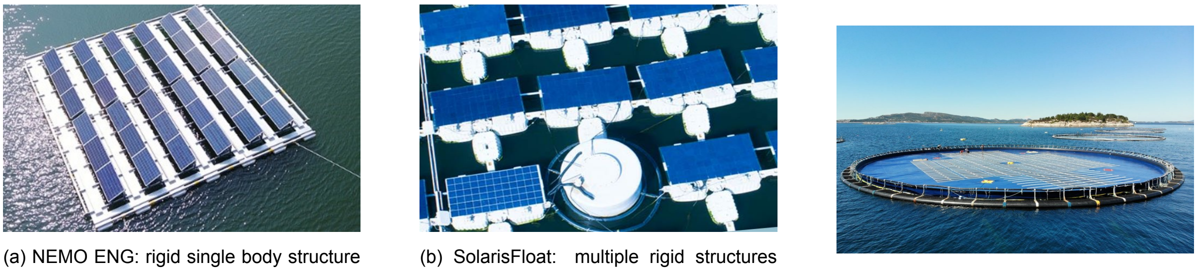

(a) NEMO ENG: rigid single body structure [36]

(b) SolarisFloat: multiple rigid structures [54]

(c) Ocean sun: flexible membrane [39]

Figure 1.1: Floating solar varying design types

Depending on the structure characteristics and dimensions, floating structures can exhibit very different behavior.

1.2. Bluewater Energy Services

Bluewater Energy Services (from here on referred to as Bluewater) provides services and products in the offshore market. The products and services consist of chartering Floating Production Storage and Offloading vessels (FPSOs), design of Single Point Mooring (SPM) tower systems and Turret Mooring Systems (TMS), mooring systems, and renewable energy solutions such as floating wind turbine systems.

Bluewater is participating in a Joint Industry Project (JIP) named Solar@SeaII. The goal of this project is the development of a flexible photovoltaic structure and mooring line system that can operate at sea. The manufacturing, transport and installation issues as found for very large floating structures (VLFS) have prompted the design of a smaller flexible floating structure. Figure 1.2 shows the flexible system as designed and installed by the JIP partners.

Figure 1.2: Solar@SeaII design [38]

The structure is constructed with a flexible material. Thin photovoltaic film is applied to the top surface of the structure and ballast bags are added to the outer edges of the bottom of the structure. The structure has longitudinal and transverse dimensions much smaller than those considered in VLFSs. Figure 1.3 shows a top view (left) and side view (right) of the structure.

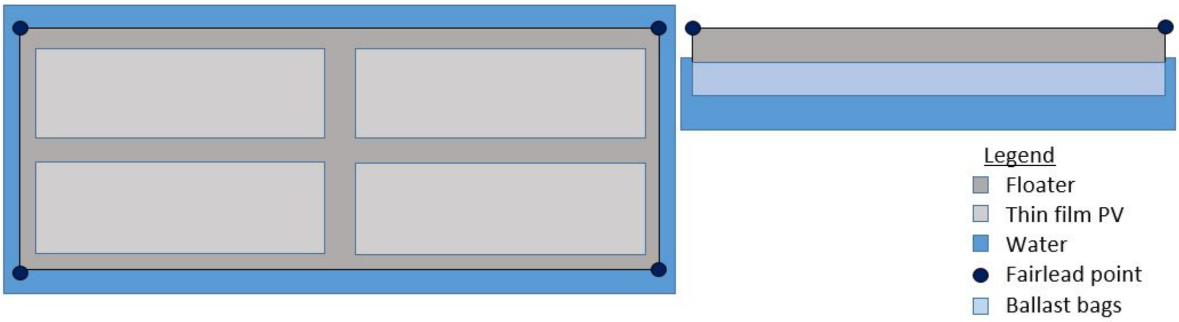

Figure 1.3: Overview Solar@SeaII Joint Industry Project structure

Combining multiple of these singular structures in an array allows for the same operational PV footprint as would be the case for a single VLFS. The structure can be inflated at the installation location, providing a more compact transport solution, which may outweigh the disadvantages associated with the transport of multiple units.

To keep the flexible structure at the intended position a mooring line system will need to be designed. The interaction of the mooring line system, the flexible structure, and the water results in a complex system. To develop a mooring line system for this state of the art design, the motions at the fairlead points of the structure need to be determined. The calculation methods for the motions at the fairlead points of a rigid body structure are known. The calculation methods for a coupled flexible structure and mooring line system are not.

In literature two main options were found to consider the interaction with the mooring line system. The first option considers the structure by means of the finite element method, the fluid by means of computational fluid design, and a Morrison equation for the mooring lines [6]. The second option analyses a fishnet by means of mooring lines and buoys entirely in OrcaFlex [51]. Both of the approaches have associated problems for implementation as required by Bluewater. The structure modelled is either not comparable to a floating flexible structure as designed by the JIP, or the calculation method considers interaction between the structure and the mooring lines as a one way coupling. It is therefore unknown how to calculate the motions of the fairlead points for a flexible structure when influenced by the mooring line system.

Development of a numerical method that can be used to determine the motions of a flexible structure due to environmental forces is therefore desired. The numerical method is to be coupled to an existing mooring line program called OrcaFlex [48] for mooring line analysis. OrcaFlex is preferred as it is an industry standard for mooring line analysis and used at Bluewater. The findings of this new method can then be used in the development of effective and market competitive floating PV and mooring system designs.

1.3. Goal of the thesis

The goal of the thesis is therefore as follows:

”To develop a numerical method that is able to determine the coupled motions of a flexible floating structure and mooring line system. With the focus on the flexible structure.”

1.4. Sub-goals for the method

As the method is to be used in the design process for both the flexible structure as well as the mooring line system, certain sub-goals should be held in mind for the method to be useful.

Firstly, the method has to be applicable in the initial stages of design of both the structure as well as the associated mooring line system. A balance between accuracy and efficiency is therefore required as this allows for quick design iterations. Secondly, as the method is used for designing a coupled floating structure and mooring line system, it should work for different structure designs and mooring line system configurations. Finally, the method has to work in three dimensions due to mooring line analysis requirements for OrcaFlex.

1.5. Scope of the research

The research focuses on the development of a numerical model that can firstly determine the motions of the structure and secondly the coupling of these motions with a mooring analysis in OrcaFlex. To determine the structural behaviour of the structure in the fluid the interaction between the structure and fluid needs to be determined.

The initial focus of the study will be the motions of a single moored flexible floating structure. This choice has been made with the following considerations in mind. Firstly, the time allotted for executing the thesis is limited. Secondly, the motions of a single structure need to be understood before the application to an array of coupled structures can occur. Finally, the interactive coupling with OrcaFlex as described and pursued in this thesis has not yet been realized by others.

The structure modelled in this report is simplified with respect to the JIP structure. The material behaviour of the solar panels on the surface of the structure is unknown, therefore the mass of the panels is distributed homogeneously over the entire structure. The influence of the electronics on the structural behaviour is unknown, but likely small, and will be neglected.

The ballast bags prevent the structure from exiting the water. The response of the ballast bags to incident waves is unknown and likely non-linear. An assumption is made that no gaps exist between the structure and the fluid surface. The ballast bags therefore remain underwater and don’t add additional mass.

Finally, marine growth is not considered as the impact is still being investigated. The impact of marine life on the structure is not considered.

1.6. Disclaimer

In this thesis the joint industry project design structure characteristics will be used for the validation of the method. The designs made in the JIP are not considered part of the thesis and are still in development, therefore no structural characteristics will be provided and wherever possible results are normalized.

1.7. Thesis structure

This report provides the underlying theory, implementation, verification, and validation of the developed method. The structure of the report is detailed below.

In chapter 2, the method for analysis, linear potential theory, structural theory, and theory required for the coupling with a mooring line system in OrcaFlex is described. An overview of the written program and an in depth view of each of the components is provided in chapter 3. The program is then verified in parts in chapter 4. In chapter 5, the original and numerical setup for the experiments used for the validation of the program are discussed and results are provided for the undisturbed wave and three test cases. A discussion of the results is provided in chapter 6. In chapter 7 the work done is reflected upon and conclusions are drawn. Finally, the recommendations for future work are detailed in chapter 8.

2

Theory

In this chapter the theory is described required for the implementation of the newly developed method in chapter 3. This chapter consists of two parts.

In the first part (section 2.1), the approach and theory used to model the structure are determined based on the expected motion of the JIP structure, knowledge found in literature, and the requirements for the method as stated in section 1.4.

In the second part (sections 2.2 to 2.6), the theory required for the numerical calculations will be discussed. This will be done in five steps. First the hydroelastic theory is described. Then the linear potential theory is discussed, followed by the theory required for structural damping and mooring line analysis. Finally, coupling between the mooring line system and the structure is described.

2.1. Method

In this section the approach used to model the motions of the flexible structure is determined. This consists of two steps. First, the expected response of the structure to waves is determined (subsection 2.1.1). Then, the different analysis types will be described, and the analysis approach is chosen (subsection 2.1.2).

2.1.1. Response

To determine the approach to use to model the motions of the flexible structure in a fluid, the expected behavior needs to be determined. For this we look to comparative structures. One example of a flexible structure is a very large floating structure (VLFS). A VLFS is characterized by a very large length to thickness ratio, kilometers in contrast to meters. This large ratio results in a relatively small flexural rigidity which can result in flexible behavior when the structure is under load. The theory regarding the interaction between a flexible structure and fluid is called hydroelasticity [2].

Two distinct types of VLFS are the pontoon type and the semi-submersible type, as represented in Figure 2.1. The pontoon type VLFS retrieves its buoyancy directly from the submerged body, the semi-submersible consists of the deck, legs, and horizontal buoyant members called pontoons. The JIP structure has longitudinal and transverse dimensions much larger than its thickness. The buoyancy of the JIP structure comes from the full submerged volume which consists of the full bottom surface. The JIP structure therefore has no buoyant protrusions as found in the semi-submersible type. Although it has smaller dimensions than a typical pontoon type VLFS, it still has a relatively large length to height ratio. The pontoon type VLFS is therefore a valid comparable structure for an initial assessment of the expected response for the JIP structure.

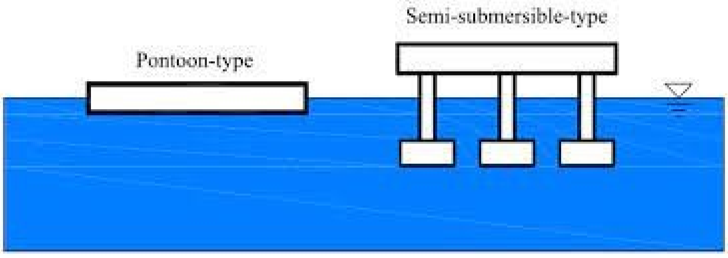

Figure 2.1: Very large floating structure types [59]

Suzuki and Yoshida [56] describe a rational measure called the characteristic length (λ_c), which can be used to distinguish conventional ships and offshore structures from Very Large Floating Structures. This metric can be determined by means of Equation 2.1.

$$\lambda_c = 2\pi(\frac{EI}{k_c})^{\frac{1}{4}} \tag{2.1}$$

In which EI is the bending stiffness of the beam, and k_c the spring constant of the hydrostatic restoring force see Equation 2.2.

$$k_c = \rho_w g B \tag{2.2}$$

In which ρ_w is the density of the water, g is the gravitational acceleration, and B is the width of the beam. The ratio of length of the structure (L) over the incident wave length (λ_i), and length of the structure over the characteristic length (λ_c) can then be determined. By applying the ratios in Figure 2.2 the expected dominant response can be found.

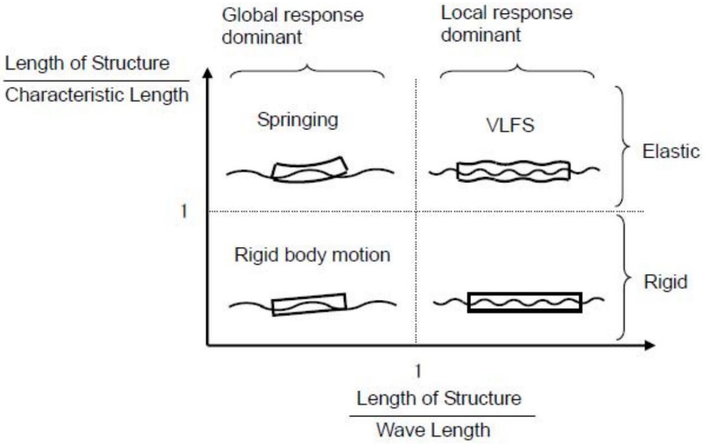

Figure 2.2: Mapping of the dominant response of floating structures

As mentioned, the provided equations assume that the structure can be resembled as a beam. This assumption can be considered valid when the structure has a large length to height ratio. It is now assumed that the JIP structure can indeed be resembled as a beam based on its similar length to height ratio as a pontoon type VLFS. This neglects the ballast bags, which have a larger height to length ratio as well. By substituting the dimensions and values for the JIP structure into Equation 2.1 and Equation 2.2 a ratio of structure length to characteristic length of 2.35 is found. The expected response according to Figure 2.2 is therefore as follows. When waves are longer than the structure the global elastic response is expected to be dominant. When the wavelength is shorter than the structure local elastic responses are expected.

2.1.2. Analysis types

To determine which type of analysis is suitable for the problem posed in this thesis, the different types of analyses, and their advantages and disadvantages are described. Based on the provided information and the method requirements as stated in chapter 1, an analysis type is selected.

In literature a clear distinction is made between analyses executed in the time-domain or in the frequency domain [5]. In the time domain analysis the solution of the system depends on the full equation of motion at each time step. The frequency domain analysis only considers the harmonic loading frequencies for small deformations.

The time domain methods can be split into linear and nonlinear analyses options. The time domain method is often considered computationally expensive. It is therefore, with an eye on the goals stated in section 1.4, that frequency domain methods will be described and considered below.

Watanabe et al. [71] state in their literature review that for mat-type (pontoon) structures usually the following assumptions are made.

- The structure can be modelled as an elastic (thin) plate with free edges.
- The fluid can be modelled to be incompressible, inviscid and irrotational (i.e. potential flow theory is valid).
- The amplitude and motions of the structure are small.
- No gaps occur between the VLFS and the free surface.

Kashiwagi [24] states that the commonly used methods for determining the hydroelastic response of a VLFS in the frequency domain can be divided in the following groups. The first is the direct method [76], [77]. The second is the mode-expansion method [31], [58], [23], [35], and [40]. The last option is a coupled Finite Element Method (FEM) - Boundary Element Method (BEM) approach. These options are discussed below.

In the direct method all degrees of freedom of the floating structure are used in the solution of the equation of motion. In a linear modal superposition (expansion) method the degrees of freedom in the equation of motion are uncoupled and nonlinear effects are discarded. The structural response can often be described as a subset of all modes [3], thereby reducing calculation times. This assumption is valid for responses dominated by low modes and often used in structural dynamics [8]. Inclusion of more modes allows for a better approximation of the actual response.

A second distinction can then be made for the modal analysis, as it can be split into the dry mode and wet mode approach [29]. In the dry mode analysis, the eigenvalue analysis is separated from the hydrodynamic analysis. In the wet mode analysis the eigenvalue analysis considers the impact of the hydrodynamic analysis on the modal shapes.

In the FEM-BEM approach the structural characteristics are determined by modelling the structure by means of a large number of elements. The fluid interaction is modelled by means of the boundary element method in which the underwater (wetted) surface area of the structure is subdivided into panels. The subdivision into panels then allows for the calculation of the fluid effects. Addition of the hydrodynamics to the nodes on the structural matrices and solving the frequency domain equation of motion then allows for the modeling of the hydroelastic behaviour of the structure.

An overview of all described analyses types is provided in Figure 2.3.

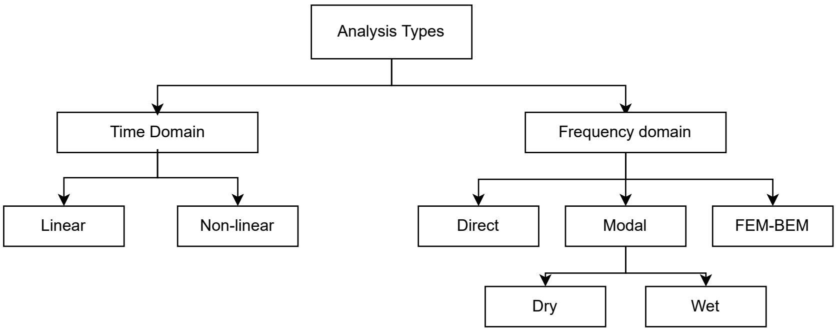

Figure 2.3: Overview of time and frequency domain analyses types

The direct method, due to all nodes being accounted for, is the most expensive of the frequency domain options. The direct method is most effective when higher modes dominate the overall response [20]. A further important note is that the direct method aims to reduce the computational requirements when assessing very short waves for VLFSs.

For the modal analysis Loukogeorgaki et al. [29] state that the wet mode approach is computationally more expensive than the dry mode superposition approach. The wet modes are calculated based on both structural matrices and hydrodynamic matrices, which can be determined by means of the Boundary Element Method (BEM) which uses panels to determine the hydrodynamics of the structure. In modal analysis the investigation of very short waves would require a high number of panels for accurate representation of the hydrodynamic effects. This becomes an issue for VLFSs as the modal superposition method would become increasingly computationally expensive. As the structure considered in this thesis has dimensions considerably smaller in both longitudinal and transverse directions than considered for a VLFS, the required number of panels for the JIP structure is much smaller than would be the case for a VLFS. The modal analysis approach does require a deviation from ”normal” BEM theory as flexible modes have to be included in the calculation of the radiation potentials.

The advantage of the FEM-BEM approach is that it can be executed in the full form or a reduced basis (modal) form. The modal form allows for the decoupling of equations and a higher efficiency at the cost of some accuracy, as the equations for the degrees of freedom become uncoupled. The method can be extended to the time domain if required in the future. The disadvantage of the panel size dependence in the boundary element method is the same as found for the modal analysis.

The choice for the method as described in the rest of the thesis is based on the expected structural response, the advantages and disadvantages of the analysis types, and the method requirements as described in section 1.4. The efficiency and accuracy balance requirement for the method is the main variation between the approaches discussed above. Another thing to be considered is the flexibility of the chosen approach for future expansion of the method. The dimensions of the JIP structure, required efficiency and accuracy, and future expansion options result in the choice for the coupled FEM-BEM approach.

The impact of the mooring line system on the analysis will be discussed later in this chapter.

2.2. Hydroelastic method

In this section the theory used to determine the interaction between the fluid flow and structural reactions is described. This happens in two parts. First a theoretical overview is given for the coupled FEM-BEM approach. Then the assumptions that go along with this approach are presented.

2.2.1. An overview of the coupled FEM-BEM approach

In structural dynamics the motion of a structure under periodic loading can be described by the equation of motion as provided in Equation 2.3.

$$\mathbf{M}^{str}\ddot{u}(t) + \mathbf{B}\dot{u}(t) + \mathbf{K}^{str}u(t) = \vec{F}e^{i\omega t} \tag{2.3}$$

In this equation the structural mass ($\mathbf{M}^{str}$), damping ($\mathbf{B}^{str}$), and stiffness ($\mathbf{K}^{str}$) matrices are to be determined for the dry structure. The displacement in time (t) is $u(t)$, $\ddot{u}$ represents the double time derivative (u), $\dot{u}$ represents the first time derivative of the displacement. $\vec{F}$ is a general force on the system, i is the imaginary number, and frequency is denoted as ω.

To implement the impact of the fluid matrices in the intended manner, the time domain equation of motion is first written as a frequency domain equation by assuming a steady state solution of the system, given in Equation 2.4. I.e. a solution that is a time independent function. In this function $\vec{\zeta}$ is the displacement in the frequency domain.

$$u = \vec{\zeta}e^{i\omega t} \tag{2.4}$$

When substituting this into Equation 2.3 this results in Equation 2.5.

$$-\omega^2\mathbf{M}^{str}\zeta e^{i\omega t} + i\omega\mathbf{B}^{str}\zeta e^{i\omega t} + \mathbf{K}^{str}\zeta e^{i\omega t} = \vec{F}e^{i\omega t} \tag{2.5}$$

Writing the equation in the form above allows for the elimination of the time dependency by dividing by $e^{i\omega t}$. The equation is visually simplified by combining all terms multiplied by ζ. This equation is now fully in the frequency domain and fluid dependent matrices determined in the frequency domain can be implemented.

Implementation of the fluid matrices in Equation 2.5 results in Equation 2.6. In which the fluid matrices and vectors are given as the added mass ($\mathbf{A}(\omega)$), hydrodynamics damping ($\mathbf{B}(\omega)$), hydrostatic stiffness ($\mathbf{C}_s$), and wave excitation force ($\vec{F}^w_{exc}$).

$$[-\vec{\omega}^2(\mathbf{M}^{str} + \mathbf{A}(\omega)) + i\vec{\omega}(\mathbf{B}(\omega) + \mathbf{B}^{str}) + (\mathbf{K}^{str} + \mathbf{C}_s)]\vec{\xi} = \vec{F}^w_{exc} \tag{2.6}$$

To achieve the goal stated in section 1.3, the fluid-structure equation of motion needs to be solved for the unknown displacement vector $\vec{\zeta}$.

2.2.2. Assumptions

The assumption made in section 2.2 that the system has reached an equilibrium solution in the steady-state means that some assumptions and limitations are applied. The assumptions and limitations for both the general case described, and the modal analysis approach of FEM-BEM are given below.

General FEM-BEM assumptions and limitations

The equation of motion in this method is not suitable for the calculation of shock forces. The displacements and rotations in the structure are small. The structure is modelled with an isotropic material, to account for the smearing of the mass of the solar panels and the ballast bags. The system should be linear: linear material behavior and no nonlinear geometric effects.

Modal FEM-BEM assumptions and limitations

If a modal analysis is used in the FEM-BEM analysis the assumptions below must be considered.

Modal superposition can only be applied for linear calculations, as nonlinear behaviour may change the natural frequency significantly during the analysis. If the structure is non-linear, the equation of motion analysis should be solved using the fully coupled matrices.

The problem under consideration should have the following characteristics for it to be suitable for linear transient dynamic analysis.

- The system should be linear: linear material behavior, no contact conditions, and no nonlinear geometric effects.
- The response should be dominated by relatively few frequencies. As the frequency content of the response increases, the modal superposition technique becomes less effective.
- The dominant loading frequencies should be in the range of the extracted frequencies to ensure that the loads can be described accurately.
- The initial accelerations generated by any suddenly applied loads should be described accurately by the eigenmodes.
- The system should not be heavily damped.

The second and third characteristics for the modal FEM-BEM approach may result in difficulties for the mooring line system implementation and might require more assumptions or simplifications, these are described in section 2.6.

2.3. Potential flow theory

In this section the linear potential theory used to determine the influence of the structure on the fluid domain is discussed. First the reason for application is provided, and then the assumptions, boundary conditions, and the governing equations will be provided.

2.3.1. Reasoning

The most complete description of a flow field is given by the viscous Navier-Stokes equation. Computational Fluid Design (CFD) solves these equations, but comes with large computational cost. By allowing for simplifications the required solution time can be drastically reduced. The main simplifications are that viscosity and viscous effects are not relevant to the problem considered. For ocean engineering this assumption is often made [66] for ocean waves at the free surface. Some of these assumptions overlap with those made for modal superposition, for example that only small deformations and rotations of the structure are considered.

2.3.2. Linear potential flow theory

By assuming that the water is incompressible and by applying the continuity principle for a control volume, the continuity equation can be found, see Equation 2.7. In which u, v, and w are velocity components of flow ($\vec{V}$) in x, y and z direction.

$$\frac{\delta u}{\delta x} + \frac{\delta v}{\delta y} + \frac{\delta w}{\delta z} = 0 \tag{2.7}$$

By assuming that the flow can be considered irrotational and non-viscous, the velocity potential function (Φ) can be used to describe motions of the water, see Equation 2.8. In which ∇ is a collective term for the second order derivatives in x, y, and z-direction,

$$u = \frac{\delta \Phi}{\delta x}, v = \frac{\delta \Phi}{\delta y}, w = \frac{\delta \Phi}{\delta z} \tag{2.8}$$

Substitution into the continuity equation 2.7 results in the Laplace equation 2.9.

$$\frac{\delta^2 \Phi}{\delta x^2} + \frac{\delta^2 \Phi}{\delta y^2} + \frac{\delta^2 \Phi}{\delta z^2} = \nabla^2 \Phi = 0 \tag{2.9}$$

The boundary conditions to be satisfied by the potential are:

1. The body surface (S), boundary condition (on S(x,y,z)):

   $$\frac{\delta \phi}{\delta n} = v_n \tag{2.10}$$

   In which v_n is the outward normal velocity at the submerged surface of the structure (positive in the direction of the fluid).

2. The sea bottom boundary condition at z = $-\infty$, guarantees that no fluid permeates through the sea bed at depth z:

   $$\frac{\delta \phi}{\delta z} = 0 \tag{2.11}$$

3. The linearized combined kinematic and dynamic free surface boundary condition at z = 0, (result from combining the kinematic (vertical velocity of free surface is equal to that of the vertical motion of the fluid) and dynamic (pressure above free surface is constant and equal to zero) free surface boundary conditions, by differentiating the dynamic and substituting the kinematic):

   $$\frac{\delta \phi}{\delta z} - \frac{\omega^2}{g} \phi = 0 \tag{2.12}$$

   In which ω is the wave frequency [rad/s] and g is the acceleration due to gravity.

The interaction between a floating body and incident waves can be split into the following phenomena according to Wehausen [73]:

- The incident wave changes the fluid pressure force on the body, causing oscillation about the mean position of the body. This is captured by the velocity potential of the incident wave (ϕ_0).
- The presence of the body scatters the incident wave, these scattered waves affect the motion of the body by exerting fluid pressure forces. This is described by the scattering potential (ϕ_7).
- The motion of the body generates radiation waves, which radiate away and exert fluid pressure forces on the body. These are accounted for by the radiation potentials (ϕ_{1-6}).

Using the assumptions for potential flow and linearized boundary conditions, and the steady-state interaction of the body with a regular deep water wave, the total velocity potential in the vicinity of the body can be expressed as Equation 2.13 ([33], [73], and [12]).

$$\Phi(\vec{x},\gamma,t) = [\phi_0(\vec{x},\gamma) + \phi_7(\vec{x},\gamma) + \sum_{j=1}^{6} \eta_j \phi_j(\vec{x})]e^{i\omega t} \tag{2.13}$$

Equation 2.13 is true for a body moving in the rigid body modes i.e. j = 1...6. The general representation of the axis system for a floating structure is provided in Figure 2.4. Surge (j=1) is a displacement in the direction of the x-axis, sway (j=2) is displacement in the direction of the y-axis, heave (j=3) is displacement in the direction of the z-axis, roll (j=4) is a positive right hand rotation about the x-axis, pitch (j=5) a positive rotation about the y-axis, and yaw (j=6) a positive rotation about the z-axis.

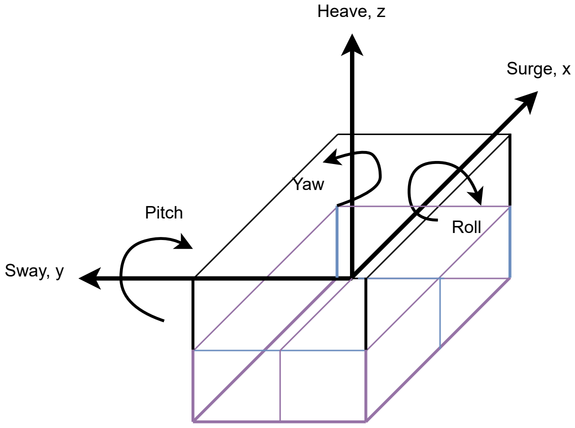

Figure 2.4: Definition of the axis system and degrees of freedom for a floating structure. Blue lines are the submerged part of the body.

The incident wave potential for deep-water is expressed as Equation 2.14. Which consists of the incident wave angle (γ), wave amplitude (ζ_a), imaginary number (i), and the wave number (k).

$$\phi_0(\vec{x},\gamma,\omega,\zeta_a) = i\frac{g\zeta_a}{\omega} e^{kz} e^{-ik(x\cos(\gamma) - y\sin(\gamma))} \tag{2.14}$$

The body boundary conditions for the body in its mean position (Equation 2.15) are added to mentioned conditions: Equation 2.9, Equation 2.11 and Equation 2.12, which are applicable for all $j \in 1,\dots,7$ for ϕ_j.

$$\frac{\delta\phi}{\delta n} = \begin{cases} i\omega n_j & j = 1,\dots,6 \\ -\frac{\delta\phi_0}{\delta n} & j = 7 \end{cases} \tag{2.15}$$

The linearized Bernouilli equation provides a relation for the velocity potential in the fluid and the fluid pressure [11]. The pressure (p) consists of a hydrodynamic pressure (first term) and the hydrostatic pressure (second term), which are both dependent on the water density (ρ).

$$p(\vec{x},t) = -\rho\frac{\delta\Phi(\vec{x},t)}{\delta t} - \rho g z \tag{2.16}$$

In this equation the η_j term is the amplitude in mode j.

The total velocity potential Φ in Equation 2.16 is the sum of the diffraction potential (Φ_d) and radiation potential (Φ_r). For which:

$$\Phi_d = (\phi_0(\vec{x},\gamma) + \phi_7(\vec{x},\gamma))e^{i\omega t} \tag{2.17}$$

$$\Phi_r = \sum_{j=1}^{6} \eta_j \phi_j(\vec{x})e^{i\omega t} \tag{2.18}$$

To determine the pressure forces on the body, the global coordinate system $\vec{x}$ is first changed to the wet body coordinate system. This system has the same origin and axes direction as the global coordinate system, but the axes are denoted as ξ, η, and ζ which are components of $\vec{\xi}$. Then by substitution of Equation 2.17 into the first term of Equation 2.16 and integration over the mean wetted surface (S) the wave excitation load (F_k^{exc}) is obtained, see Equation 2.19. In which S_0 is the wetted body surface.

$$F_k^{exc} = -\rho\int\int_{S_0}\frac{\delta\Phi_0(\vec{\xi},t)}{\delta t}n_k(\vec{\xi})dS - \rho\int\int_{S_0}\frac{\delta\Phi_7(\vec{\xi},t)}{\delta t}n_k(\vec{\xi})dS) \text{ for k = 1, ..., 6} \tag{2.19}$$

The first term consist of the forces due to the incident wave potential and are called the Froude Kryloff loads. The second term consists of the loads due to the scattered wave potential and are called the diffraction loads [11]. Applying the same process as used for Equation 2.19, but now for the radiation potential (Equation 2.18), results in Equation 2.20. In which n_j considers the normal directions to the surface for the rigid modes (1-6).

$$F_k^r = -\int\int_{S_0}\frac{\delta\Phi_R(\vec{\xi},t)}{\delta t}n_j(\vec{\xi})dS \tag{2.20}$$

The time derivative results in an inertia related part and damping related part, see Equation 2.21. These terms are often referred to as the added mass ($A(\omega)$) and hydrodynamic damping ($B(\omega)$) in which the load is in the direction of the k^{th} degree of freedom due to a body oscillation in the j^{th} degree of freedom.

$$F_{k,j}^r = [-\frac{\rho}{\omega}\int\int_{S_0} Im(\phi_j(\vec{\xi})n_k(\vec{\xi})dS)]\eta_j\frac{e^{i\omega t}}{\delta^2 t} + [-\rho\int\int_{S_0} Re(\phi_j(\vec{\xi})n_k(\vec{\xi})dS)]\eta_j\frac{e^{i\omega t}}{\delta t} \tag{2.21}$$

Or in a more reader friendly format:

$$A_{k,j} = -\frac{\rho}{\omega}\int\int_{S_0} Im(\phi_j(\vec{\xi})n_k(\vec{\xi})dS)\eta_j\frac{e^{i\omega t}}{\delta^2 t} \tag{2.22}$$

$$B_{k,j} = -\rho\int\int_{S_0} Re(\phi_j(\vec{\xi})n_k(\vec{\xi})dS)\eta_j\frac{e^{i\omega t}}{\delta t} \tag{2.23}$$

The radiation and scattered wave potentials ϕ_{1-7} are unknown and need to be determined.

Before proceeding to the process of how these potentials can be determined, a description of the hydrostatic stiffness is provided. The hydrostatic stiffness matrix coefficients, also known as restoring spring coefficients [22], assure that the net weight of the structure and the buoyancy are in balance. For a double-symmetric body in a 6 degree of freedom system, only five entries in the matrix are filled. These are the heave coefficient C_{33}, the roll coefficient C_{44}, and the pitch coefficient C_{55}. As the theory for this part is quite lenghty and well known, the reader is referred to the book by Journee and Massie [22] in which a more in depth description is given. The numerical functions and implementation will be discussed later.

2.3.3. Velocity potentials via source distribution

The velocity potential at any field point Q in the fluid domain can be expressed by means of a surface distribution of sources, see Equation 2.24 [28].

$$\phi(\vec{x}) = \frac{1}{4\pi}\int_S \sigma(\vec{x_S})G(\vec{x},\vec{x_S})dS \tag{2.24}$$

Where $\vec{x_s}$ is a point on the body surface S, and the unknown source distribution $\sigma(\vec{x_S})$. The Greens function G provides a means to solve linear inhomogeneous partial differential equations by transforming the partial differential equation to an integral equation representation of the same problem [4]. The Greens function satisfies the boundary conditions (including free surface and radiation conditions), the continuity condition, but not the normal velocity boundary condition on the surface of the body given in Equation 2.10. Kim [27] provides derivations in great detail for the deep-water Green function. Expressions for the infinite-depth free-surface Green function and its derivatives have been published by Telste and Noblesse [63] and later by Ponizy [49], see Equation 2.25.

$$G(\vec{x},\vec{\xi},f) = -\frac{1}{4\pi}(\frac{1}{r}+\frac{1}{r'}) + \tilde{G}(\vec{x},\vec{\xi},f) \tag{2.25}$$

in which:

$$\tilde{G}(\vec{x},\vec{\xi},f) = -\frac{1}{4\pi}[2fR_0(h,v) - i\pi J_0(h)e^v] \tag{2.26}$$

$$f = \frac{\omega^2 L}{g}, \text{L is the reference length} \tag{2.27}$$

$$\rho = (x-\xi)^2 + (y-\eta)^2 \tag{2.28}$$

In which ρ is the radius in two dimensional space, which is used to determine the distances r and r’ in three dimensions in Equation 2.29 and Equation 2.30.

$$r = \sqrt{\rho^2 + (z-\zeta)^2} \tag{2.29}$$

$$r' = \sqrt{\rho^2 + (z+\zeta)^2} \tag{2.30}$$

$$h = f\rho \tag{2.31}$$

$$v = f(z+\zeta) \tag{2.32}$$

The first term of Equation 2.25 is the sum of the source potential at the field point and the source potential at the image source due to a unit source. The image source realizes the boundary constraint required at the linearized free surface and the body [37]. The second part $\tilde{G}$ represents the oscillating potential due to the source strength at the field point, which accounts for the presence of waves. For clarification of the distances as specified in equations 2.29 & 2.30, please see Figure 2.5.

Telste and Noblesse [63] give the following expressions for the derivatives of the oscillating part of the potential ($\tilde{G}$):

$$\frac{\delta\tilde{G}}{\delta x} = \frac{\delta\tilde{G}}{\delta\rho}\frac{(x-\xi)}{\rho} \tag{2.33}$$

$$\frac{\delta\tilde{G}}{\delta y} = \frac{\delta\tilde{G}}{\delta\rho}\frac{(y-\eta)}{\rho} \tag{2.34}$$

$$\frac{\delta\tilde{G}}{\delta z} = \frac{1}{4\pi}\left[-2f^2\frac{1}{d} + R_0(h,v) - i\pi J_0(h)e^v\right] \tag{2.35}$$

and,

$$\frac{\delta\tilde{G}}{\delta\rho} = \frac{1}{4\pi}\left[2f^2R_1(h,v) + iJ_1(h)e^v\right] \tag{2.36}$$

$$d = \sqrt{h^2+v^2} = fr' \tag{2.37}$$

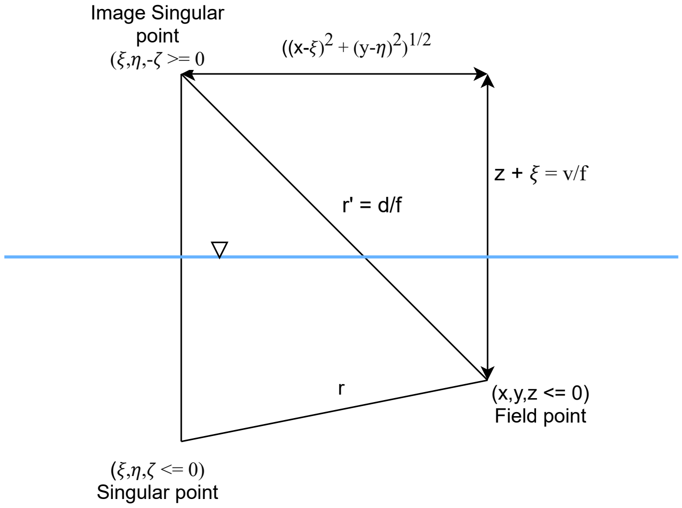

Figure 2.5: Definition sketch [adapted from [63]]

In which J_0 and J_1 are Bessel functions of the first kind, and R_0 and R_1 are real functions to be defined by for instance the FORTRAN code in the appendix of Telste and Noblesse [63].

The singularity that is located exactly on the source point is avoided by placing the source panels at a small distance from the centroid of the body panel as proposed by Guha [16].

The radiation and scattered wave potential potentials can then be determined with equation by Faltinsen [12], in which j specifies the scattered wave potential (ϕ_7) and radiation potentials (ϕ_{1-6}):

$$\phi_j(\vec{x}) = \int\int_{S_0} \sigma_j(\vec{\xi}) G(\vec{x}, \vec{\xi}, f) dS \tag{2.38}$$

Using the body boundary condition (Equation 2.10) and substituting gives Equation 2.39 for the scattered wave potential and Equation 2.40 for the radiation potentials.

$$\frac{\delta}{\delta n(\vec{x})} \int\int_{S_0} \sigma_j(\vec{\xi}) G(\vec{x}, \vec{\xi}, f) dS = \begin{cases} -\frac{\delta \phi_0}{\delta n(\vec{x})}, & \text{j = 7 and } \vec{x} \in S_0 \end{cases} \tag{2.39}$$

$$\frac{\delta}{\delta n(\vec{x})} \int\int_{S_0} \sigma_k(\vec{\xi}) G(\vec{x}, \vec{\xi}, f) dS = \begin{cases} i\omega n_k(\vec{x}), & \text{k = 1, ..., 6 and } \vec{x} \in S_0 \end{cases} \tag{2.40}$$

Malenica et al. [32] provide Equation 2.41 in which the integral is interpreted in the Cauchy principal value sense due to the singularity that occurs when the source and field point coincide:

$$\frac{\delta}{\delta n(\vec{x})} \int\int_{S_0} \sigma_j(\vec{\xi}) G(\vec{x}, \vec{\xi}, f) dS = \frac{\sigma_j(\vec{x})}{2} + \int\int_{S_0} \sigma_j(\vec{\xi}) \frac{\delta G(\vec{x}, \vec{\xi}, f)}{\delta n(\vec{x})} dS \tag{2.41}$$

The source density distributions associated to the radiation and scattered wave potentials can then be determined from Equation 2.42 which results from the substitution of either Equation 2.39 into Equation 2.41 or vice versa:

$$\frac{\sigma_j(\vec{x})}{2} + \int\int_{S_0} \sigma_j(\vec{\xi}) \frac{\delta G(\vec{x}, \vec{\xi}, f)}{\delta n(\vec{x})} dS = \begin{cases} i\omega n_j(\vec{x}), & \text{j = 1, ... , 6 and } \vec{x} \in S_0 \\ -\frac{\delta \phi_0}{\delta n(\vec{x})}, & \text{j = 7 and } \vec{x} \in S_0 \end{cases} \tag{2.42}$$

The source densities therefore now only depend on the incident wave potential, and the normal vectors to the body surface. The numerical determination of the source density distributions and calculation of the potentials will be discussed from section 2.7 onward.

By determining all the potentials, the previously mentioned added mass, hydrodynamic damping and wave excitation force can be determined (Equation 2.19, Equation 2.21).

2.4. Structural theory

In this section first the method used to determine the structural mass and stiffness matrices is chosen based on recommended methods in literature. Then the impact of the structural damping is discussed along with possible modeling approaches and considerations.

2.4.1. Structural method

The goal of the thesis is to develop a program which can determine the coupled motions of a flexible structure and mooring line system with a focus on the fluid-structure interaction. To analyse the effect of the structure on the mooring lines and vice versa, the structure has to be considered in three dimensions.

A lot of research has been done on the subject of very large floating structures, and often the VLFS is modeled via Timoshenko beam theory, or a via Mindlin plate theory for thin to moderately thick plates. This is valid when the cross section of the structure resembles these shapes and has been applied by [24], and [40]. Suzuki et al. [56] state: “A combination of a plate Finite Element (FE) model and a modal approach (Okada et al, 1999) is also applied when a more refined structural modeling (e.g., a variable flexural stiffness) is needed.” As previously stated in section 1.2, the structure length and width are considerably shorter than considered in a VLFS. The accompanying assumption of a large length to height ratio should therefore be weighed based on the design of the structure.

In the JIP design the ratio of length to height is roughly equal to 50 [-]. The ratio for which a structure is considered a pontoon type (or mat-type) is 60 and higher [75], The JIP structure is however much lighter resulting in a comparatively small draft. In subsection 2.1.1 it was determined that the structure was expected to move as a VLFS when wave lengths were smaller than the length of the structure,

The structure in this report is therefore considered as a plate by means of finite elements. This allows for a relatively simple calculation in three-dimensions allowing for mooring line system coupling. This program then has the potential to be expanded to a more refined structure analysis in the future, without building a completely new program. The progression of analysis by means of a simple structural shape, before progressing also allows for a gradual verification and validation process during the development of the program. A short description of how the finite element method works is provided later.

2.4.2. Structural matrices

In section 2.3 the hydrodynamic damping was discussed, also called the wave or potential damping. In an actual viscous fluid, friction would also result in the loss of energy from the system. Due to the assumption made by applying linear potential theory, the viscous contributions were neglected.

In structural dynamics various forms for approximating the structural damping are proposed. Each of the methods aims (directly or indirectly) to specify a a damping ratio ζ_d. In practice the structural viscous damping is often assumed by means of Rayleigh damping, or proportional damping [7]:

$$\mathbf{B}^{str} = \alpha \mathbf{K}^{str} + \beta \mathbf{M}^{str} \tag{2.43}$$

In Equation 2.43 α and β are the stiffness and mass proportional damping coefficients. For flexible structures there is still discussion on what the appropriate, α and β coefficients are. One option is to determine the coefficients as fractions of the critical damping ξ_{crit} for the first two non-zeros frequencies (ω_1, ω_2):

$$\alpha = \frac{2(\xi_2\omega_2 - \xi_1\omega_1)}{\omega_2^2 - \omega_1^2} \tag{2.44}$$

$$\beta = \frac{2\omega_1\omega_2(\xi_1\omega_2 - \xi_2\omega_1)}{\omega_2^2 - \omega_1^2} \tag{2.45}$$

Equation 2.44, and Equation 2.45 would therefore assume that the damping at other frequencies than ω_1 and ω_2 can be approximated by the two chosen frequencies.

Bureau Veritas [67] recommends that for compliant structures stiffness proportional damping (α dependent) should be used, as mass proportional damping would give damping due to rigid body modes.

Orcina [45] provides a note on this choice. They state that it is quite common for systems to have responses at frequencies higher than the wave frequency, and that these are often damaging to the system. Stiffness proportional damping is however very effective at over-damping the high frequency and should therefore be avoided. The approach recommended is therefore to run cases both with and without mass and stiffness proportional damping, and base the factors α and β on the lowest and highest frequency in the system.

Suzuki et al. [57] state that “Structural damping is usually neglected in discussing hydroelasticity due to wave excitation because its effect is much lower than that of wave making damping in the significant wave period.”. In this thesis the implementation of Rayleigh damping will be implemented, as this only requires simple matrix multiplications of known matrices and scalars. The impact is expected to be small, based on the insight gained from [57].

2.5. Mooring line systems

In this section the goal of, and components in a mooring line system are described. This is followed by an overview of expected load frequencies for the mooring line system and the floating or submerged structure. Finally it is concluded whether the impact of mooring line loads is expected to result in issues for the theory used in the calculation of the motions of the flexible structure.

2.5.1. Goal and components

Mooring line systems are used to keep a floating or submerged structure at a specific location (station keeping). A mooring line system usually consists of three main parts:

- The anchor system, that attaches to the mooring line and secures it to the sea bottom.
- The mooring line, that attaches to both the floating or submerged structure and the anchor system.
- The connectors used to tie the anchor, mooring line and vessel together

The design of a mooring line system depends on environmental factors (wind, waves, and currents), water depth, soil conditions, allowable excursions of the floating or submerged structure, and structural characteristics of the mooring line system. Due to the large variation in design parameters, different types of mooring line systems exist. Miao et al. [72] state that “For a very large floating structure in shallow water the chain mooring lines may be used, which are of nonlinear characteristics, however effective in eliminating motions of the structure.”. In the JIP design a chain system was used and implemented at the test site in Oostvoorne.

2.5.2. Expected load frequencies

In section 2.2.2 the conditions for a successful analysis were discussed. To assess whether mooring line, wind, wave, and current frequencies and associated loads might provide issues, the underlying system is discussed.

The mooring line system is designed to keep a structure within an allowable excursion area while under environmental loads. The expected forcing frequencies are therefore a combination of the environmental loads and the motion of the moored structure. Figure 2.6 provides an overview of the expected periods on the x-axis and relative amount of energy for different ocean waves on the y-axis.

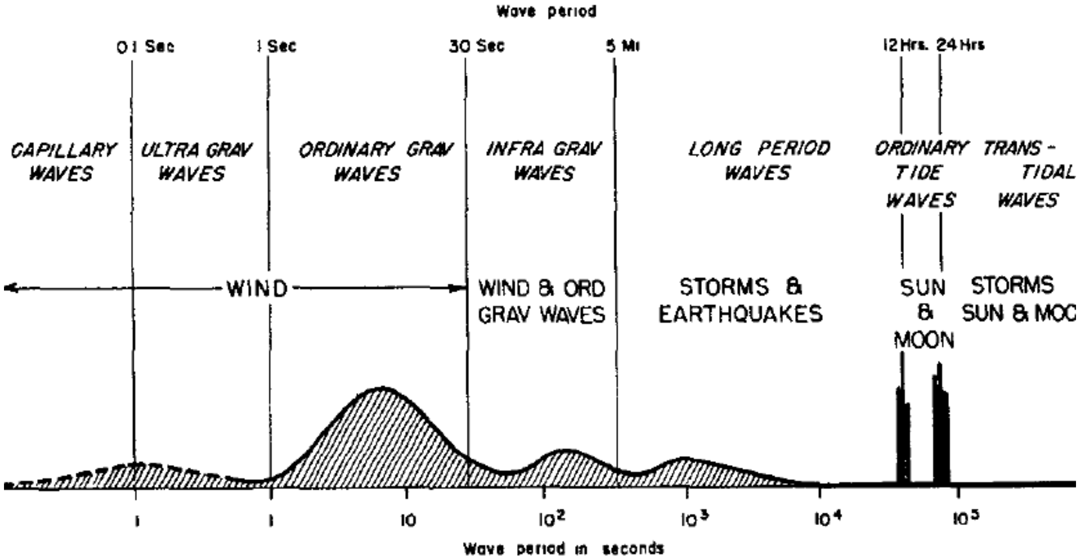

Figure 2.6: Spectrum of ocean waves and relative energy distribution. Wave period [s] on the x-axis, relative energy on the y-axis. Amended from [34]

The figure shows that a large part of the wave energy is located in the periods (T) between 0 and 10e3 seconds. Calculating the associated wave frequency in Hertz ($Freq$) and radians per second (ω), results in the values in Table 2.1.

Period [s]	**Wave frequency [Hz]**	**Wave frequency [$\frac{rad}{s}$]**
10e3	0.001	0.006
30	0.033	0.209
10	0.100	0.628
1	1.000	6.283

Table 2.1: Loading frequencies

A typical mooring line analysis wave frequency range is 0.025 to 2.025 radians per seconds. This range captures a large amount of the energy in the system, but not all.

Structural eigenfrequencies become higher for increasing mode number and are usually much higher than the expected wave frequencies. It is therefore not expected that either the wave frequencies or mooring line induced load frequency will become an issue in the application of the structural theory. The current is assumed constant in a time domain of three hours as the current speed is slowly varying over time. This is in line with the steady-state equilibrium assumption used earlier.

Normally wind forces are also accounted for in the environmental forces via an NDP or API spectrum [47]. In general these can be approximated fairly easily with the Morrison equation, and in the case of a flexible body the Morrison force can be determined based on the above water level panels. Currently wind forces are not considered in this thesis as there is no available measurement data to validate the implementation.

2.6. Coupling theory

In this section the reasoning behind the coupling method considered in the thesis is described. First a short overview is given of other research in which elastic structures were modelled and coupled with OrcaFlex. Which assumptions were made, and what the perceived issues are with those methods. Then the coupling method as considered for the numerical method in this thesis will be described, and what the perceived benefits are over the existing coupling methods.

2.6.1. Methods as applied in literature

Three main solutions for accounting for mooring for flexible structures in literature were found:

1. Model the free floating structure initially as elastic, but account for it as a rigid structure with Response Amplitude Operators (RAOs) at the center of gravity in the mooring analysis in OrcaFlex.

2. Modelling of a fish net in OrcaFlex-Python as an assembly of mooring lines with varying bending stiffness (EI), and use buoys with three degree of freedom (surge, sway, and heave) to allow for structure continuity and motion transfer between lines [51].

3. Model the elastic structure as a combination of smaller rigid structures and couple the motions via the 6 Degree of Freedom buoys. In this case the buoy has RAOs in surge, sway, heave, roll, pitch and yaw direction.

The first method assumes that the mooring line forces will not deform the structure, and therefore accounts for the structure behaviour once through rigid body RAOs. The second method works well for nets, but to model a closed structure more buoys and lines would have to be used. This approach will become less effective as the dimensions of the structure increase, because the length of lines per wavelength should be appropriate to capture the physics. The third method negates the issue found for the second method, and combines plates through 6 DOF buoys. The downside is that specific load cases can result in extremely high unrealistic forces at the connectors between the plates.

2.6.2. Method pursued in this thesis

An integral part of the thesis goal is to develop a numerical method that focuses on hydroelastic structure motions and is designed with an eye for future coupling with a mooring line system in OrcaFlex. Therefore a two-way coupling is pursued. Structural deformations due to mooring line and wave loads should influence the mooring line system behaviour, and the mooring line forces should be able to influence the elastic motions of the structure.

The hydroelasticity of the structure will be described by the theory provided in the previous sections. The dynamic analysis of the mooring line system is executed separately. The interaction between the two will be based on the exchange of mooring line forces and motions at the fairlead points of the structure. Figure 2.7 shows the displacement of the structure and fairlead points (circles) on the left, and the forces (arrows) by the mooring lines due to the displaced fairlead points on the right. The anchors are portrayed by means of triangles which are fixed in place as represented by the triple diagonal lines. In the left figure, the dashed line represents the structure that connects the fairlead nodes. In the right figure, the original position of the mooring line is drawn by means of a dashed line and the displaced position with a solid line. The arrows represent the force on the fairlead points.

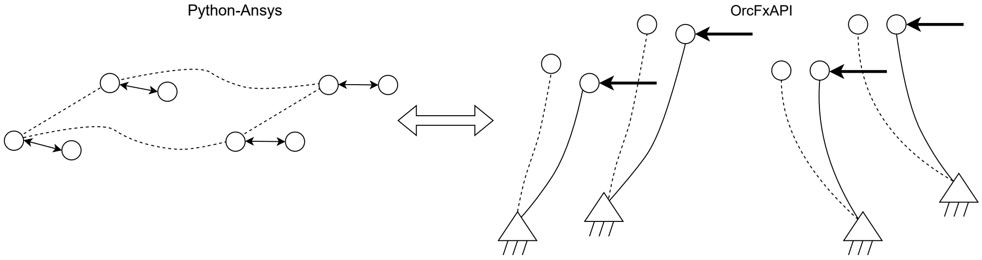

Figure 2.7: Two-way interaction

When the structure moves in a way that results in compression in a mooring line, the mooring line provides no forces on the associated fairlead point except for the weight of and fluid drag on the mooring line. Only the weight of the mooring line will then provide a force to the structure, if the remaining force is low the structure will move freely at that fairlead point. The mooring lines in tension then provide the forces that should keep the structure in its position.

This results in the following advantages.

1. Data efficiency: The only data exchanged is that at the fairlead locations. The position of the calculated fairlead points (on the structure) is resembled at the line end by individually operating 6 DOF buoys.
2. Avoidance of high connector loads: Due to the use of individually displaced buoys and flexible calculation outside of OrcaFlex, high connection loads should be avoided.

The wave exciting force $\vec{F}_{exc}^{w}$ as used in the equation of motion shown in Equation 2.6 is through this interaction complemented by a mooring line force $\vec{F}_{m}$. The coupled equation of motion is shown in Equation 2.46.

$$[-\vec{\omega}^2(\mathbf{M}^{str} + \mathbf{A}(\omega)) + i\vec{\omega}(\mathbf{B}(\omega) + \mathbf{B}^{str}) + (\mathbf{K}^{str} + \mathbf{C}_s)]\vec{\xi} = \vec{F}_{exc}^{w} + \vec{F}_{m} \tag{2.46}$$

The forces provided by OrcaFlex are provided per time step, but in theory can be implemented as frequency domain forces into the equation of motion. The numerical implementation will be discussed in section 2.7.3.

2.7. Numerical approximation

In the section below it is described how the theory discussed in the previous sections 2.2 - 2.6 can be represented by numerical calculations. First the finite element method will be discussed as used for the structural calculations. Next the boundary element method used in the hydrostatic and hydrodynamic calculation is discussed. This is followed by the discussion of the mooring line analysis. Finally, a description of the coupling from numerical point of view is given.

2.7.1. Finite Element Method

The finite element method (FEM) is a numerical method that approximates the solution of partial differential equations which can be used to describe the behaviour of a structure. The finite element method is well known and often used, but for the readers convenience a summary is given below. For more in depth discussions the reader is referred to the book by Hutton [21], which was found to be insightful. The analysis by means of FEM is known as Finite Element Analysis (FEA).

Background

A structure is discretized into a finite number of small elements, which connect at common points (nodes or nodal points). Equations are determined for each element based on a combination of shape functions. The element equations are then assembled into a system of equations that describes the full system. The approximate solution is then optimized (error minimization) by means of small changes to the functions (Calculus of variations).

The resulting combination of finite elements is called the mesh. The mesh is only an approximation of the structure and the accuracy of the solution therefore depends on the element size. When the elements are small enough, the approximate solution converges to the solution of the partial differential equations.

Hutton [21] states the following advantages for using FEM: irregular boundary shapes, different materials and material behaviour, linear or dynamic behaviour, and general loads can be accounted for with easy modification. This makes FEA a valuable tool, but a tool needs to be properly applied.

2.7.2. Boundary Element Method

The linear potential theory described in chapter 2.3 is numerically approximated by means of the Boundary Element Method (BEM). In this method the linear partial differential equation described as integral equations in section 2.3 are solved. The reasons for writing the code as opposed to using a commercial package are given below.

- The hydrodynamic mesh can be coupled directly with the mesh allowing for easier computation of the fluid-structure interaction.
- The added mass and damping can be determined at specific sub-steps, which are normally hidden in the software and not available as output.
- This approach allows for future expansion of the method in terms of different potential theory for shallow and intermediate water depths.

Panel size

For the proper application of the boundary element method a panel size has to be determined. To determine the parameters that the panel size depends on, sources from literature are consulted, arguments are presented, and a decision for a rule of thumb is made.

Maeda & Ikoma [30] state that: “It is not easy to maintain a high-precision computation on hydrodynamics of a very large floating structure based on the boundary-element method, because the size of the element on a large structure should be relatively small compared with the wavelength of incident waves.”. To determine a rule of thumb for analysis the statements by Tay & Wang [60], Wang et al.

[69], Maeda & Ikoma [30], and Journée & Massie [22] are considered.

Tay & Wang state that based on convergence tests, the size of a four-node quadrilateral plate element and constant fluid panel must be smaller than $\frac{\lambda}{10}$ in which λ is the incident wave length. Wang et al. state that experience shows that for a constant panel, the mesh size should be less than 1/10 of the incident wave length. For an 8 node quadratic panel, it should be less than 1/4 of the incident wave length. Maeda & Ikoma state that 10 elements are required per wavelength, but that practically the maximum number of elements must be limited to the memory storage capacity of the computer. Finally, Journée & Massie state that in the wave zone the element size should be small compared to the wave length. That the characteristic length of an element ought to be less than 1/8 of the wave length, and that the best way to find a sufficient number of elements, is to do calculations with increasing numbers of elements and check the convergence of the results.

Finally, the goal in this thesis has to be considered. In this thesis regular deep water (Airy) waves are used. This type of wave is characterized by its small wave steepness, the depth of the fluid is constant, and the fluid is irrotational and incompresible. The panel size should also provide a good wave steepness discretization, i.e. have a certain number of panels in height depending on the ratio of wave height (h) and wave length (λ). As the degree of change is therefore small, the wave length is considered the dominant factor for choosing the panel size.

Based on this information, the element size for the FEM analysis and therefore BEM panel size used in this thesis will ensure that more than 10 elements are used per wavelength. Additionally a convergence panel test will be executed.

Numerical functions

To implement the linear potential theory as described in section 2.3, the panel decomposition method by Hess and Smith [17] is considered. This approach is often used in the application of linear potential theory on floating structures were the surface area to volume ratio is small [25]. A short description of the method will be given below for the readers convenience.

The panel method proposes that the pressure distribution over a body can be accurately obtained by discretizing the mean wetted surface area into N panels of constant size. The source strength is divided homogeneously over all panels and is determined at the panels centroid, also called the collocation point. See Figure 2.8.

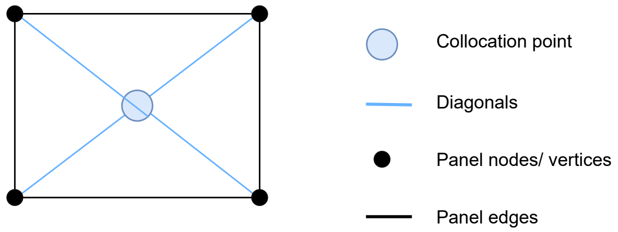

Figure 2.8: Collocation point

Variations exist for the implementation of the panel; lower and higher order panel method [18]. Lower order panels are flat quadrilaterals, whereas the higher order panels can be curved. This would therefore allow for a more accurate representation of a curved body with fewer panels when compared to the lower order implementation. For the cube, box and plate experiments, as modeled in this thesis this is not required. The lower order panel method is implemented and higher order panels might be of interest for future development of the program.

By rewriting the equations given in chapter 2.3 by means of the Hess and Smith panel method, Equation 2.47 can be obtained. In which ξ_p is the centroid position (collocation point) position on the panel (p), N is the number of panels, σ is the source strength on the panel.

$$\sum_{p=1}^{N} \sigma_{j_p}(\vec{\xi}_p) \int\int_{S_p} \frac{\delta G_p(\vec{x}, \vec{\xi}_p, f)}{\delta n(\vec{x})} dS = \begin{cases} i\omega n_j(\vec{x}), & \text{j = 1, ..., 6} \\ -\frac{\delta \phi_0}{\delta n(\vec{x})}, & \text{j = 7} \end{cases} \tag{2.47}$$

For each panel the induced normal velocity at the collocation point is determined. This induced velocity results from a source density distribution on the source panel area (S_p), see Equation 2.48 (amended from [22]). All values are panel and frequency dependent. The calculations required for the determination of α will be detailed chapter on implementation.

$$\begin{vmatrix} \alpha_{11} & \dots & \dots & \dots & \alpha_{1N} \\ \dots & \alpha_{22} & \dots & \dots & \dots \\ \dots & \dots & \alpha_{33} & \dots & \dots \\ \dots & \dots & \dots & \dots & \dots \\ \alpha_{N1} & \dots & \dots & \dots & \alpha_{NN} \end{vmatrix} \begin{vmatrix} \sigma_{1,j} \\ \dots \\ \dots \\ \dots \\ \sigma_{N,j} \end{vmatrix} = \begin{vmatrix} v_{1,j} \\ \dots \\ \dots \\ \dots \\ v_{N,j} \end{vmatrix} \tag{2.48}$$

The source densities (σ) can be determined by solving Equation 2.48 as seen in Equation 2.49.

$$\vec{\sigma}^T = \alpha^{-1} \cdot \vec{v}^T \tag{2.49}$$

The index j in Equation 2.48 depends on whether the scattered wave potential and/or radiation potential needs to be calculated. In case of steady flow the solution should be diffraction dependent (body fixed), whereas when free surface waves occur both radiation and diffraction are considered (body is free).

To determine the potentials a separate matrix β is constructed in Equation 2.50. The calculations required for the determination of β will be detailed in the chapter on implementation.

$$\begin{vmatrix} \phi_{j,1} \\ \dots \\ \dots \\ \dots \\ \phi_{j,N} \end{vmatrix} = \begin{vmatrix} \beta_{11} & \dots & \dots & \dots & \beta_{1,N} \\ \dots & \beta_{22} & \dots & \dots & \dots \\ \dots & \dots & \beta_{33} & \dots & \dots \\ \dots & \dots & \dots & \dots & \dots \\ \beta_{N1} & \dots & \dots & \dots & \beta_{N,N} \end{vmatrix} \begin{vmatrix} \sigma_{j,1} \\ \dots \\ \dots \\ \dots \\ \sigma_{j,N} \end{vmatrix} \tag{2.50}$$

Equations 2.22, 2.23, and 2.19 are respectively the panel variants of the added mass (A_{kj}) (Equation 2.51), hydrodynamic damping (B_{kj} (Equation 2.52), and exciting wave force (F_k^e) (Equation 2.53). The generalized normal is n_{k_p}, which is the multiplication of the surface normal vector and the corresponding displacement field as a result of a nodal displacement. By knowing the radiation and scattered wave potentials these can be calculated for the whole system, or kept separate as later discussed in section 3.3.4. In equations 2.51 & 2.52 $\Im$ and $\Re$ are the imaginary and real parts of the complex potential.

$$A_{kj}(\omega) = -\frac{\rho}{\omega} \sum_{p=1}^{N} n_{k_p} \Im \phi_{j_p}^{\omega} \Delta S_p \tag{2.51}$$

$$B_{kj}(\omega) = -\rho \sum_{p=1}^{N} n_{k_p} \Re \phi_{j_p}(\omega) \Delta S_p \tag{2.52}$$

$$F_k^e = -i\omega\rho \sum_{p=1}^{N} n_{k_p} (\phi_{0_p}(\omega) + \phi_{7_p}(\omega)) \Delta S_p \tag{2.53}$$

Hydrostatic stiffness numerical functions

For the calculation of the hydrostatic stiffness matrix numerical functions are required, these functions are given by McTaggart [33]. In this section only the final equations will be shown.

The filled positions in the hydrostatic stiffness matrix can be determined via Equation 2.54, Equation 2.55, Equation 2.56, Equation 2.57, and Equation 2.58. In which A_{wp} is the water plane area, $x_{wp}A_{wp}$ is the longitudinal centroid of floatation, $z_{cb}\nabla$ is the center of buoyancy relative to the water line, $x_{cb}\nabla$ is the longitudinal center of buoyancy, I_{wp-yy} and I_{wp-xx} are the water plane moments about the x and y axis respectively in which the arm is specified.

$$C_{33} = \rho g A_{wp} \tag{2.54}$$

$$C_{44} = \rho g [\nabla z_{cb} - \nabla z_{cg} + I_{wp-yy}] \tag{2.55}$$

$$C_{55} = \rho g [\nabla z_{cb} - \nabla z_{cg} + I_{wp-xx}] \tag{2.56}$$

$$C_{35} = -\rho g A_{wp} x_{wp} \tag{2.57}$$

$$C_{53} = C_{35} \tag{2.58}$$

Coefficients C_{35} and C_{53} are zero for a structure with double symmetry where the center of buoyancy lies beneath the center of gravity, and will take on a value when a difference in longitudinal position of center of gravity and center of floatation exists. The hull water plane area (A_{wp}) is calculated via Equation 2.59. In which N_p is the number of panels, n_{j_z} is the z normal component of panel j, and z_j is the z-coordinate of the centroid of panel j.

$$A_{wp} = -\sum_{j=1}^{N_p} A_j n_{j_z} z_j \tag{2.59}$$

2.7.3. Mooring line analysis

For the numerical analysis of the mooring line system contribution to the coupled problem, the dynamic analysis software OrcaFlex by Orcina is used with a commercial license. OrcaFlex is an industry standard for the analysis of mooring line systems. In this section the options regarding the calculation methods for mooring lines are discussed.

Modelling options

OrcaFlex offers various ways to run calculations on vessels and mooring line systems, these are listed below with their method of calculation.

- Quasti-static: Determines the equilibrium position of the system, by first determining the line catenary with fixed degrees of freedom (dof) of the vessel, and then releasing the fixed dof's.
- Quasi-dynamic: In the quasi-dynamic analysis only the vessel degrees of freedom are calculated as opposed to also calculating the internal nodes within the mooring lines.
- Frequency domain dynamic: Linear calculation. Uses the static analysis to determine linear transfer functions. These functions are then used to determine the systems response at each frequency. This method can be considerably more efficient than the time domain analysis, but does not consider line dynamics.
- Time domain dynamic: Mass, stiffness, loading, etc. are calculated at each time step and the system is coupled (line loads and vessel loads).

Miao et al. [72] state that “To fully assess the adequacy of a mooring system, it is necessary to carry out dynamic analysis for each mooring line. This can be done numerically by employing, for example, the lumped mass method.”

In this thesis the dynamic analysis in OrcaFlex is considered for future implementation to properly account for the mass and inertia of the mooring lines, and to include the coupling between the structure and the mooring line system.

Lumped mass model

OrcaFlex represents mooring lines by means of a lumped mass model. The mooring line is segmented in nodes which are connected by means of segments. The segments are therefore part of the discretization of the actual line and the properties for one segment (mass, buoyancy, drag, etc.) are lumped at the nodes on the end.

The line is segmented based on user-defined sections, and for each section the user has to define the line properties which can be stored in the line type. The length and number of segments to be used for a section also need to be defined [43]. A section can therefore be used to attain a higher resolution for specific parts of the mooring line by increasing the number of nodes and decreasing the segment length in that section. See Figure 2.9 for a simple overview of the lumped mass model for a two section mooring line. The nodes are represented as circles and the segments as lines between the nodes.

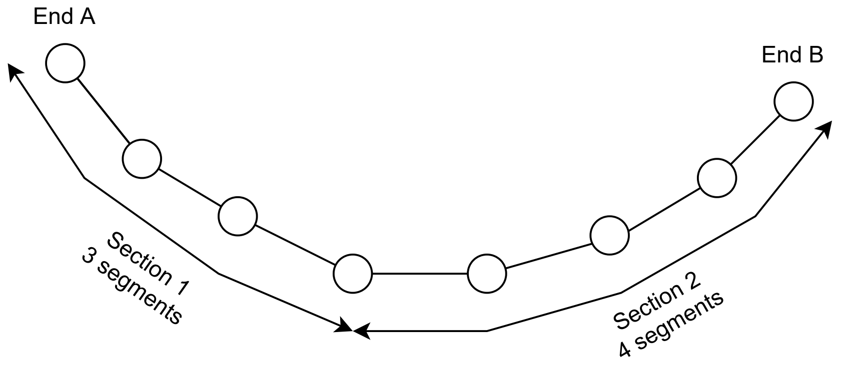

Figure 2.9: Orcina line lumped mass model. Nodes represented by circles, segments by lines between nodes. Sections are comprised of multiple segments.

2.7.4. Numerical coupling

In section 2.6.2, the ”wished for” interaction between the structure and the mooring line system was described. In this section the required software, and steps for implementation are described.

Application Programming Interface

OrcaFlex interaction can be subdivided into two main types. The first is the graphical user interface which is the standard for many users. It provides multiple modeling options, easy interaction and is well documented. The downside is that it requires starting OrcaFlex manually. The second is an Application Programming Interface (API). This API is available for Python and named OrcFxAPI [44]. A similar API is available for Matlab.

The APIs allow the user to write external scripts with specified function handles that are recognized by OrcaFlex. The script is loaded as an external function by OrcaFLex, and specified variables can be exchanged between the OrcaFlex mooring simulation and the external script. This exchange happens at the start of each new time step. OrcFxAPI can therefore be used to implement the two-way interaction described in section subsection 2.6.2. The API is less intuitive to understand, documentation exists, but is not always implemented in the same way as stated [9]. It comes with the advantage that it can be used by calling it from an external program such as Python or Matlab and will allow for the two-way interaction. It is therefore that the API is preferred for implementation.

For the interaction with OrcaFlex two things are required. The first are commands to specify the mooring line system characteristics, and position of the fairlead points. The second are the function handles to retrieve the wave characteristics, fairlead position, and time step value.

Integration procedures

OrcaFlex offers both an implicit and explicit integration procedure for dynamic analysis. An explicit procedure uses the state of the system at a current time to solve the equation at a later time, see example Equation 2.60. An implicit procedure uses both current and later states of the system in solving the equation, see example Equation 2.61 [14].

$$Y(t+\Delta t) = F(Y(t)) \tag{2.60}$$

In which:
Δt = small time step.
Y(t) = current state of the system
Y(t + Δ t) = state of the system at a later time

$$G(Y(t), Y(t+\Delta t)) = 0 \tag{2.61}$$

Explicit methods can be numerically unstable for stiff systems, unless the time step size is taken to be extremely small. An implicit method can therefore be computationally more effective due to the larger time step and iteration(s) within these time steps [42]. These iterations would occur only within OrcaFlex and the final result would be sent to Python. The execution by means of an implicit method in OrcaFlex would therefore be beneficial for the performance of the proposed method.

3

Implementation

In this chapter the numerical representation (section 2.7) of the theory (section 2.3) is implemented in a program. The structure of this chapter is as follows. First a global program layout is provided with a description of each component in the program, see section 3.1. In section 3.2 the design goals of the program, the consideration of and choices for specific program languages and commercial software are discussed. This thesis focuses on the implementation of the fluid-structure interaction part of the proposed program.

The implementation of the fluid-structure interaction (FSI) component of the global program is discussed in the following steps. First a flowchart is provided that represents the internal workings of the FSI component. In subsection 3.3.1, the method used to determine the dry structure characteristics is provided. The process for the boundary mesh construction is described in subsection 3.3.2. In subsection 3.3.3, calculations regarding the panel parameters are discussed. The implementation of the calculation of the added mass, damping, hydrostatic stiffness and exciting wave force is discussed in subsection 3.3.4. The construction of the equation of fluid matrices and exciting wave force vector is discussed in subsection 3.3.5. In subsection 3.3.7, the assembly of the equation of motion is described. Finally, a clarification is provided on the OrcaFlex implementation, and the verification and validation executed in the following chapters.

3.1. Global program layout

The program developed in this thesis is divided into components which each solve a part of the hydroelastic and mooring problem. A flowchart of the interaction of program components is provided in Figure 3.1.

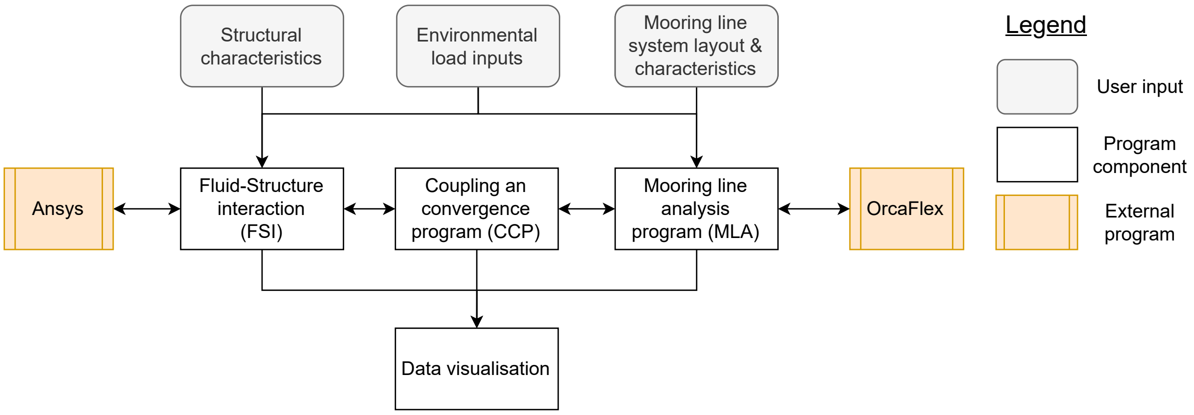

Figure 3.1: Overview of the hydroelastic and mooring line interaction program in which the Fluid-Structure Interaction is a component.

To provide the reader with a clear overview of the goals of each of the components as represented in the flowchart, the intended program is summarized below.

First the user is required to provide inputs in Python which characterize the problem to be solved by each of the program components. These inputs will be discussed in section 3.3. After the user has provided inputs, the Fluid-Structure interaction code instructs ANSYS to construct, mesh and calculate the structure shape as well as the structural mass and stiffness matrices. These are stored in the working folder. The mesh files are then used by the FSI component to construct a boundary element mesh used for solving the radiation-diffraction problem. The structural added mass and stiffness matrices are used to determine the structural damping. Finally, the displacement of the fairlead points on the structure are determined by solving the equation of motion (Equation 2.6).

The Mooring Line Analysis (MLA) component uses the Application Programming Interface by Orcina for OrcaFlex (OrcFxAPI) to model the mooring line system based on the user input and fairlead point locations as calculated in the FSI component. OrcaFlex determines the forces at the fairlead points of the mooring lines due to a displacement in location. These forces are provided back to the MLA component in Python. This component has to convert the mooring line induced forces from the time domain to the frequency domain.

The coupling and convergence helper component, incorporates the implementation of section 2.6. The effect of this component depends on the problem considered, and whether the mooring line forces lead to a convergent problem for the considered step.

Finally the Data visualisation component plots any results not covered internally by the other components.

3.2. Program design goals, languages, and packages

To develop the method as described in chapter 2 into functioning components of a working program it is necessary to consider and discuss the program design goals, the programming language(s), and external programs to be used. These are discussed in subsection 3.2.1, subsection 3.2.2, and subsection 3.2.3.

3.2.1. Design goals

To provide guidance for the implementation of the method based on the theory as presented in chapter 2, the numerical method goals as presented in section 1.4 are reiterated and program design goals are formulated.

Method design goals:

- Applicable in the initial stages of design, providing a balance between accuracy and efficiency.
- Applicable for different structure designs and mooring line system configurations.
- Applicable in three dimensions.

The program design goals mostly concern the user-friendliness of the program. The goals are therefore as follows.

- The amount of user inputs that the user has to provide should be kept to a minimum.
- The user is able to set all inputs necessary for the structure and mooring line characteristics
- The user should only have to interact with a single program, as opening and closing multiple programs is both cumbersome and prone to errors.
- The intended code should be understandable for people without programming experience.

3.2.2. Programming language

“A programming language is any set of rules that converts strings, to various kinds of machine code output. Programming languages are one kind of computer language, and are used in computer programming to implement algorithms” [74]. Many different programming languages are available in which the numerical method as described in this thesis can be written. Each of these languages has its own advantages and disadvantages. For the program discussed in this thesis both Matlab and Python were considered.

Matlab is a proprietary, closed-source software developed by Mathworks. A license has to be bought by the customer before the user is able to run the software. Matlab provides the base software and various add-ons named ”Toolkits” for which separate licences can be bought. Matlab is often used in academical studies, and students at the Delft University of Technology receive (instructional) courses in which the software is used and taught.

Python is a free, open-source software. No licenses are required before the user is able to run it. Python has many of the, if not the same, features as provided in Matlab. Individuals and groups using Python develop their own equivalent to ”Toolkits” called ”Packages” which can (largely) be used for free by installing and importing them. A downside is that no instructional courses for Python were provided in the study path followed by the author of the thesis.

As both Matlab and Python are able to do many of the same tasks, including the coupling with OrcaFlex, the focus is therefore on the disadvantages associated to each. The distinct disadvantage of Matlab is that if a user is unable to secure a Matlab license or does not have the ”toolkit” required for the program developed in this thesis, the program is unable to run. Although Matlab is available at Bluewater now, this is no guarantee for the future. Python inherently, due to its open-source nature, therefore provides a more future-proof outlook for the developed program in this thesis. Python however is a new language to be learned during the execution of this thesis.

To write the actual code a ”software editor” is required. This editor provides the user with an interface, debugger, and interprets and executes the code. Many options are available and in the choice for a specific editor is mostly based on user preference in terms of interface and application goal. The editor used is named ”Spyder”. ”Spyder is a free and open-source scientific environment written in Python, for Python, and designed by and for scientists, engineers and data analysts.” [55]. Spyder is chosen for simplicity and availability as it has been approved by the Information Technology (IT) department within Bluewater and is included in ”Anaconda” which also provides commonly used packages.

3.2.3. Structural software

Multiple FEA software packages exist that can be implemented to reach the goals stated in section 2.7. Examples are ANSYS, DIANA, ABAQUS, and COMSOL Multiphysics. Each of these software packages is able to calculate the structural outputs required in the thesis.

In the work described in this thesis the commercial program ANSYS is used. ANSYS is well known within the industry, available at Bluewater, and well documented.

The structural mass and stiffness matrices are determined by means of ANSYS Mechanical. ANSYS provides different program interfaces for the user. The graphical user interface (GUI) is what most people use and it provides the user with a structured program overview without showing the underlying code. The user can provide inputs and required outputs that are, via various code in the background, transformed into the required instructions for the program. The GUI method requires the user to start the program in the foreground and interact with the program itself for each required action.

The second option is to provide instructions via the ANSYS Parametric Design Language (APDL). The user writes all instructions in a Python script in APDL and instructs ANSYS Mechanical to execute the provided commands. This option allows the user to run ANSYS Mechanical in the background. ANSYS then outputs the results requested by the user.

One of the design goals for the numerical program is that the user only has to provide inputs once, without the need for the user to interact with different programs. The APDL approach is therefore preferable for the implementation within the numerical program described in this thesis.

3.3. Fluid-Structure interaction

In this section the actions taken in the Fluid-Structure interaction component are described in detail. This is described in the following parts:

- Initial structure mesh composition and modal analysis via Python - ANSYS APDL (section 3.3.1).
- Boundary mesh composition in Python (section 3.3.2)
- Panel parameters determination (section 3.3.3)
- Solving the radiation diffraction problem (section 3.3.4)
- Equation of motion matrices and vector composition (section 3.3.6)

A flowchart of the discussed items is provided in Figure 3.2, The goal of this flowchart is to illustrate the subdivision of parts in the FSI component and the programs in which the parts are housed. A flowchart providing an in depth view into the calculations and connections to other parts of the program is provided in Appendix D.

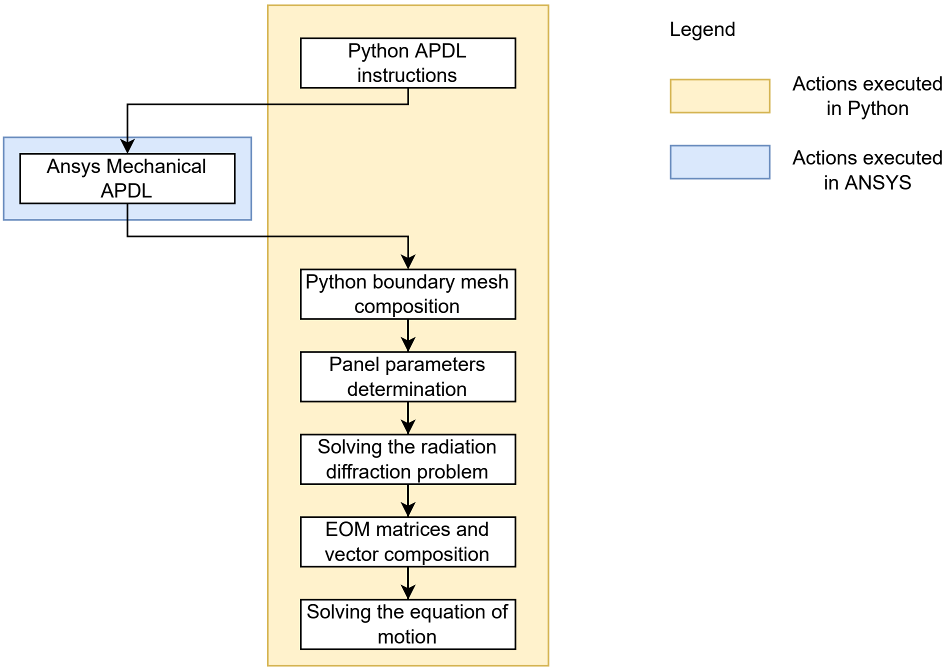

Figure 3.2: Subdivision of parts of the Fluid-Structure Interaction program

3.3.1. ANSYS APDL process

First, an instruction on how to run APDL code in ANSYS Mechanical is provided for the reader. Then structure characteristics are provided to ANSYS in Python via the ANSYS Parametric Design Language (APDL). The APDL input parameters and output files are listed in Table 3.1. A detailed description of the ANSYS process is given afterwards.

APDL scripting and execution in ANSYS

Earlier it was stated that ANSYS has two user interface options, the GUI and the external API, and that the external API uses APDL. An clarification should be added, useful for anyone trying to replicate the actions performed by ANSYS in this thesis. Applicable to anyone who has a valid ANSYS licence that includes a version of ANSYS Mechanical.

After installing ANSYS and the subpackage of ANSYS mechanical, in this case a commercial version of ANSYS 2021R2, the user can start the ANSYS Mechanical module from the computers task bar by searching for the ”$MechanicalAPDLproductlauncher2021R2$” app. ANSYS will then then start two programs as represented by windows on the taskbar see Figure 3.3. The left one is an output window and the right one the graphical user interface.

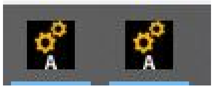

Figure 3.3: Taskbar overview of opened APDL programs by ANSYS

After clicking on the mechanical application the right symbol in Figure 3.3 the user provide code to ANSYS in the manner represented in Figure 3.4.

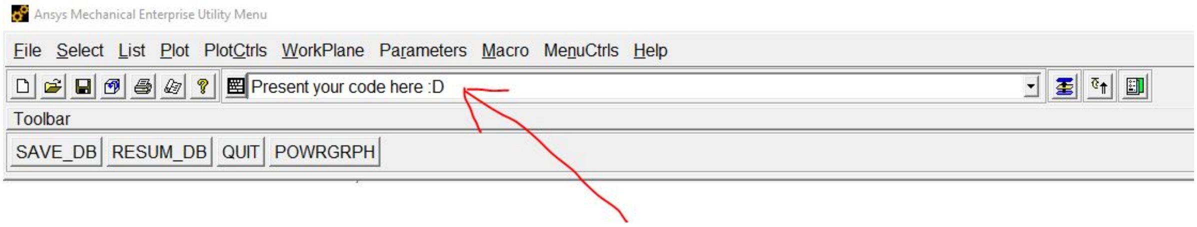

Present your code here :D

Figure 3.4: Script entry bar at the red arrow location in ANSYS Mechanical APDL

The mechanical scripting panel on the right side of Figure 3.4 can then be used to write and execute APDL code directly via the interface. The arrow on the right end of the input field allows for seeing previous written commands. Clicking on the output window, i.e. the left button in Figure 3.3, provides an overview of all ANSYS actions and error messages.

For APDL coding it proved invaluable to have access to the ANSYS APDL command manual as made available by the Budapest University of Technology and Economics [62]. The website in the reference provides descriptions for (likely) all APDL commands, with details describing the use of parameters and theory where available. These commands are unlikely to change between versions as they are the core functions by which ANSYS operates.

ANSYS structural inputs

ANSYS first requires details with respect to the structure that it has to model and do calculations on, these input parameters are presented in Table 3.1. For convenience the output files are presented in the bottom half of the table. The exact commands and naming of these files will be described in the next section.

The definition of the structure occurs in the pre-processor in ANSYS APDL which is started by means of the command $\backslash PREP7$. Next the material characteristics are defined by means of the command MP, X, Y, Z. X defines what characteristic is meant, i.e. isometric Youngs modulus (EX), Poisson’s ratio (PRXY), and material density (DENS). The y entry then ascribes the material characteristic to a material. The Z-value then contains the actual value that the parameter should have.

The APDL command BLC used in ANSYS to model the structure is used to create a block shaped structure.[1] It is chosen to construct the structure in such a manner that a corner is specified at x, y, and z equal to zero. All other corners of the structure then lie in the positive directions of the axes.

---

[1] It should be noted however, that with some adjustments, more complex structures can be modeled as long as quadrilateral surfaces can be determined. The Graphic User Interface (GUI) would likely be preferable for constructing the geometry.

User input parameters

Parameter	Description	Unit
L	Length of the structure	$[m]$
B	Width of the structure	$[m]$
D	Height of the structure	$[m]$
E	Youngs modulus	$[GPa]$
v	Poissons ratio	$[-]$

Stored output files

Filename	Description	File format
$AnsysActualDisplacements$	Original position of all nodes	$.CSV$
$ElData$	Topology: Couples node numbers to element number	$.CSV$
M	Sparse HB formatted structural mass matrix	$.txt$
M	Contains the mapping for the HB formatted file	$.mapping$
K	Sparse HB formatted structural stiffness matrix	$.txt$
K	Contains the mapping for the HB formatted file	$.mapping$

Table 3.1: APDL input parameters and output files

This choice of origin is a personal preference, as any point is allowed. The origin chosen at the corner provides an easy way to distinguish from the output file $AnsysActualDisplacements.CSV$ whether the structure was modeled correctly. With this preference the nodes on nine edges of the block always have a zero valued coordinate in the undeformed position. A sketch of the modelled structure and axes system is presented in Figure 3.5.

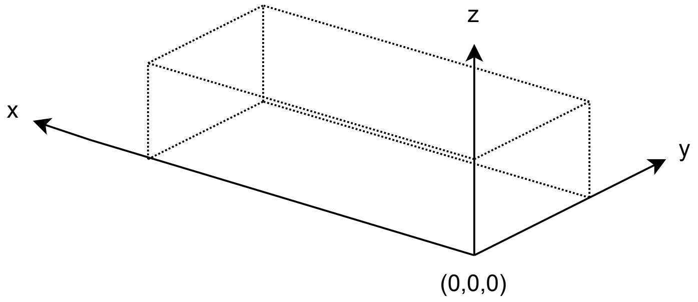

Figure 3.5: Origin and axes definition of the ANSYS structure

The choice was made to save all files in a Comma Separated File ($.csv$) format. In which the comma is the delimiter between values. The underlying reasons are as follows. A $.csv$ file can store a large amount of data, and is often used to interchange data between different languages. It also comes with the advantage that the file is readable in a text editor. In terms of data storage $.csv$ is not the most efficient, as it is surpassed by $.bit$ files, but the other advantages in this case outweigh this disadvantage.

Element options, considerations, and choices

In the finite element method the actual structure is approximated by a finite number of elements. These elements consist of vertices, edges and faces. The choice for an element depends on the application. In this thesis, the JIP floating structure is represented as a floating plate. The fluid interaction is calculated by means of the panel method (BEM). The requirements for the element are therefore as follows. Small deformations can be modelled accurately, and the structure can be subdivided in an appropriate number of similar-sized elements. In the design stage it is preferred that the element is able to work for various shapes and protrusions such as ballast bags.

The number and length of the elements is dependent on the required size of the panel for an accurate representation of the wave as discussed in subsection 2.7.2. The length of the element is also dependent on the height of the JIP structure. The JIP structure has a length to height ratio of roughly 50. The length of the sides of the element should always be smaller than the height of the structure as this is the smallest dimension.

In ANSYS two types of elements can therefore be considered suitable. The first is a solid element. Suitable for all shapes and the most accurate, but more expensive in terms of storage and calculation requirements. The second is a shell element, which is a two-dimensional abstraction of the solid element in which the third dimension is stored separately as thickness. Different shell elements are required for different length to height ratios, which makes it more difficult for changing designs. The choice for a shell element would therefor limit the method to shapes of a specific size, but comes with the advantage of both storage and calculation efficiency.

Wassee [70] offers further remarks on the choice, which are as follows. In terms of raw accuracy 3D quadratic elements are generally the most superior, if the hardware is capable then there is no reason to use shell or solid shell elements. Shell elements may require a lot of pre-processing and geometry preparation before the geometry becomes suitable for shell mesh generation. The choice for an element is therefore a judgement call based on the following. First, the amount of skill and experience of the user. Correct usage of shell elements require significant skill. Secondly, the level of result accuracy. Finally, the amount of time available.

The element implemented in this thesis is element $SOLID186$ as shown in Figure 3.6. In this figure the edges are represented by lines, the nodes by means of dots and letters, and the sides by means of numbers. $SOLID186$ is recommended for general structure shapes and therefore allows for the requirement for the design stage. The amount of experience and skill required for successful application is lower than for shell elements. A shell element is preferable in the future if only thin or thick plates are considered, as this requires less storage and is computationally more efficient. This choice however would also require more skill and experience for successful application.

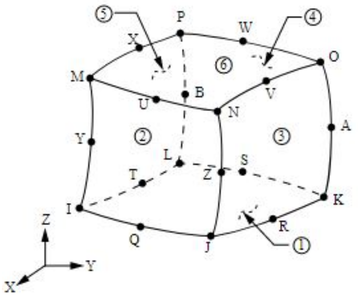

Figure 3.6: Representation of element SOLID186 [1]. Nodes represented by dots and letters, edges by means of solid and dashed lines, and element sides by means of numbers.

The element is implemented in ANSYS APDL by the command $ET, 1, SOLID186$, in which the element type (ET) is bound to the structural properties (1) and the element used is $SOLID186$. The element size is selected by means of the $ESIZE, x,,$ command in which x specifies the length of the element sides. The approach of setting one length for all sides is chosen to assure that even if the structure is rotated around its center, enough elements are available to capture the wave accurately.

The next step is the meshing of the structure, i.e. the discretization of the continuous structure in space by means of the user specified elements. The shape is meshed in three-dimensions by meshing the volume $VMESH, ALL,,$. A mesh check is then performed by ANSYS. The coordinates of the undeformed structure are written to the $AnsysActualDisplacement$ file.

When the structure dimension is smaller than the user defined length of the element, ANSYS will change the element length to be equal to the smallest dimension in the structure.

A single topology file $ElData.csv$, that relates nodes to elements is written. ANSYS provides the element nodes in a standard output sequence, this sequence is directed by the script lines to retrieve the element topology for the $ElData.csv$ file, see Figure 3.7. The sequence of nodes in the output file $ElData.csv$ should therefore always be the same unless this code is changed, more on this in subsection 3.3.2.

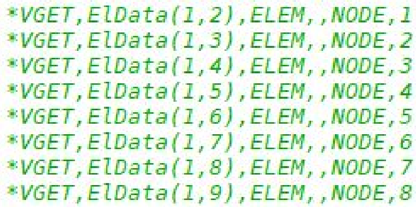

```
*VGET,ElData(1,2),ELEM,,NODE,1
*VGET,ElData(1,3),ELEM,,NODE,2
*VGET,ElData(1,4),ELEM,,NODE,3
*VGET,ElData(1,5),ELEM,,NODE,4
*VGET,ElData(1,6),ELEM,,NODE,5
*VGET,ElData(1,7),ELEM,,NODE,6
*VGET,ElData(1,8),ELEM,,NODE,7
*VGET,ElData(1,9),ELEM,,NODE,8
```

Figure 3.7: APDL script to store nodes in a specified sequence in the topology file

3.3.2. Python boundary mesh composition

Internal panels are not required for the boundary element calculation as described in paragraph 2.7.2. The goal is therefore to remove the internal panels created by meshing the structure with solid elements in ANSYS. The approach to achieve this goal is described below.

For the boundary mesh composition two files created by the APDL code are important. The first one $ElData.csv$ describes the topology: i.e. which nodes belong to which elements. The second one $AnsysActualDisplacements.csv$ describes the position of the nodes. Each element in ANSYS has a different topology and properties. A representation of element $SOLID186$ is provided once again for convenience in Figure 3.8.

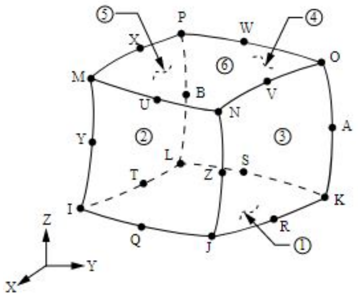

Figure 3.8: Element SOLID186 [1]

In Figure 3.9 two $SOLID186$ elements are displayed next together. By combining knowledge of the composition of the element used ($SOLID186$) and the $ElData.csv$ output file, the internal areas can be eliminated. In this process only the corner nodes of the elements are considered to make quadrilateral surfaces, the locations are marked by the numbers 1 to 12. The detailed elimination process will be described further below.

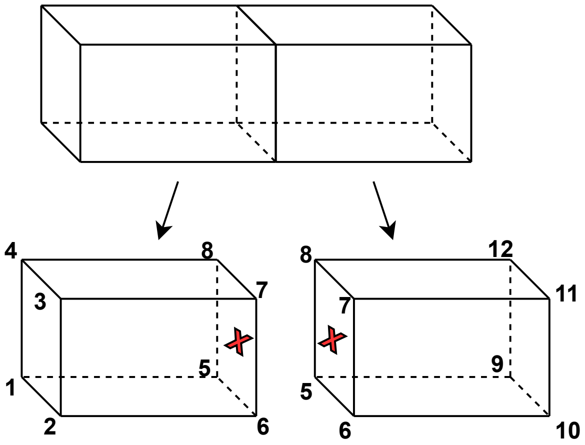

Figure 3.9: Boundary mesh composition by elimination of common surface areas between elements. To be eliminated panels represented by red crosses. The corner node locations are numbered as 1 to 12.

The first step in the elimination process is to delete the internal nodes (nodes A, B, Q, R, S, T, U, V, X, Y, Z in Figure 3.8). These are always located on the same entry column of the output file due to the output sequence provided through Figure 3.7. This leaves the corner nodes of the each element (I, J, K, L, M, N, O, P in Figure 3.8). As the sequence of nodes is always the same, the surfaces of the element always consist of the same entries in the topology file. When two elements are in contact with each other, as shown in Figure 3.9, the nodes at the points of contact must have the same node number. This is true even in cases where numerical inaccuracy would provide two slightly different locations. If the same vector occurs more than once, i.e. the nodes belong to two different surfaces, the panel is internal. If the vector occurs only once, it means that the panel is located on the surface of the structure and it will only have (for the simple cube geometry) two corner nodes that are used multiple times.

Figure 3.10 shows the initial collection of nodes (blue dots) for an arbitrarily sized structure on the left, and the resultant boundary mesh after the elimination of internal surfaces on the right. The edges of the outside panels on the structure are visible in the right figure as lines and the panels are grey. In the node plot (left side of Figure 3.10), it can be seen that all 20 nodes of each element are still considered. On the right hand side, the internal and non-corner nodes have been deleted and the panel edge lines run directly between the remaining corner nodes.

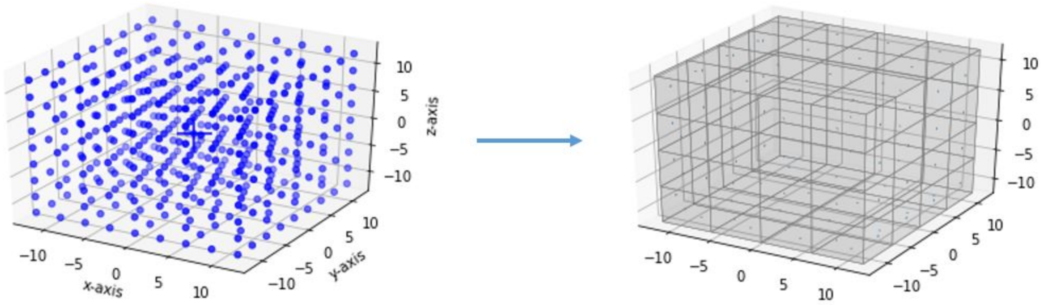

Figure 3.10: Elimination process: Left side: Representation of the original nodes (blue dots), right side: constructed panels for BEM (grey)

3.3.3. Panel parameter calculation

The next step is the determination of the panel characteristics required in further hydrodynamic calculation. The resulting panel parameters are based on four nodes on the panel corners and their respective order. The program abbreviations and descriptions for the panel parameters are given in Table 3.2:

Parameter	Description
v	nodes of the panel
D1, D2	diagonals of the panel
normal	normal unit vector of the panel
colp	collocation point on the panel

Table 3.2: Panel parameters and descriptions

The analytical expressions of the panel equations by Plotkin et al. [26], required in the source density and potential calculation are too numerous to be shown here in full. Therefore the most important ones for the determination of panel positions and distances are shown below.

The parameters required and used in the panel calculations are given in Figure 3.11. The corner nodes of the panel v (vertices: v1, v2. v3. v4) are required to determine the diagonal vectors that lie on the surface of the panel (D1 and D2). Vectors are created between the corner nodes (d12, d23, d34, d41 denoted in red). Point Q is the location of the field point at which the unit source distribution is evaluated for the panel. The distance between the vertices and Q is denoted by r1, r2, r3, r4 (dotted lines), which are required for the calculation of the velocity potential of a panel due to a unit density source distribution over that panel. The panel parameters are determined with respect to a local panel coordinate system for which the axes are denoted as X, Y and Z in Figure 3.11. All of these parameters are required to determine the source strength distribution over the wetted surface area of the structure.

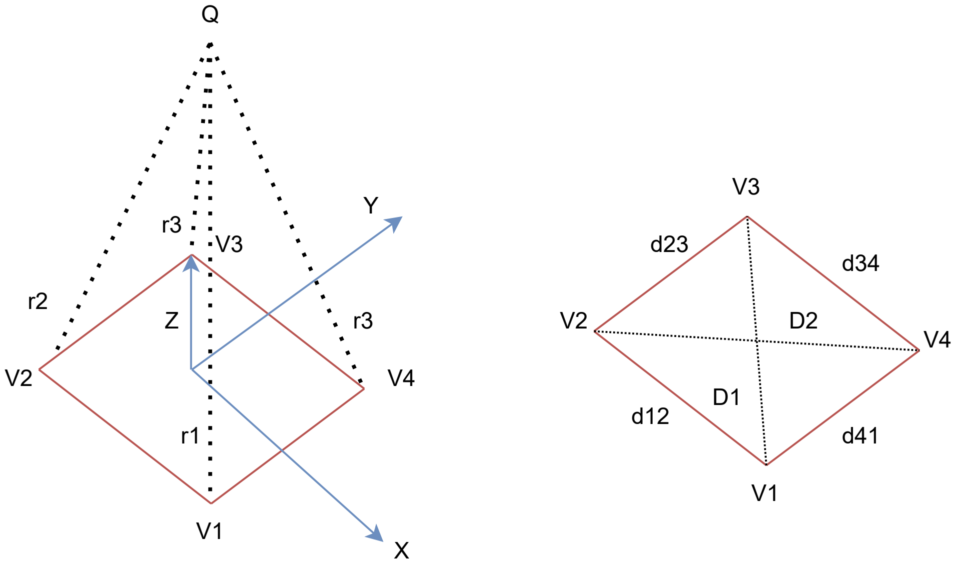

Figure 3.11: Panel parameters and their locations on a single panel, amended from [26] and [68]

The diagonal vectors are determined by means of Equation 3.1.

$$D_n = V_{n+2}(x, y, z) - V_n(x, y, z) \tag{3.1}$$

The cross product of the diagonal vectors ($D1$ and $D2$) provides the normal of the panel pointing outward into the fluid. Assuming that the nodes on the panel are provided in a manner as seen in Figure 3.11 with n equal to 1 or 2. The normal vector is then calculated by means of the cross product between $D1$ and $D2$ as shown in Equation 3.2, and normalized by means of Equation 3.3.

$$\vec{n} = \vec{D_2} \times \vec{D_1} \tag{3.2}$$

$$\vec{n_i} = \frac{\vec{n}}{|n|} \tag{3.3}$$

The panel edge vectors $(d_{12}, d_{23}, d_{34}, d_{41})$ values are calculated by means of Equation 3.4-Equation 3.7 and are required in the calculation of the centroid position on the panel.

$$d_{12} = \sqrt{((x_2 - x_1)^2 + (y_2 - y_1)^2)} \tag{3.4}$$

$$d_{23} = \sqrt{((x_3 - x_2)^2 + (y_3 - y_2)^2)} \tag{3.5}$$

$$d_{34} = \sqrt{((x_4 - x_3)^2 + (y_4 - y_3)^2)} \tag{3.6}$$

$$d_{41} = \sqrt{((x_1 - x_4)^2 + (y_1 - y_4)^2)} \tag{3.7}$$

The secondary inputs required to determine the location of the centroid of the panel are the halfway points (c) between the four vertices, named c_1, c_2, c_3, see Equation 3.8 in which n is equal to 1, 2, 3. c_4 is calculated by means of Equation 3.9.

$$c_n(x, y, z) = \frac{c_n(x, y, z) + c_{n+1}(x, y, z)}{2} \tag{3.8}$$

$$c_4(x, y, z) = \frac{c_4(x, y, z) + c_1(x, y, z)}{2} \tag{3.9}$$

The location of the centroid of the panel for a quadrilateral (col) can then be determined using Equation 3.10 in which i is the x, y or z coordinate and d is the summation of $d_{12}, d_{23}, d_{34}, d_{41}$.

$$col(i) = \frac{c_1(i)d_1 + c_2(i)d_2 + c_3(i)d_3 + c_4(i)d_4}{d} \tag{3.10}$$

The calculated values are stored in a vector for each panel. These vectors are then stored in a two-dimensional tabular format called a $DataFrame$ from the package $Pandas$. This storage format has to advantages. The first is that it makes stored data easy to read. The second is that the values are color graded and deviations are therefore more easy to spot.

After these panel parameters have been determined it is recommended to check whether the calculations up to this point have been executed correctly. Therefore before proceeding further the ways in which the output can be checked is described. A change in APDL or Python code used for mesh construction can result in specific program errors, Which usually represent themselves in one of the following ways:

1. The program reports that a specific file is unavailable.
2. The program reports that non-valid values are used in the calculations.
3. The diagonals are determined incorrectly, or the normal vectors are inverted.

The first two errors will be reported internally in the Python console. The third error is one that can slip through as Python is happy to provide results based on wrong input values. Two verification implementations for the third error are now presented. The first is a visual representation (plot) of the panels and the parameters. The second is by means of a comparison file and a unit test.

In the panel parameter calculation the normal vector, diagonal vector, and panel edge vector values are dependent on each other and on the provided input files. It is therefore possible for simple structures to visually verify correctness of the executed calculation. Plots used to determine whether the diagonals and normal vectors were calculated correctly are provided in Figure 3.12a & Figure 3.12b. In the left sub-figure the diagonal vectors are represented by a dashed blue line and the panel edges by a black

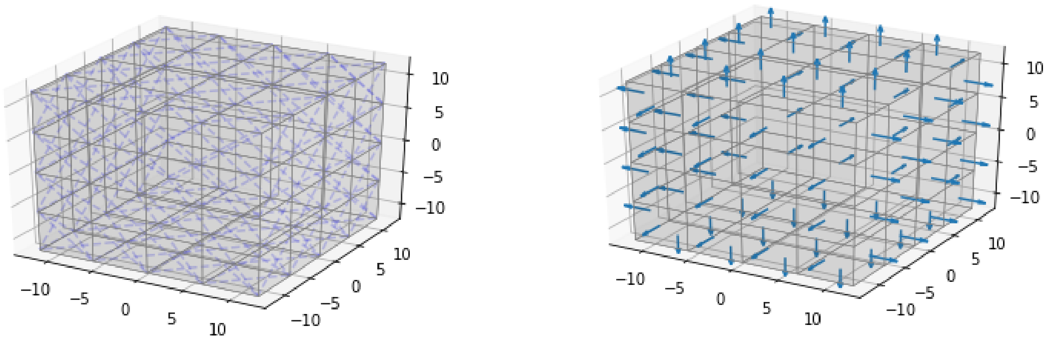

(a) Diagonal vectors represented by dashed blue lines

(b) Normal vectors represented by the blue arrows pointing towards the fluid.

Figure 3.12: Resultants of the panel calculations

solid line. In the right sub-figure the normal vector to the surface of the panel is represented by means of a blue arrow.

The second approach to combat wrong calculations is by means of the implementation of a unit test. The goal of a unit test is to isolate pieces of code and to verify whether it works as originally intended. In the code this is implemented as follows. First a model with specific input values is created via APDL, which results in the input files for Python. Then boundary mesh and panel parameters are calculated and written to a comparison file in .csv format. For the verification inputs provided to ANSYS, the results as intended are known and stored in a verification file. By comparing the unit test comparison file with the verified file the proper working of the method for both the meshing and the panel calculation can be determined.

This procedure is recommended when the code is stored in a shared user folder, and changes in code are not solely dependent on one user. To ensure that changes to the code can be rolled back to a verified version a version control program such as GIT [15] can be used.

3.3.4. Solving the radiation potential problem

The hydrodynamic calculation is based on the suggested implementation by McTaggart [33] and Guha [16]. The required user inputs for this part of the FSI program are given in Table 3.3:

Parameter	Description	Unit
ω	wave frequencies	$[\frac{rad}{s}]$
wave dir	wave direction	$[deg]$
water depth	water depth	$[m]$

Table 3.3: User inputs radiation-diffraction problem

To illustrate the difference between a rigid potential solver, and the one implemented the difference in application goal and approach is described below.

Rigid body radiation potential solvers assemble a 6x6 matrix per frequency for both the added mass and hydrodynamic damping. This is possible as the motion of a single point in the structure can be determined, and the motions of the other points in the structure can be deduced based on the rigid body behavior and relevant distances.

In the case of hydroelasticity the motion is dependent on the position of multiple nodes on the body as the structure is flexible. The displacements of points on the body are dependent on the individual node contributions of the added mass and damping, along with the stiffness and exciting force on the node. The six degrees of freedom for a node consist of surge, sway, heave, roll, pitch, and yaw. Referring back to Equation 2.51 to Equation 2.53 the entry n_{k_p} referred to the generalized normal. This vector can be calculated by first calculating the normal vector (n) as previously detailed in Equation 3.2.

Then, the generalized normalized vector, see Equation 3.3, provides the normal directions in surge (n1), sway (n2), and heave (n3). For the roll (n4), pitch (n5) and yaw (n6) directions Equation 3.11 need to be calculated. In which $\vec{r}$ is a vector between the origin to a point on the surface, which is determined in Equation 3.10.

$$(n_4, n_5, n_6) = \vec{r} \times \vec{n_i} \tag{3.11}$$

In subsection 2.7.2 the α and β matrices were mentioned, but no explanation was given on how the components of α and β were determined. This was partly because the theory given was to provide an overview of the solution process in the linear potential theory, and partly as it is easier to explain along with the implementation. Both the integral functions and the to be implemented functions are given.

The α and β matrices consist of both inputs of the source density distribution, and the source density due to oscillations. Equations by Hess & Smith [17] are given in Equation 3.12 and Equation 3.13. In which $\tilde{G}$ is the wavy part of the Greens function which can be implemented using the code by Telste & Noblesse, which will be discussed below.

The two other terms r and r' are the parts dependent on the real and imaginary panels and are independent of wave frequency. The functions and implementation are described by [19], and has been implemented in [16].

$$\alpha_{ij} = \frac{1}{2\pi}\int_{\Delta S_j} \frac{\delta}{\delta n}\frac{1}{r} dS + \frac{1}{2\pi}\int_{\Delta S_j} \frac{\delta}{\delta n}\frac{1}{r'} dS + \frac{1}{2\pi}\int_{\Delta S_j} \frac{\delta \tilde{G}_0}{\delta n} dS \tag{3.12}$$

$$\beta_{ij} = \frac{1}{4\pi}\int_{\Delta S_j} \frac{1}{r} dS + \frac{1}{4\pi}\int_{\Delta S_j} \frac{1}{r'} dS + \frac{1}{4\pi}\int_{\Delta S_j} \tilde{G} dS \tag{3.13}$$

Guha [16] states that the normally the wavelength is large with respect to the panel size and this allows for the approximation of the required integrals at the centroid of the panels and multiplication of the integrands by ΔS_j. As the wavelength for hydroelasticity is smaller, it is therefore very important to use the panel size rule of thumb discussed earlier to guarantee that this assumption is allowable.

To determine the wavy part of the Greens function the FORTRAN code as made available by Telste Noblesse [63] has been written. The FORTRAN code is converted to a $.exe$ format using the GCC compiler [61]. A list of h and v values are calculated based on Equation 2.31 and Equation 2.32. Which are stored for each panel in a text file named $aap.txt$. The executable is then executed and uses the created $aap.txt$ file as input. It then creates an output file named $noot.txt$ in which the calculated R0 and R1 values are stored. With these values Equation 2.35 and Equation 2.36 can be determined. Finally resulting in expressions for the wavy parts of the Greens function in Equation 3.12 and Equation 3.13.

The normal velocities v_i for each DOF on the surface of the panel can then be determined by means of Equation 3.14. In which n_i are the generalized normal coordinates.

$$\vec{v_i} = i\omega n_i \tag{3.14}$$

Then by solving the Equation 2.49 source density values (σ) are determined, and used in the calculation of Equation 3.15. In which for the radiation potentials i is 1 to 6, and for the scatter wave potential i is 7.

$$\phi_i = \beta\sigma_i \tag{3.15}$$

After determining the radiation potentials in the manner described above, the added mass and damping matrices can be determined by means of Equation 2.22 and Equation 2.21. Which can be implemented almost one to one in the code.

The scattered wave potential is now the only unknown, but can be determined in a similar manner by means of first calculating the associated body boundary vn_d condition given in Equation 3.16.

$$vn_d = -\frac{\delta\phi_0}{\delta n(\vec{x})} \tag{3.16}$$

Going through the same process as for the radiation potentials, i.e. multiplication with the inverse of α and then multiplication of the resulting source density with the β matrix results in the scattered wave potential. To avoid calculating the incident wave potential ϕ_0 is stored. This concludes the solving of the radiation and diffraction problem.

3.3.5. Fluid matrix and vector calculation and composition

In the previous section the implementation of solving the radiation problem was discussed and the results are an expression for the radiation, scattered wave and incident wave potential. Substituting the radiation potentials into Equation 2.22 and Equation 2.21 provides us with the coefficients for the added mass and damping for each frequency in the list of provided wave frequencies for each panel.

To determine the correct coefficient values for the added mass and damping, which are not included in the original user specified frequencies, an interpolation calculation is executed. The inputs for the interpolation function are the wave excitation frequency, the added mass and damping coefficients calculated via the input frequencies, and the order of the polynomial. In the program the polynomial is set to a ninth order approximation as the provided frequency range is user dependent. In theory when the value needs to be determined between two points a first order approximation would be sufficient.

In the implementation used, the full range of wave frequencies is used to determine the correct value. Using a first order approximation on all values would result in smoothing if sudden peaks occur in the data set for the coefficient values and the frequency step chosen is not small. Smoothing could result in erroneous values for the added mass and damping, which can translate into errors for the eigenfrequency of the structure and over or under damping. The difference in computational requirements is almost negligible as there are only 81 data points in the largest considered data set of wave frequencies (start 0.025, step 0.025, stop 2.025 [rad/s]). The choice is therefore made to be cautious and use a high order polynomial.

The acquired added mass and damping coefficients are then equally split over the four nodes on the panel. For nodes belonging to multiple panels the coefficient is a summation of the individual panel contributions, see Figure 3.13.

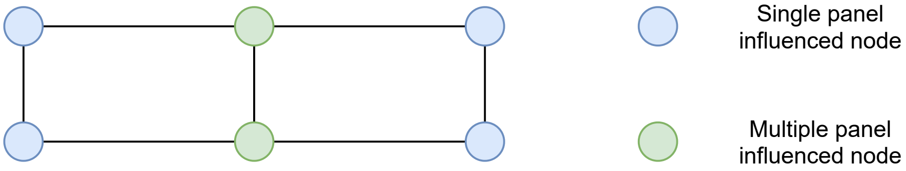

Figure 3.13: Node coefficient contributions. Single panel influenced nodes in blue, multiple panel influenced nodes in green, panel edges in black

To allow for arbitrary incident wave angles in the calculation of the exciting wave forces, the following method is used. The regular wave profile in three-dimensions can be considered as two-dimensional (x, z-axis), see Figure 3.14.

To determine the amplitude of the wave approaching the structure for an arbitrary incident angle (alpha), the structure is rotated about the z-axis by the incident angle. The x-directional distance to each panel centroid is determined. Based on this distance the wave elevation can be calculated at a specified time at a panel centroid location. A sketch of the process is provided in Figure 3.15. In which x and y are the origin axis of the structure.

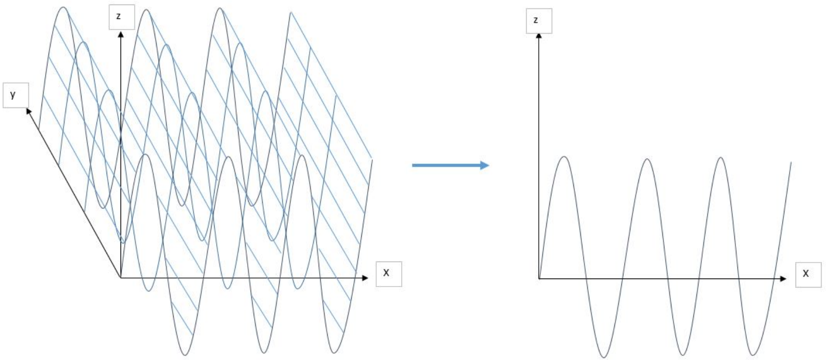

Figure 3.14: Expressing a 3D regular deep water incident wave (left) as a 2D wave in x and z-direction (right)

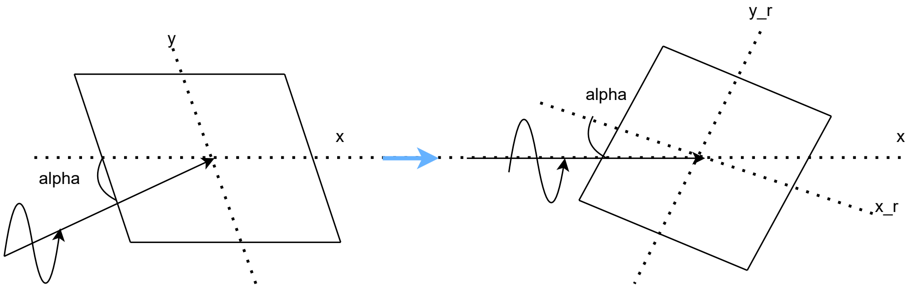

Figure 3.15: Rotation by angle alpha of the structure to simplify the incident wave to a two-dimensional function. x and y denote the original axes, x_r and y_r the rotated axes of the structure. The wave is represented by means of the sinusoidal black arrow, and the direction of propogation as a straight black arrow.

The exciting wave forces are calculated according to Equation 3.17, which is a function of the water density (ρ), wave frequency (ω), generalized normals (n_i), panel area (ΔS_p)and time (t). The centroid calculated force coefficients are split over the panels nodes equally and contributions to each node are summed together.

$$F_k^e(\omega, t) = [-i\omega\rho(\phi_{0_p}^{\omega} + \phi_{7_p}^{\omega})n_i\Delta S_p]e^{i\omega t} \tag{3.17}$$

3.3.6. Equation of motion matrices and vector composition

Now that a value is stored for each wetted node for the added mass, damping, and wave exciting force. The next step is composing these in such a way that the coupled problem of structure and fluid can be calculated as per Equation 2.6. This is not straightforward and requires additional actions below.

Remembering the output files as created in Table 3.1, and specifically the M and K text and mapping files. These files are created by ANSYS in a format called Harwell-Boeing, which is a sparse matrix file. The Harwell-Boeing format is the only option for the current developed method as it is the only file format that also provides the node numbers and degrees of freedom which are needed for the direct coupling of the fluid and structure.

This sparse matrix format is convenient as it saves disk space when the file is not used. However for the calculation full matrices for the mass and stiffness need to be transcribed. A problem is however that no transcription codes are available for Python use. In this thesis therefore such a code has been written, which is provided in appendix C. This code uses the .txt and .mapping files to formulate a structural matrix with row and column names that are node dependent, the resulting matrices are once again stored as DataFrames in Python.

The stiffness matrix is composed by implementing the equations given in Equation 2.7.2. In this case the matrix is calculated in full for the entire structure. The values for the coefficients are divided by the number of wetted nodes. This matrix is frequency independent so no interpolation is required.

The added mass $A(\omega)$ and stiffness C_s matrices are then added to their respective wetted node locations in their structural mass and stiffness matrices. A simplified case for one node (N) is shown for the mass matrix in Equation 3.18. The same example is applicable for the addition of the stiffness matrices.

$$\begin{vmatrix} M^N_{str,11} + A^N_{11} & ... & ... & ... & M^N_{str,16} + A^N_{16} \\ ... & M^N_{str,22} + A^N_{22} & ... & ... & ... \\ ... & ... & M^N_{str,33} + A^N_{33} & ... & ... \\ ... & ... & ... & ... & ... \\ M^N_{str,61} + A^N_{61} & ... & ... & ... & M^N_{str,66} + A^N_{66} \end{vmatrix} \tag{3.18}$$

When the user wants to consider Rayleigh damping. The user has to provide input values α_1 and α_2 for the Rayleigh damping, which are respectively α and β in Equation 2.43, and sets the Rayleigh damping to ”yes”. The structural Rayleigh damping matrix is determined from the user specified damping and the structural mass and stiffness matrices. The structural Rayleigh damping is then combined with the hydrodynamic damping in the same manner as described for the mass matrices in Equation 3.18. In the case that Rayleigh damping is not included, the structural mass matrix is copied, emptied of values and the hydrodynamic damping values are added. This concludes the last matrix composition required for the equation of motion.

The force vector shapes for the exciting wave force vector and the mooring force vector are deduced from the mass matrix, to keep the same mapping convention. This is simply achieved by compressing the N x N matrix to a N x 1 vector and filling it with zeros. The wave exciting force contributions for each node are added to their respective positions in a copy of this vector. The mooring line force contributions are filled into the fairlead node positions of a empty copy of the force vector. The final summation of the wave force vector and the mooring line vector results in the full description of the considered forces in the equation of motion for each mode.

To find the displacements at specific measurement locations a short Python script is implemented that finds the nearest node location to the point specified. This can be calculated using the minimum Euclidean distance, see Equation 3.19. In this equation x_n, y_n, and z_n are the respective nodal coordinates, and x_{sp}, y_{sp}, and z_{sp} are the user specified coordinates. The expression min is a function that finds the minimum for all the calculated distances.

This script is executed for the original node locations at the start. The resultant nodes numbers are then stored in a data frame format. This data frame is called upon when the equation of motion is solved and results need to be extracted for storage or plotting.

$$Closestnode = \min \sqrt{(x_n - x_{sp})^2 + (y_n - y_{sp})^2 + (z_n - z_{sp})^2} \tag{3.19}$$

3.3.7. Solving the equation of motion

In the previous sections the process and implementation for retrieving the fluid and structural matrices and force vector has been described. In this section the equation of motion is composed, and solved. For this an overview of the shape of each of the resultant matrices and vectors is given.

The structural matrices as found by ANSYS have been transcribed in an N by N matrix consisting of 6 by 6 submatrices for each node N. The added mass and damping matrices have been added to the wetted nodes, resulting in N by N matrices consisting of 6x6 submatrices, with a similar mapping as the structural matrices. The force vector is a N by 1 matrix, in which for each N a 6 x 1 vector is available.

In theory it is possible to solve this system in a modal way, by pre- and post multiplying it with the modal eigenvector matrix. This would uncouple the system and would likely be faster than the implemented method of brute force applied now.

First the force vector is is split up in the sinusoidal and cosinusoidal components of $e^{i\omega t}$. Then the equation of motion is rewritten to achieve an equation in which the unknown deformation (ζ) is the result of the known matrices and vectors, see Equation 3.20. In which the suffix i for the force vector $F_{k,i}$ represents either the sinusoidal or co-sinusoidal force vector.

$$\vec{\zeta} = \frac{\vec{F}^{e}_{k,i}(\omega, t)}{-\omega^2(M^{str} + A(\omega)) + i\omega(B(\omega) + B^{str}) + K^{str} + C} \tag{3.20}$$

The equation of motion is solved twice for each force vector, giving a displacement vector for the sinus (u_s) and co-sinusoidal part (u_c). The absolute displacement vector is taken and provides a co-sinusoidal ($\hat{u}_c$) and sinusoidal ($\hat{u}_s$) amplitude for each node in the vector. Then the phase of each the solutions is determined (θ_c, θ_s). Combining the solutions via Equation 3.21 then gives the final nodal displacement values for all nodes.

$$\vec{u} = \hat{u}_c cos(\omega t - \theta_c) + \hat{u}_s sin(\omega t - \theta_s) \tag{3.21}$$

From all of these solutions, the interesting ones are the measurement or fairlead locations specified by the user. As the resulting displacement vector ($\vec{u}$) still has the same mapping. Nodes closest to the locations defined by the user were determined by Equation 3.19, and stored in a DataFrame. The stored node names are now used to find the corresponding displacements. The data is plotted in one plot, and results are written to a DataFrame named $Data$.

The following chapters only describe the actions taken to verify and validate the fluid-structure interaction model as discussed above.

4

Verification

In this chapter the verification of the fluid-structure interaction part of the program will be provided. The verification steps undertaken in this chapter are the following.

First the structural mass and stiffness matrices are verified by executing some simple tests and comparing the associated mode shapes with those found in literature. Then the implementation of the hydrostatic stiffness is verified by means of an analytical calculation and determining the response of the structure to a long-crested (small incident wave frequency) wave and comparing this with expectations. A convergence test is executed to determine whether the linear potential solver converges to a singular solution for the added mass, hydrodynamic damping coefficients and force components.

The implementation of the regular deep water waves as implemented in the program is compared to theory. To test whether the model can simulate a flexible structure, the structure is subjected to a regular wave and the phase difference in peak amplitude is compared between the different measurement locations. Finally, to determine whether the rotation of the structure has been implemented correctly the incident wave angle is changed and results are compared with expectations.

4.1. Structural mass and stiffness matrices

In the equation of motion the structural mass and stiffness play a large part. Not only do they influence the motions at high and low frequencies, but the combination of both in a Rayleigh damping matrix will impact the mid frequency range. It is therefore necessary to determine whether the outputted files by ANSYS can be trusted. By verification of the parts (mass and stiffness) the whole can be verified (damping).

The ANSYS output format is transcribed from the Harwell-Boeing format as described earlier. This however does make verification more difficult as this also scrambles node values throughout the matrices. The mass and structural matrices are therefore often not ordered in an easy to understand way. Two simple checks can be executed for the mass matrix however. The first is that no values are expected on the off-diagonal entries for the UX, UY, and UZ entries of each node. The second is that the mass matrix should always be positive definite. Checking the transcribed matrix shows that the structural mass matrix is correct for both these checks.

The structural stiffness matrix is more difficult to verify. The main diagonal should be filled, but the off-diagonal entries are dependent on whether a node interacts with a second node. These values can be positive or negative. The transcribed stiffness matrix has a full diagonal, with coupling between nodes on the off-diagonal.

The inputs of the matrices have been been checked indirectly by comparing mode shapes for a plate as found by Senjanovic [52] with the mode shapes found via the files produced by ANSYS. The mode shapes seem to be consistent on visual comparison. The optimal way to compare the two is to find the

Abbreviation	Description	Value	Unit
ω	Wave frequency	0.1	$[\frac{rad}{s}]$
k	Wave number	0.001	$[\frac{1}{m}]$
$ampl$	Wave amplitude	0.2	$[m]$
x	location of evaluation	0	$[m]$
t	time of evaluation	30	$[s]$

Table 4.1: Input parameters for the theoretical wave equation

relative difference between the two. This however is not possible as the scale factor used is unknown and no mode shape data further than figures is provided.

A last method is available to check the correctness of the mass matrix as retrieved by ANSYS, which is the summation of mass components. As the mass for the full matrix is subdivided over the elements and all the mass of those elements is divided over the associated nodes of that element. It is possible to check whether the full mass is present in the nodal mass matrix as retrieved by ANSYS. For a simple overview see Figure 4.1, in which a single element has its mass divided over two nodes.

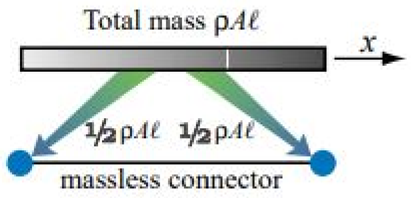

Figure 4.1: Total mass division into lumped masses at nodes (blue circles) on an element (mass-less connector), from [50]

Combining the fact that ANSYS is an industry leader on the subject of FEA and that an error in the implementation of the mass and damping would be very unlikely as it is used in almost every model, and the matrices passing the simple checks above, the mass and stiffness matrices are highly likely to be correct.

4.2. Numerical versus theoretical incident wave

To verify whether the implemented wave is modelled correctly by the numerical method the undisturbed wave is compared to the theoretical wave. The expectation is that these are the same, as the equation used can be translated almost one-to-one into Python.

The equation for the theoretical deep water wave elevation (η) is given in Equation 4.1. In this equation ζ_w is the wave amplitude k is the wave number, x is the location where the wave is evaluated, t is the time at which the wave is evaluated.

$$\eta_w = \zeta_w(cos(kx)cos(\omega t) - sin(kx)sin(\omega t)) \tag{4.1}$$

Using the wave characteristics as given in Table 4.1 and substituting them in Equation 4.1 results in a value of -0.198 meters.

The numerically calculated theoretical wave is shown in Figure 4.2.
From Figure 4.2, the wave elevation at 30 seconds is -0.198 meters. By changing the time of evaluation it is possible to verify each point in the presented wave. This shows that the numerically calculated wave is indeed equal to the theoretical wave. The numerical method waves are therefore correct and usable for both verification and validation of other components of the program.

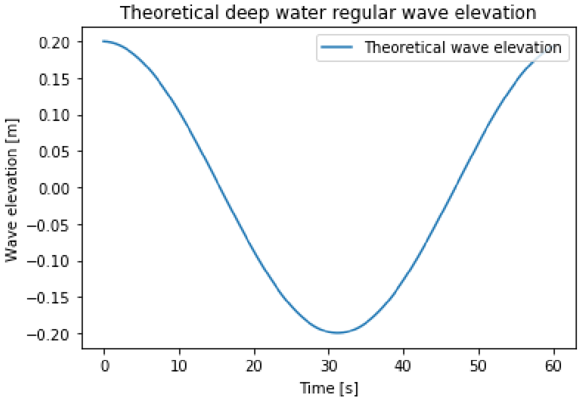

Figure 4.2: Numerically calculated theoretical regular deep water wave. Wave period of 62.8 seconds, wave amplitude of 0.20 meters

4.3. Hydrostatic stiffness

To determine whether the implementation of the hydrostatic stiffness was executed correctly, the verification is executed in three steps. First, the heave coefficient for the hydrostatic stiffness is compared to an analytically calculated value. Secondly, a test is undertaken with a long-crested wave. Finally, the response of an undamped structure to a higher incident wave frequency is tested. In these tests the structure characteristics as represented in Table 4.2 are used.

4.3.1. Test 1: analytical comparison

First the hydrostatic stiffness value for the heave coefficient is verified by means of calculating the analytical value via Equation 4.2.

$$C_{33} = \rho_w g L B \tag{4.2}$$

Substituting the values in Table 4.2 in Equation 4.2 results in an analytically calculated value of 1.0558e6 $[kg/s^2]$. Running the numerical model gives a heave coefficient of 1.0558e+06 $[kg/s^2]$, and therefore a perfect match for the coefficient.

4.3.2. Test 2: coefficient implementation

Now that the calculation of the heave coefficient was successful, the correct implementation in the structural stiffness matrix can be verified in the manner described below.

In this test a long-crested (very low wave frequency) wave is sent towards the structure. For very low wave frequencies the contribution of the mass and damping terms in the equation of motion Equation 2.6 drops significantly. Therefore the equation of motion (Equation 2.6) can be approached/rewritten as a product of the stiffness matrices (K and C) and exciting wave force (F), see Equation 4.3.

$$K + C = F \tag{4.3}$$

The expected response of a floating structure to a long-crested wave is that the structure will follow the wave at the same height as the amplitude of the incident wave. The long-crested wave characteristics chosen are provided in Table 4.3. The associated wave length (λ) and period (T) are calculated via Equation 4.4 and Equation 4.5, which are valid for a deep water wave.

Abbreviation	Description	Value	Unit
L	Length	15	$[m]$
B	Width	7	$[m]$
H	Height	0.5	$[m]$

Table 4.2: Characteristics hydrostatic tests

Abbreviation	Description	Value	Unit
ω	Wave frequency	0.1	$[\frac{rad}{s}]$
T	Wave period	62.8	$[s]$
ζ	Wave amplitude	0.2	$[m]$
λ	Wave length	6157.6	$[m]$
α	Incident wave angle	0	$[deg]$
$Oxyg$	Origin wave	-25	$[m]$
ele	Panel length and width	0.5	$[m]$
t	time step	0.01	$[s]$

Table 4.3: Wave and panel characteristics

$$T = \frac{2\pi}{\omega} \tag{4.4}$$

$$\lambda = \frac{gT^2}{2\pi} \tag{4.5}$$

The measurement locations are provided in Table 4.4.

X [m]	Y [m]	Z [m]	Node number [-]
-6	0	-0.25	739
-3	0	-0.25	751
0	0	-0.25	763
3	0	-0.25	775
6	0	-0.25	787
-6	3	-0.25	211
-3	3	-0.25	223
0	3	-0.25	235
3	3	-0.25	247
6	3	-0.25	259

Table 4.4: Measurement locations hydrostatic stiffness test

The resultant heave displacements for the measurement locations are provided in Figure 4.3.

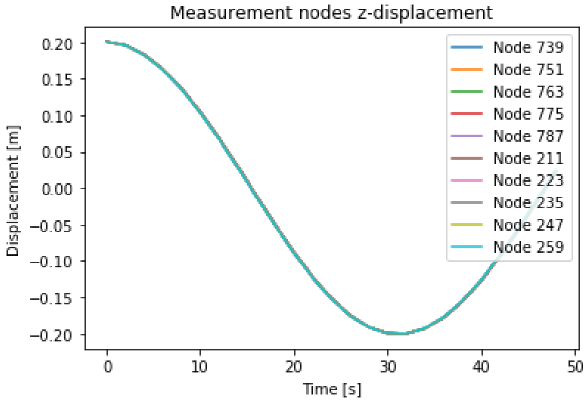

Figure 4.3: Response to a long-crested wave. Time in seconds on the x-axis, displacement of nodes in meters on the y-axis.

From Figure 4.3 several things can be determined. The wave is modelled correctly; this can be deduced from the half wave period as found in the figure and comparing it with the calculated wave period in Table 4.3. Damping is not relevant at this frequency, as this would be noticeable as a decreased maximum amplitude. Finally, and most importantly the displacement in the heave direction at the measurement locations follow the wave elevation at their respective locations as expected.

4.3.3. Test 3: phase differences

In the previous hydrostatic test the hydrostatic stiffness implementation was verified, but it did not provide any information on whether the flexibility of the structure is modelled. To test this, a higher wave frequency wave is used. The values used in this test are provided in Table 4.5.

Abbreviation	Description	Value	Unit
ω	Wave frequency	1.5	$[\frac{rad}{s}]$
T	Wave period	4.2	$[s]$
ζ	Wave amplitude	0.1	$[m]$
λ	Wave length	27.4	$[m]$
α	Incident wave angle	0	$[deg]$
$Oxyg$	Origin wave	-25	$[m]$
ele	Panel length and width	0.5	$[m]$
t	time step	0.01	$[s]$

Table 4.5: Wave and panel characteristics 2

The expected result is a difference in peak time at each measurement location (phase difference). The results at measurement locations at the same x-coordinate will overlap, as the corresponding wave height is the same. The difference in time between peaks can then be calculated via Equation 4.6.

$$V_p = \frac{\omega}{k} \tag{4.6}$$

Assuming deep water conditions the wave number (k) can be written as Equation 4.7.

$$k = \frac{\omega^2}{g} \tag{4.7}$$

Substituting this into Equation 4.6 gives an expression for the phase velocity in terms of the wave frequency (ω) and gravity (g), see Equation 4.8.

$$v_p = \frac{\omega}{\frac{\omega^2}{g}} = \frac{g}{\omega} \tag{4.8}$$

In Equation 4.8 v_p is the phase velocity. When the wave frequency is directly proportional to the wave number, the wave travels undisturbed at this frequency. Substituting the values provided in Table 4.5 gives an expected velocity of 6.54 meters per second. The distance between subsequent measurement locations is 3 meters. The time to overcome that distance with the wave frequency is therefore expected to be $\frac{3}{6.54}$ = 0.459 seconds.

Running the numerical method with the values provided results in Figure 4.4.
In Figure 4.4 two lines have been drawn at subsequent measurement locations. The time difference between peaks for subsequent locations is calculated based on the time values determined at the vertical lines. This shows that at 1.55 seconds the value for node 259 is -0.6585 and node 247 reaches this value at 2.01 seconds. The difference is therefore 0.46 seconds, which is as expected.

4.4. Radiation and diffraction tests

In this section the added mass, hydrodynamic damping and hydrostatic damping are verified by comparison of numerical results to analytical solutions and literature solutions.
To determine whether a singular solution can be found, the convergence of the program is tested. The test is performed for a structurally stiff 24 meter sided cube, that has a draught of 12 meters. The panel size is varied between the values of 12, 6, 3 and 2 meters, and results for the added mass, hydrodynamic damping, stiffness and exciting force vector are compared. For this specific test the coefficient results belonging to each panel are added together to construct a singular 6 by 6 matrix. The convergence is tested for the frequency range starting at 0.025 radians per second, ending at 2 radians per second with a step size of 0.025 radians per second.

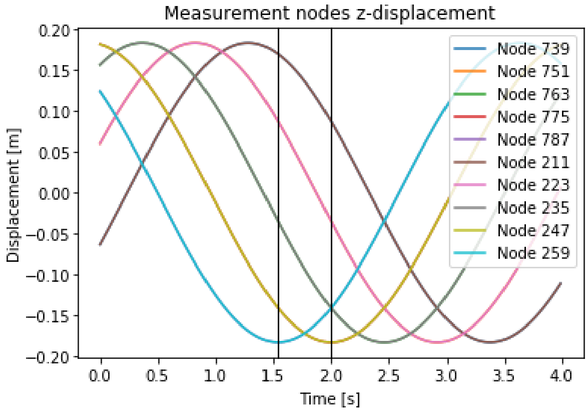

Figure 4.4: Phase difference test result. Time represented in seconds on the x-axis, displacement of the measurement nodes in meters on the y-axis.

The presentation of all the coefficients of added mass, hydrodynamic damping, and hydrostatic stiffness would require 108 plots, another 6 plots are required to represent the exciting wave force coefficients. The amount of plots are to many to be shown in the report. Therefore the convergence for the heave coefficients values for the added mass, damping and stiffness matrices and the exciting force coefficient are shown.

The expectation is that for decreasing panel size the solution will start to converge to a singular value for a given frequency in each of the plots. In Table 4.6 the values for the coefficients are shown for the earlier stated panel sizes.

From the convergence test the conclusion can be drawn that the method converges to a solution as the panel size used is decreased. The hydrostatic stiffness is independent of frequency and remains constant as expected. The heave component of the hydrodynamic damping quickly converges even at larger panel sizes. The heave component of the exciting wave force vector requires a panel size of around 3 before reaching a steady value, the same is true for the heave component of the added mass.

An interesting phenomena seems to occur at mostly higher wave frequencies where the value seems to suddenly jump between values (almost in the way a discontinuous function would). The expectation is that this occurs at irregular frequencies [46], and [22]. Orcina [46] states that this is an error caused by mathematical and computational technicalities, and that the affected frequency range can be made smaller by means of smaller panel sizes, but not eliminated.

To determine whether this is an irregular frequency or an error in the code, the equation for finding the first irregular frequency ($\hat{\omega}$) for simple geometries by Chen [5] is used, see Equation 4.9. This equation is simply a function of length (L), width (B), draught (T), and gravity (g).

$$\hat{\omega} \approx \sqrt{\frac{gk_{11}}{tanh(k_{11}T)}} \tag{4.9}$$

In which:

$$k_{11} = \sqrt{\frac{1}{L^2} + \frac{1}{B^2}} \tag{4.10}$$

Substituting the appropriate values for the modeled cube results in a first approximate occurrence of an irregular frequency at 1.36 radians per second. It is therefore highly likely that the peak found in the heave added mass coefficient plot is an irregular frequency.

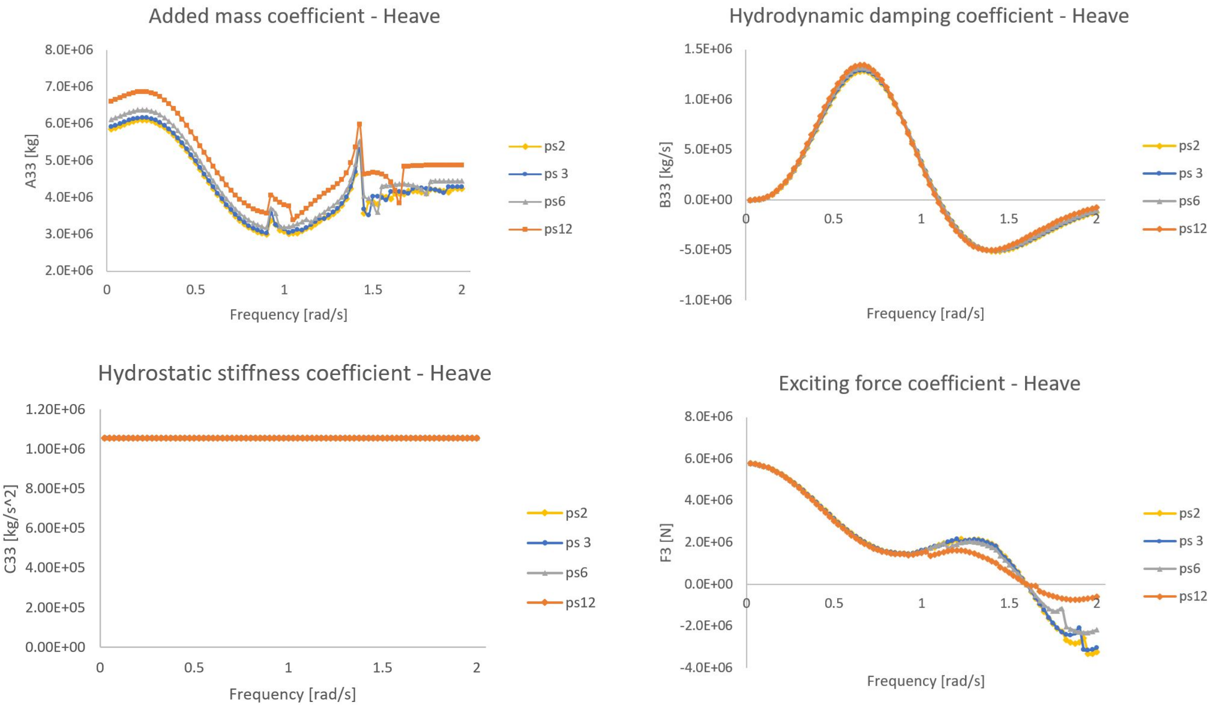

Table 4.6: Convergence test heave coefficients. Top left: convergence of the heave coefficient of the added mass. Top right: convergence of the heave coefficient for the hydrodynamic damping. Bottom left: convergence of the heave coefficient for the hydrostatic stiffness. Bottom right: convergence of the heave coefficient for the exciting wave force. Panel sizes denoted as ps in the units meter.

The influence of irregular frequencies can result in faulty coefficient values being introduces into the EOM. Multiple methods have been researched to remove the occurrence of irregular frequencies [5], but these will not be implemented in the thesis as this is not the primary focus. The occurrence of irregular frequencies in the applied exciting wave frequency range is therefore an aspect that must be checked during the validation.

A second smaller peak is found to be strange in the heave coefficient of the added mass at approximately 0.92 radians per second. A peak would suggest that the added mass for this frequency suddenly increases and then rapidly decreases again, resulting in a sudden increase and decrease of resistance against imposed acceleration. One likely reason is the existence of a natural heave frequency, as a wave at this frequency is likely to induce resonance in the structure.

To determine whether the natural heave frequency of the structure is causing this peak, Equation 4.11 is used, in which L is the length of the structure, B is the width of the structure, M is the mass of the structure and A33 is the heave coefficient of the added mass at this specific frequency.

$$\omega_{33} = 2\pi \sqrt{\frac{\rho g L B}{M + A33}} \tag{4.11}$$

Substituting the values for the structure and fluid, the resultant natural heave frequency is determined to be 8.4 radians per second, and is therefore determined not to be the cause of the peak. The nearest eigenfrequency of the dry structure, converted to wave frequency is 3.5 radians per second. The peak seems to become smaller with decreasing panel size. A further decrease in panel size was therefore attempted but this resulted in an out of memory error on the work computer.

A last cause may be that this is a spurious frequency. Spurious frequencies can occur when the wave length may cause resonance internally in the structure. The wavelength of the peaking frequency is calculated. This resulted in a value of 72.8 meters, roughly three times the length of the cube. A second

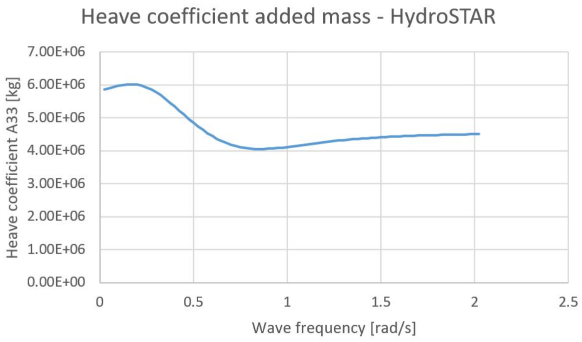

Figure 4.5: Added mass heave coefficient calculation by HydroSTAR. 24 meters sided cube, 12 meter submersion depth in infinite water depth, and panel size of 2 by 2 meters.

and third peak would then be expected at 1.13 and 1.60 radians per second. Which seems likely based on the added mass plot in the top left of Table 4.6.

To determine if the small peak is an error in the code. To examine this further the heave coefficient for the added mass of the 24 meter sided cube is determined via HydroSTAR with a panel size of 2 by 2 meters. This resulted in Figure 4.5.

From Figure 4.5 it is clear that no such bump is calculated by HydroSTAR. It is also clear that in the wave frequency range 0.75 up to 1.2 radians per second the added mass is estimated to be higher by HydroSTAR then by the numerical method developed. The reason for this is difficult to determine, as this would require diving into the calculations made internally in HydroSTAR which is not possible. For frequencies outside this range the results are comparable to those found by HydroStar.

5

Experiments

In this chapter the experiments used to validate the numerical method are presented, as the method is still in development the amount of presented results is limited. To validate the numerical method, the MARIN tank experiment measurements are compared to the results as found via the numerical method. The structure of this chapter is therefore as follows. First a description of the experiment setup and the measurement equipment is provided. Applicable test cases are then selected based on the applicable range of the numerical method. The capability of the numerical program to model the undisturbed tested waves is tested and results are presented. After the capability of modeling waves is validated. Test cases are chosen and results are presented. These results are discussed in chapter 6.

5.1. MARIN tank experiment

MARIN executed seakeeping tests for a 1:1 scale structure in regular waves in the depressurized wave basin. To validate the method described in this thesis, the characteristics of the experimental setup are used to define the inputs for the numerical model.

The basin

The basin is 240 meters long, 18 meters wide, and has a fixed water depth of 8 meters. In the basin both longitudinal as well as transverse waves can be simulated. The maximum wave height that can be simulated in the longitudinal direction is 0.75 meters at a 4 second wave period. The longitudinal generated waves end on a absorbing beach. For an impression of the basin see, Figure 5.1.

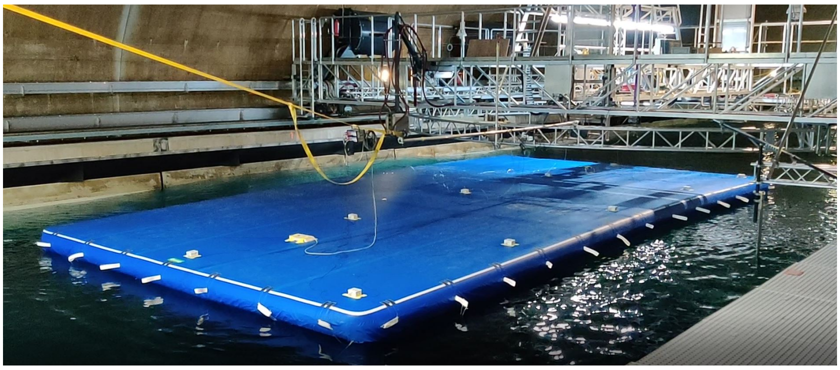

Figure 5.1: MARIN wave basin JIP structure test

Calibration

Before testing, the waves were calibrated at the moored position of the structure, without the structure present in the basin. Twenty-one regular waves were tested ranging from 1 to 4 seconds, without exceeding the wave breaking limit. The instrumentation allows up to 0.4 meters at a wave period of 3.0 seconds. An overview of the associated wave period and height of the measured waves is represented in Figure 5.2, in which the first numbers before the underscore in the labels stated in the legend refer to the testing sequence.

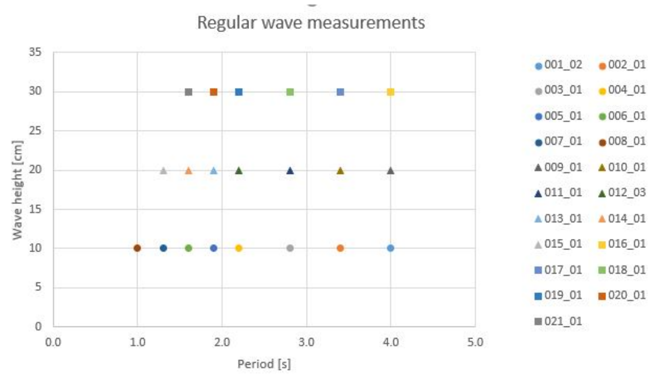

Figure 5.2: Overview of the MARIN measured waves. Wave period in seconds on the x-axis, and wave height in meters on the y-axis, the labels in the legend refer to the test sequence.

Instruments

The reference wave heights are measured by means of a resistance type wave probe. The translations and rotations are measured on one point of the model by means of an NDI contact-less optical position measurement system. The system determines model motions based on the three infrared LEDs on a position target placed on the center of the model (x,y = 0). The accelerations are measured at 10 positions by means of 3 DOF Piezo-type accelerometers. The sampling rate for the wave probe was 200 Hz. The digital optical systems measure at 100 Hz.

Setup

The structure is modeled with the values provided in Table 5.1.

Abbreviation	**Description**	**Value**	**Unit**
L	Length of the structure	15	$[m]$
B	Width of the structure	7	$[m]$
H	Top surface of the structure	-	$[m]$

Table 5.1: Characteristics of the model tested.

The motions of the structure are measured at multiple positions by means of accelerometers. An overview of the locations on the structure and the corresponding accelerometer names is provided in Figure 5.3, and the coordinates can be found in Table 5.2. In this table L denotes the length of the structure and H denotes the height of the structure.

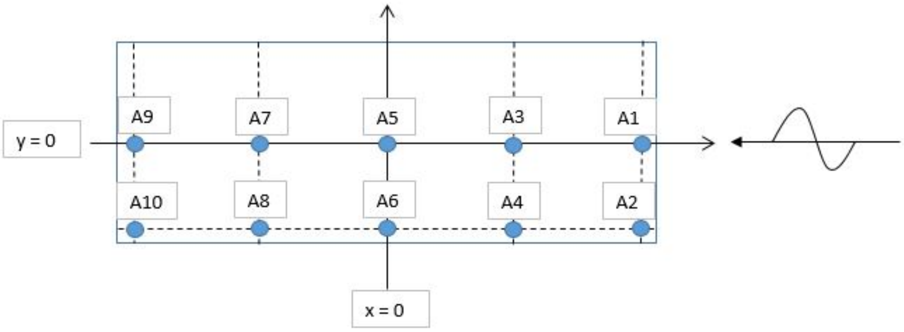

Figure 5.3: Location of the measurement points on the model given by the blue dots, accelerometer names provided by the label.

Accelerometer name	x-coordinate	y-coordinate	z-coordinate	unit
$A1$	0.46 L	0	H	$[m]$
$A2$	0.46 L	- 0.23 L	H	$[m]$
$A3$	0.23 L	0	H	$[m]$
$A4$	0.23 L	-0.23 L	H	$[m]$
$A5$	0	0	H	$[m]$
$A6$	0	-0.23 L	H	$[m]$
$A7$	-0.23 L	0	H	$[m]$
$A8$	-0.23 L	-0.23 L	H	$[m]$
$A9$	-0.46 L	0	H	$[m]$
$A10$	-0.46 L	-0.23 L	H	$[m]$

Table 5.2: Marin model test accelerometer measurement coordinates

5.2. Applicable test cases

To determine the amplitude at different positions of the body, the regular deep water wave equation was implemented in the numerical method. To ensure that the method can be compared to the data measured, i.e. considering the simplifications and assumptions made in the method, first the measured waves are analysed. The method is currently valid for deep water cases, i.e. cases in which the ratio of water depth versus wavelength is larger than 0.5 [-]. The measured wave ratios are plotted based on a water depth of 8 meters and their associated wave periods in Figure 5.4.

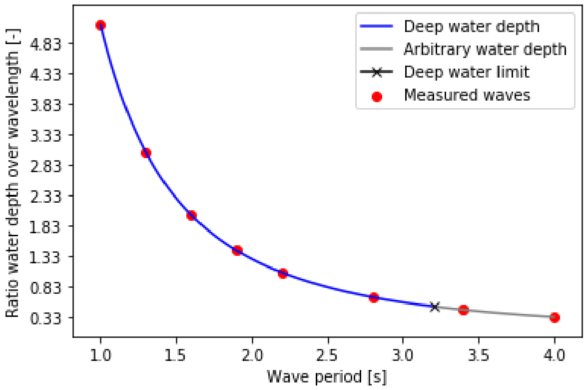

Figure 5.4: MARIN measured waves. The wave length in meters is provided on the x-axis, the ratio of water depth in meters over the wavelength in meters is provided on the y-axis

From Figure 5.4 it can be concluded that only the waves with a period of 3.4 and 4.0 seconds do not meet the requirements for deep water. The deep water simplification of $\omega^2 = gk$ is not valid and $\omega^2 = gktanh(kh)$ should be used. This intermediate water depth dispersion relation is not implemented in the method and these test cases should therefore be discarded.

5.3. Validation of the numerical wave

To verify that the regular deep wave equation has been implemented correctly, the numerical expression for the regular wave height is compared to a deep water wave measured by Marin. The properties of this undisturbed incident wave as provided by Marin are shown in Table 5.3.

Abbreviation	Description	Value	Unit
T	Wave period	2.8	$[s]$
ω	Wave frequency	2.24	$[\frac{rad}{s}]$
Amp	Wave amplitude	0.05	$[m]$

Table 5.3: Characteristics of the MARIN wave used in the validation of the numerical wave. Time in seconds on the x-axis, wave elevation in meters on the y-axis.

The wave generators require time to build up to the actual wave during a ramp-up period, the comparison is therefore executed after this period has finished. The comparison of the numerically simulated wave and the measured wave is provided in Figure 5.5.

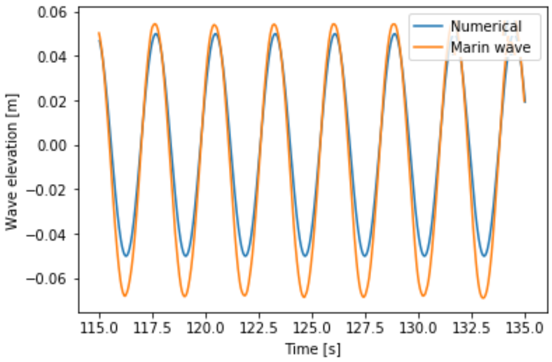

Figure 5.5: Numerical undisturbed deep water wave validation based on MARIN data. Time in seconds on the x-axis, wave elevation in meters on the y-axis.

The numerical wave does provide the correct frequency for the measured wave, but the amplitude as stated in Table 5.3 deviates relative to the actual measured wave by MARIN. Adjusting for the difference in average height by 0.015 meters and difference in amplitude 0.011 in the inputs for the numerical wave, results in Figure 5.6. This figure shows the both the adjusted numerical wave and the MARIN measured wave with wave elevation on the y-axis and time on the x-axis.

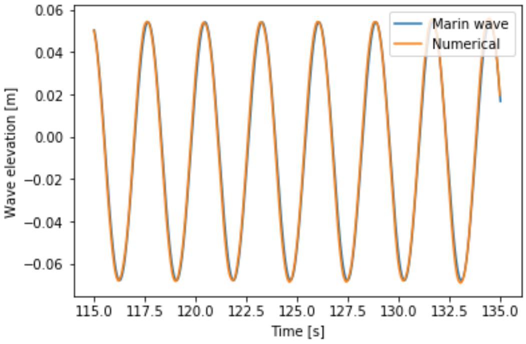

Figure 5.6: Numerical undisturbed deep water wave validation based on MARIN data after adjustments. Time in seconds on the x-axis, wave elevation in meters on the y-axis.

From Figure 5.6 it can be concluded that the numerical method is able to model the waves as generated and measured during the tests at MARIN by MARIN.

5.4. Test cases

As stated at the beginning of this chapter the method still in development, for this thesis some test cases are used to provide insight on the current capability of the program. Based on the calculation performed in section 5.2 and the results represented and reiterated in Figure 5.7, three incident wave frequencies are chosen with varying amplitudes as test cases for the numerical method. This should allow for an adequate amount of results to validate both the numerical models reaction to differing wave frequencies as well as amplitudes. An overview of the wave characteristics of the considered test cases is provided in Table 5.4. Argumentation for the choice of the test cases is provided below.

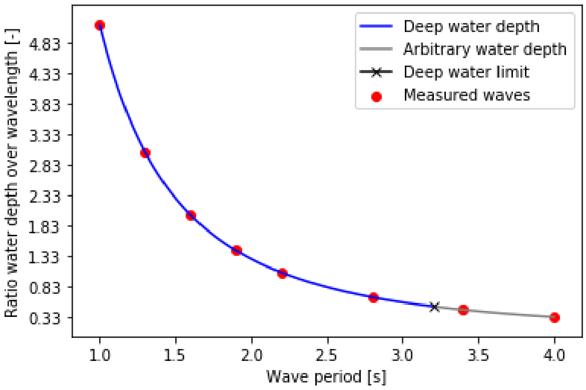

Figure 5.7: MARIN measured waves. The wave length in meters is provided on the x-axis, the ratio of water depth in meters over the wavelength in meters is provided on the y-axis

Abbreviation	**Description**	**Value**	**Unit**
T_1	Incident wave period	4.0	$[s]$
T_2	Incident wave period	2.8	$[s]$
T_3	Incident wave period	2.2	$[s]$
$ampl_1$	Wave amplitude	0.10	$[m]$
$ampl_2$	Wave amplitude	0.15	$[m]$

Table 5.4: Test cases wave amplitude and frequency

The first test case (T_1) consists of an incident wave with a wave period of 4 seconds and a wave amplitude of 10 centimeters. This wave is considered interesting as the wave length exceeds the length of the structure, and the wave length is close to a multiple of the structure length. Based on the theory presented in chapter 2 the global response is expected to be dominant. The expectation is therefore the structure may exhibit interesting behavior in terms of global motions. This test case would therefore show the capability of the numerical method to model the global deformation motions of the structure.

The second test case (T_2) consists of an incident wave with a period of 2.8 seconds and a wave amplitude of 0.15 meters. The wave is the first tested case for which the wave is shorter than the structure length. In chapter 2, it was described that at a wavelength shorter than the structure length local deformations would play a more significant role. The expectation is that this is the first tested wave for which the associated phenomena will be visible. Hoof [66] provides insight on some of the hydroelastic effects which may occur. In the case of adequate draft wave shortening is to be expected. If the structure is stiff enough it can result in wave lengthening. These effects should be more pronounced for measurement locations near the center of the structure.

The final test case (T_3) consists of a wave 2.2 seconds and an amplitude of 0.10 meters. The wave is selected it is roughly twice as short as the modelled structure. The hydroelastic interactions as mentioned for test case 2 are expected to be the even larger for this test case. The hydroelastic effects should be most noticeable near the center of the structure and smaller to the sides of the structure. The expectation is that the deformation on the corner measurement points can be modelled relatively accurately, with less accurate results for the points closer to the center of the structure. The errors are expected to be larger than those found for test case 1 and 2, due to the increased expected hydroelastic interactions which are not implemented in the method.

5.5. Hydroelastic tests

In this section the results are provided as calculated with the numerical method and as measured by MARIN for the Joint Industry Project. The results have been normalized. The measurement locations chosen are located near the longitudinal edge of the structure, as the goal is to determine whether the motion of the fairlead point locations can be modelled accurately. The measurement locations are therefore A2, A4, A6, A8, and A10 as provided in Figure 5.3 & Table 4.4, are now renamed by adding a Z to represent heave measurement.

The results of each of the individual tests will be presented as follows. First figures are provided showing both the MARIN test results and the numerically determined test results. Then individual figures are provided for each considered test location. As these previously mentioned figures only provide a quick overview, the error in maximum displacement value between the numerical approach and the MARIN values is presented. The percentage error (ϵ) between the maximum amplitude found by MARIN (z_m) and numerical (z_n), is determined via Equation 5.1 and provided in a table.

$$\epsilon = \frac{z_n - z_m}{z_m} * 100 \tag{5.1}$$

As previously stated, the MARIN measurement data experiences a delay before a regular wave profile is formed due to the ramp-up time of the wave generator. The time required is different for each wave test, which explains the different time axis in the resultant comparison plots.

5.5.1. Test case 1: Incident wave longer than the structure

The results as calculated for a wave amplitude of 10 centimeters and a wave period of 4 seconds are presented in Figure 5.8. The first subplot shows the combined results for all the measurement locations for both the MARIN and the numerical model. The percentage error (ϵ) between the maximum amplitude found by MARIN (z_m) and numerical (z_n) for each of the measurement locations is provided in Table 5.5.

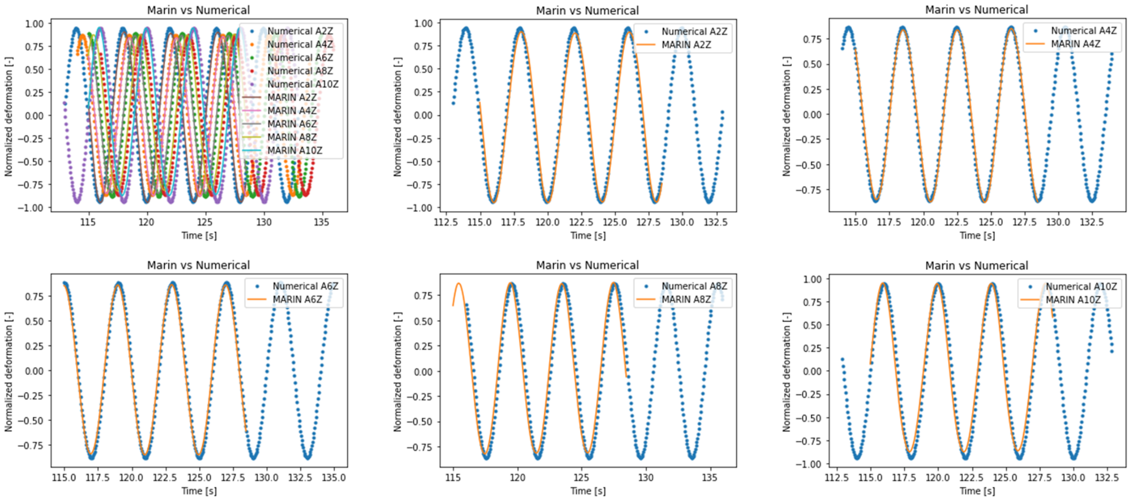

Figure 5.8: Numerical and MARIN results for 4 second wave period. Time is plotted on the x-axes in seconds, normalized displacement on the y-axes.

Locations	Error	Unit
A2Z	4.57	[%]
A4Z	1.79	[%]
A6Z	2.37	[%]
A8Z	-1.20	[%]
A10	-0.68	[%]

Table 5.5: Maximal displacement error for the numerical method compared to MARIN experiments

From the first plot of Figure 5.8 a clear distinction in structural response between nodes can be seen. Measurement locations $A2Z$ and $A10Z$ move in anti-phase. The measurement locations near the corner of the structure display larger responses, see measurement locations $A2Z$ and $A10Z$. Measurement locations $A2Z$ and $A8Z$ have a slightly lower response to the incident wave than $A6Z$. No phase difference or significant unsymmetrical deviation in amplitude between measurement locations can be seen.

The calculated errors in Table 5.5, describing the difference in maximum displacement for the numerical method with respect to the MARIN test, are in the range of -1.2 to 4.57 percent.

5.5.2. Test case 2: Incident wave length slightly smaller than the structure

The results as calculated for a wave amplitude of 15 centimeters and a wave period of 2.8 seconds are presented in Figure 5.9. The first subplot shows the combined results for all the measurement locations for both the MARIN and the numerical model. The percentage error (ϵ) for the measurement locations in this test is provided in Table 5.6.

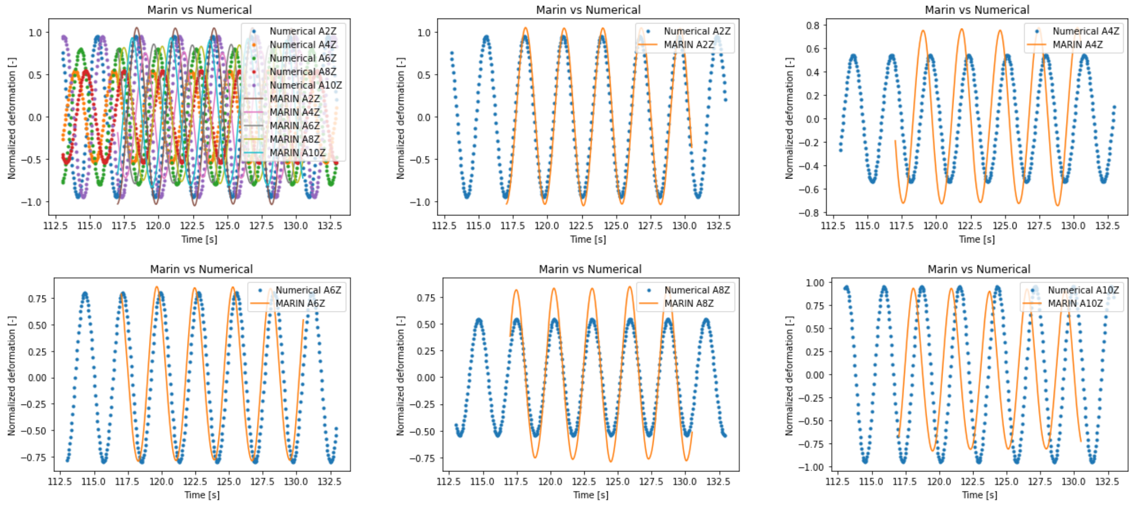

Figure 5.9: Numerical and MARIN results for 2.8 second wave period. Time is plotted on the x-axes in seconds, normalized displacement on the y-axes.

Locations	Error	Unit
A2Z	-9.85	[%]
A4Z	-29.89	[%]
A6Z	-6.77	[%]
A8Z	-36.01	[%]
A10Z	1.93	[%]

Table 5.6: Maximal displacement error for the numerical method compared to MARIN experiments

Top right figure in Figure 5.9 shows that locations $A2Z$ and $A10Z$, and $A4Z$ and $A8Z$ move in a similar manner with respect to maximum and minimum amplitude. The figure for $A4Z$ plot shows a large deviation between the numerically calculated deformation and the experimental deformation in terms of amplitude as well as a phase difference. According to the numerical model the structural response should be significantly lower. The deformation of this point in the MARIN test occurs earlier than calculated with the dispersion relation in the numerical method. This effect also appears for the middle point $A6Z$, but the phase difference is less. Measurement location $A6Z$ on the center of the structure shows a slight difference in deformation and a phase difference. $A8Z$ again shows the same large deformation behavior as found for $A4Z$, however no phase difference is found. The plot for $A10Z$ shows a phase difference between the numerical model and the experiment. $A10Z$ also shows that the minimum experimental deformation for $A10Z$ is lower than calculated by the numerical method.

In Table 5.6 the calculated errors are provided for each of the measurement points. Measurement locations $A2Z$, $A6Z$ and $A10Z$ remain within a range of -9.85 to 1.93 percent. $A4Z$ and $A8Z$ have large errors of -29.89 and 36.01 percent.

5.5.3. Test case 3: Incident wave significantly smaller than the structure

The results as calculated for a wave amplitude of 15 centimeters and a wave period of 2.2 seconds are presented in Figure 5.10. The first subplot shows the combined results for all the measurement locations for both the MARIN and the numerical model, the other subplots show the results for the individual measurement points.

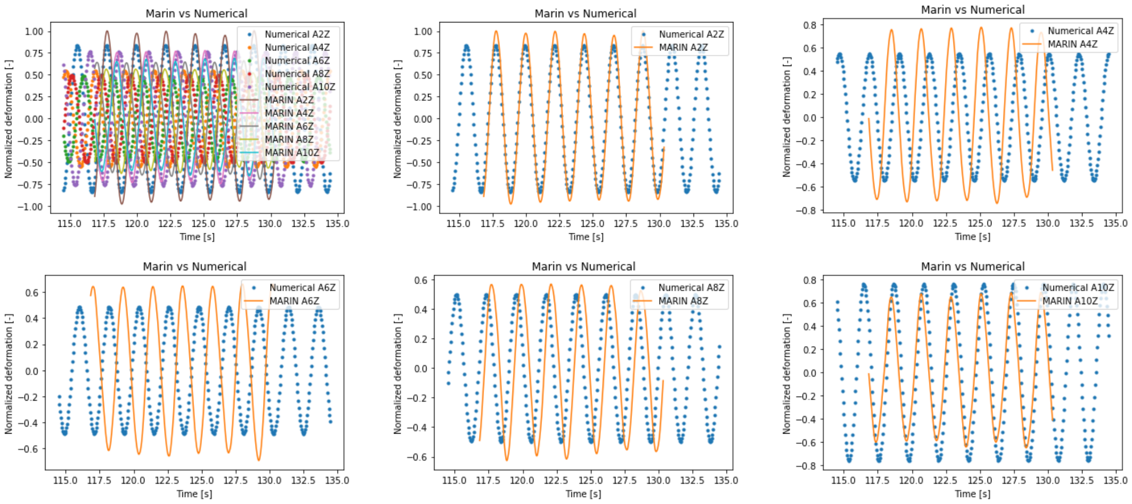

Figure 5.10: Numerical and MARIN results for 2.2 second wave period. Time is plotted on the x-axes in seconds, normalized displacement on the y-axes.

Locations	Error	Unit
A2Z	-16.36	[%]
A4Z	-29.58	[%]
A6Z	-26.42	[%]
A8Z	-12.24	[%]
A10Z	10.53	[%]

Table 5.7: Maximal displacement error for the numerical method compared to MARIN experiments

The top left figure in Figure 5.10 is too chaotic to provide meaningful observations. For each of the measurement locations presented in the following sub figures the numerical method underestimates the deformation of the structure except for $A10Z$. This difference between the MARIN measured deformation and modeled deformation becomes increasingly worse from measurement points $A2Z$ to $A6Z$, and improves for measurement point $A8Z$. The differences between the model and the MARIN experiments is largest for $A4Z$ and $A6Z$. This is represented by the error values presented in Table 5.7. Noticable phase differences are found for measurement points $A4Z$, $A6Z$ and $A8Z$. A slight difference in phase can also be seen for $A10Z$.

To provide a secondary view on the deformation behavior of the measurement locations, the results for all waves as measured by MARIN are provided in Figure 5.11. From this figure it is noticeable that the deformation first drops after measurement point $A2Z$ and then steadily rises as the wave progresses, with a slight relapse at $A8Z$.

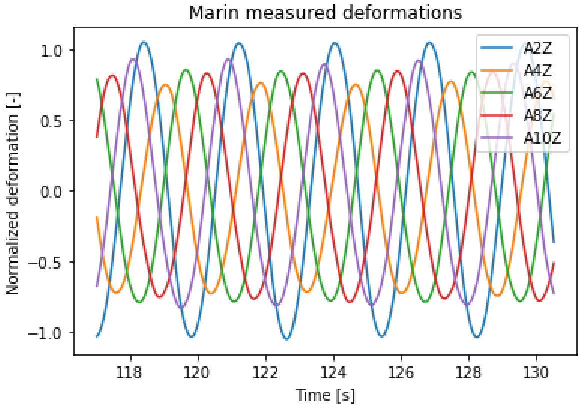

Figure 5.11: Deformation at measurement points as measured by MARIN for a wave period of 2.2 seconds and wave amplitude of 15 centimeters. Time represented in seconds on the x-axis, and normalized deformation on the y-axis.

6

Discussion

In this chapter the results of the test cases as presented in section 5.4 are discussed. First the results are discussed individually per test case. Then the combined observations and trends are discussed. Implications of the found results and current shortcomings of the numerical method are then provided.

6.1. Test case 1

From the sub figures shown in Figure 5.8 it can be seen that the displacement of the measurement points as calculated by the numerical model and as measured by MARIN show good agreement. The largest error in maximum amplitude is 4.57 percent. The hypothesized interesting behavior for this wave period has been found and is represented as an anti-phase deformation of the $A2Z$ and $A10Z$ measurement locations. No local hydroelastic effects have been found in the form of wave lengthening or shortening, or as deviations in expected deformations. The structure can be characterized to have responses in which the global behavior is dominant.

The anti-phase motion of the structure may be explained by the wave characteristics. A wave period of 4 seconds correlates to an undisturbed wavelength of 25 meters. When considering the structure deformation measurements at for instance 120 seconds, the most leading measurement point $A2Z$ and $A10Z$ are exactly located on the through and crest of the wave. This is represented in Figure 6.1.

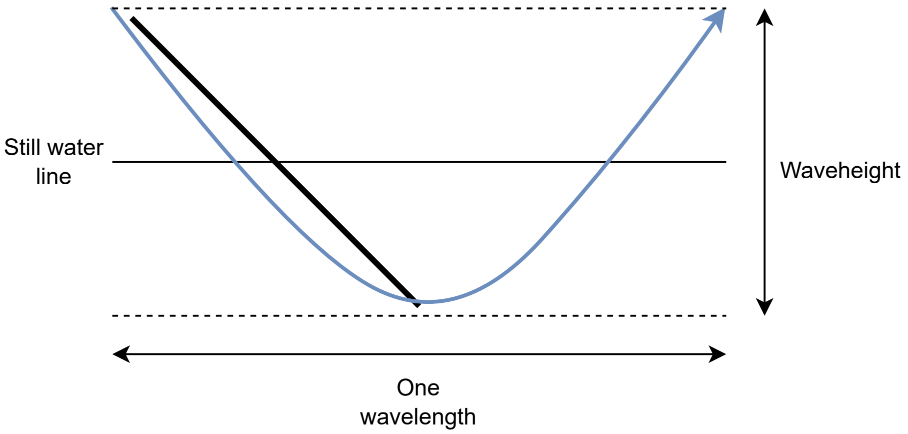

Figure 6.1: Explanation of the anti-phase of measurement locations. In blue the traveling wave, and the diagonal black line represents the structure.

6.2. Test case 2

In test case 2, two possible cases of effects of hydroelasticity on the structure are found. The first is the phase difference, the second is the increase in amplitude. Although it is enticing to immediately point to hydroelasticity it is necessary to consider other options, these are as follows. The structure can move in an excitable eigenmode if the wave has specific lengths, resulting in large deformations. The structural stiffness is actually lower than as used in the numerical method, resulting in larger deformations. The mass of the structure is underestimated which may result in larger deformations. These possible reasons are discussed below.

The exciting wave has a wave length of 12.2 meters. The distance between measurement locations is 3 meters, it is therefore possible that both $A4Z$ and $A8Z$ lie in the crest or through respectively. Which could represent itself as the third excitation mode of a beam. It would however then also be expected that the movement of the center point could become large. The measurement locations $A2Z$ and $A10Z$ would still have relatively low deformations due to the additional local weight of the ballast bags. The mode explanation is therefore not the likely reason.

If the structural stiffness of the structure would be lower for points closer to the center of the structure, it would be expected that the center point would experience increased deformations as well. In this case the stiffness at the center of the structure would therefore have to be higher. This theory is therefore also not likely, because it would mean that the structural stiffness changes drastically in 6 meters.

In the numerical method the assumption is made that the mass of the water in the ballast bags can be neglected as this mass is underwater most of the time. This mass is located at the edges of the structure resulting in less deformation at the edges and larger deformation near the center of the structure. Once again it would be expected that the center point $A6Z$ would move in a similar manner as $A4Z$ and $A8Z$. The mass is therefore not likely to be the contributing factor.

This results in the discussion of possible hydroelastic effects, and the option that they are the cause. The phase difference is visible in a peculiar way. The outer measurement point $A2Z$ is hardly affected, whilst the effect is greatest for $A4Z$, $A6Z$, and $A10Z$. The effect disappears completely for $A8Z$. A possible explanation would be the impact of the draught of the non-modelled ballast bags.

Van Hoof [66] states that the draught of a structure can result in wavelength shortening when the draught of the structure dominates over the stiffness of the structure. Wave shortening would therefore express itself as a deformation that occurs earlier at a measurement point than expected. For measurement points $A4Z$ and $A6Z$ this could explain why the phase difference becomes less pronounced when the distance from the ballast bag increases. The wave length at these positions can grow due to an the increased domination of stiffness over draught.

Wave shortening is stated by Van Hoof to lead to wave focusing, and therefore increased amplitudes. This could explain why the amplitudes can be significantly higher at locations where draught is likely to dominate over the structural stiffness. It is however not possible from the test data to determine whether this is the case, as the wave elevation was measured at a single point.

6.3. Test case 3

In test case 3 similar effects are found as for test case 2. The expectation was that for increased wave frequency the impact of hydroelastic interaction with the structure would become larger. Test case three was therefore expected to have the largest errors. This proved to be correct as the deviation from the MARIN experiment is noticeable for all measurement points.

From the comparison between the numerical model and the MARIN data it is indirectly visible that the wave is deformed under the structure. The phase difference between the numerical model and MARIN data is largest for $A4Z$ and $A6Z$. The wave arrives earlier at these points than expected by the numerical model. This might again be explained by the wave shortening due to the effect of the draught of the structures ballast bags. This phase difference seems to be reducing for measurement points $A8Z$ and $A10Z$.

The drop in deformation as found for $A4Z$ and $A6Z$ with respect to $A2Z$ is likely due to the influence of the ballast bags as previously discussed in test case 2. The error as found for $A8Z$ is smaller than found in test case 2 and may be attributed to the fact that the ballast bags deformed backwards and upwards due to the pressure of the wave. This would reduce the impact of the draught and could result in lower amplitudes if the structure in this region becomes more stiffness dominated than draught dominated.

6.4. Combined observations and trends

For waves longer than the structure the deformation is dominated by the global response and no hydroelastic effects were found. These deformations can be described fairly accurately. For a wave shorter than the structure, the deformation of points seems highly dependent on whether the draught or stiffness is dominant for that location. Due to the way the test was set up no definitive conclusions can be drawn on the cause of the associated deviations.

6.5. Implications and shortcomings

It has been found that for waves shorter than the structure the deformation is impacted by hydroelastic effects as expected. These hydroelastic effects increase for increasing wave frequency. These effects are not captured by the numerical model as the impact of the draught of the ballast bags was neglected based on the structural characteristics and nonlinear behaviour of the structure.

Van Hoof [66] states that “for the application of offshore floating solar, the wave deformation is negligible as most sea-states consist of waves with frequencies lower than the domain were significant wave deformation occurs.”. For inland application of floating solar the effect can be considerable.

Consideration of the ballast bags is therefore likely required to allow for a better approximation of the structure deformation in shorter than structure waves.

7

Conclusions

In this thesis a new numerical method for the determination of the motions of a flexible structure and its interaction to a mooring line system in OrcaFlex was presented. The work in this thesis focuses on the fluid-structure interaction part of the method, but considers the coupling with OrcaFlex in the design. The method presented therefore serves as a basis for the further development of a full program capable of describing both the hydroelastic behavior of the structure as well as the interaction with a dynamic mooring line model in OrcaFlex.

The work executed in this thesis can be summarized as follows. A method has been constructed which is capable of determining the structural matrices and generating a mesh by means of ANSYS. The mesh is directly coupled to the fluid by converting the ANSYS mesh to a boundary element mesh. This boundary element mesh is used in solving the radiation-diffraction problem by means of a lower order panel method based on the work by Katz and Plotkin, Telste and Noblesse, Guha, Hess and Smith, and Viswanathan et al.. A Python script was written that constructs full structural matrix files from a sparse Harwell-Boeing format. These matrices are then used to assemble the fluid-structure equation of motion on a nodal basis.

The individual components for the equation of motion were successfully verified by comparison with analytical calculations, results from literature, and results from external software. The capability of the program to model undisturbed waves was validated and test cases were ran. It was determined that for waves longer than the structure the deformation of the fairlead points and flexible motion of the structure could be assessed accurately. The results for increasingly shorter wave length became less accurate. The deformation of the structure for short waves was likely impacted by significant hydroelastic effects due to the ballast bags and stiffness of the structure. These hydroelastic effects resulted in both phase differences, wave lengthening and shortening, and increased and decreased wave amplitudes. Due to the test setup it could not be confirmed that the hydroelastic effects are the main cause, but it is deemed very likely.

As the numerical method currently only considers the flat plate without the ballast bags, the influence of the draught of the ballast bags was not accounted for. The implementation of ballast bags may therefore result in a better approximation of the deformation of the structure for the shorter than structure waves.

The goal of the thesis was the development of a numerical method that is able to determine the motions of a flexible structure. The developed method is currently not able to fully describe the hydroelastic interaction of the JIP structure for waves shorter than the structure. These short waves are mostly relevant for inland water bodies. The method is considered suitable for long wave cases at sea. The hope is therefore that the method can be improved and serve as the basis for further development of the overall suggested program as represented in this thesis.

8

Recommendations

In this chapter recommendations for future research are given, that could add or improve the functionality of the numerical method developed in this thesis. These recommendations are based on a retrospective view on the work described and questions that arose that could not be answered within the scope of this thesis. The recommendations are limited to the fluid-structure model as verified and validated in the thesis, and are given in the order of most to least important.

The hydroelastic interaction of the structure and wave was determined to be important for waves shorter than the structure. The influence of the ballast bags was not considered in the scope of the thesis due to the nonlinear behavior, but likely contributes strongly to the deformations found for short waves. It is therefore recommended to execute a study on the effect of the ballast bags on the hydroelastic motions of the structure. This could result in better approximations for structure deformation for shorter than structure waves.

The numerical method has been set up in such a way that the mesh is provided by ANSYS based on the SOLID 186 element type. This choice was made early in the process and has resulted in a meshing operation which can be considered computationally expensive for fine grid models. The implementation of shell elements could reduce both the computational time and reduce the storage space required. Research into the application of shell elements is therefore recommended.

In this thesis a deep water linear potential solver was used for the determination of fluid matrices and the wave exciting force vector. During verification calculations it became clear that the speed of this implementation was significantly slower than that of HydroSTAR. It is therefore recommended to look into the feasibility of nodal calculations in for instance HydroSTAR to improve the efficiency of the program. This would also allow for shallow and arbitrary water depth calculations.

Another recommendation for the improvement of efficiency of the current method lies in the implementation of code that allows the usage of multiple Computational Processing Units (CPU) in Python. Currently the method is restricted to one CPU due to the Global Interpreter Lock (GIL). The implementation of code that allows the usage of multiple CPUs in Python is not difficult, but can result in a significant increase in computational efficiency.

Finally, the code as currently used in the thesis is not considered user friendly for the following reasons. The user has to input the required values directly in the Python scripts. The ANSYS and Python related processes are considered in separate scripts, and comparing the numerical data and MARIN data requires an additional script. In most cases only a short description is provided on the actions executed in the script. It is therefore recommended to streamline the user experience by the implementation of a relatively simple user interface. The second recommendation would be to clean up comments, improve the code, and to provide better function descriptions. This results in better code, which is useful for further expansion of the method.

A

Program summary

The code written to implement the extensively described method in the thesis is considered proprietary. It is therefore not enough to describe the method, but also details on how tests were executed, which software versions were used and the capabilities of the executing system is required.

A broad description of the method has been provided in the main body of the report, along with descriptions of how the numerical tests were set up and performed. In this appendix details regarding both the program and test computer are provided.

A.1. Program and computer details

Program title: WaveRider
Licensing provisions: Proprietary code
Number of lines in program:

- AnsysCaller: 219
- Transcription: 79
- FSI: 3295
- Telste and Noblesse executable: 636

Number of bytes in program:

- AnsysCaller: 8 kb
- Transcription: 4 kb
- FSI: 181 kb
- Telste and Noblesse executable: 2.213 kB

Distribution format: Digital version internal system Bluewater Energy Services bv..
Programming language: Python 3 & Ansys APDL.
Testing computer:

- Processor: Intel(R) Core(TM) I7-7700HQ CPU @2.80GHz 2.81 GHz
- RAM-Memory: 8.00 GB (7.88 GB available)
- Windows operating system version: 64-bit
- Windows edition: Windows 10 home

Anaconda version: version 3.5.2 64-bit
Operating system: Windows 10, 64-bit
Nature of the problem: Frequency domain Fluid-Structure interaction solver for regular deep water waves.
Potential application fields: Design of offshore or near-shore floating flexible structures.
Running time: Dependent on input parameters and operating system.

B

Tutorial

In this appendix a step by step description description of how to use the method presented in the thesis is described. First the required actions to allow for the running of the script will be detailed. Then the direct user interaction will be described.

B.1. Setup

In this section the required steps to use the method are provided, these are listed below.

- Installing Python and accompanying packages.
- If on a proprietary computer, attaining the proper access rights to execute both the script and the executable.
- Installing the ANSYS interaction connection.

B.1.1. Installing Python and accompanying packages

To run the scripts developed for the exectution of the described method it is required to install both Python and the packages used in the script. This is easily done by going to the following website: “https://anaconda.org/””, downloading the files and installing it according to the provided instructions. For the installation it is required to have a 64 bit version of Anaconda as the Telste and Noblesse executable used in the code is made for a 64 bit operating system.

B.1.2. Commercial computers and access rights

During the thesis the work was executed both on a personal computer as well as a commercial computer. Usually the access rights on commercial computers are restricted, self-made or installed executables are not allowed, and access to specific folders is withheld. The method as documented, requires two types of rights. Firstly, writing privileges to the working folder in which the Python script is located. Secondly, the right to execute the Telste and Nobless executable. This permission can usually be requested from and given by the IT department.

If the method is installed on a personal computer, the rights above are also required. But if the computer is ran in administrator (admin) mode, no issues should occur.

B.1.3. ANSYS interaction connection

This connection is attained by a Python module constructed by Bluewater. The Burro file, which contains the module script, is added to the working folder and is called when the ANSYS script is ran. This module is not required as the individual APDL codes given in the script can be used in the graphical user interface of ANSYS Mechanical APDL.

B.2. Direct interaction

To use the method, inputs are required in multiple scripts. These inputs will be described in three parts, and help in the following actions.

1. Create the necessary input files for the structural and hydrostatic & dynamic analysis.
2. Provide the inputs that determine the actions taken by the fluid-structure interaction analysis.
3. Post-processing of results.

B.2.1. Part 1: ANSYS structure modeling

In the current version of the method the structural shapes accepted are blocks and cubes. The material behavior is set to be isometric. The user is presented with the input fields in the Python script $"AnsysCaller.py"$ as presented in Table B.1.

Abbreviation	Description	units
L	length	$[m]$
B	width	$[m]$
H	height	$[m]$
ele	element length	$[m]$
rho	structural density	$[\frac{kg}{m^3}]$
EX	youngs modulus	$[\frac{N}{m^2}]$
modes	number of modes	$[-]$

Table B.1: AnsysCaller input fields

To provide insight in the axes system and representation of these inputs, see Figure B.1. The length is always provided in the x-direction, the width on the y-axis, and the height on the z-axis.

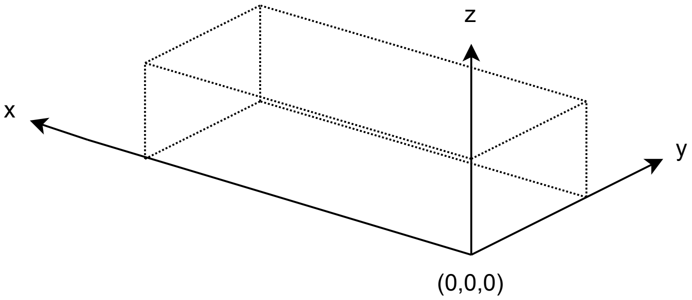

Figure B.1: Structure and axis system definition

The axes system used in the $"AnsysCaller.py"$ script is consistent with the rest of the method, except that the origin of the structure is shifted later on. This will be explained in part two.

Important note!: It is highly recommended that before running the script via the 'run file' or F5 button on the keyboard, previous ANSYS output files are deleted.
The acceptable input value ranges for each parameter in Table B.1 are presented in Table B.2.

In general, for each of the mentioned values a value larger than zero is acceptable. For the element length a value between zero and the smallest dimension should be considered. Once all values are filled in, the script can be run when an ANSYS licence is available.

The run-time of the script is dependent on the input values supplied, the general rule is more elements and/or considered modes result in a longer wait time. To determine whether the code is still busy two options are available. The first, checking whether all new files have been created in the working folder.

Abbreviation	Definition	Lower limit	Upper limit	Unit
L	Length	1e-10	∞	$[m]$
B	Width	1e-10	∞	$[m]$
H	Height	1e-10	∞	$[m]$
ele	Element length	1e-10	$min[L, B, H]$	$[m]$
rho	Structural density	1e-10	∞	$[\frac{kg}{m^3}]$
EX	Youngs modulus	1e-10	∞	$[\frac{N}{m^2}]$
$modes$	number of modes	1	∞	[-]

Table B.2: Valid input ranges

Secondly, by checking the IPython console for the end message provided by Python as shown in Figure B.2. The exact message differs depending on working folder location.

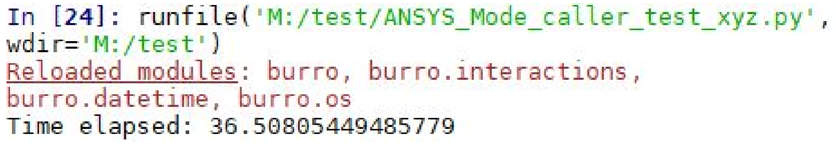

```
In [24]: runfile('M:/test/ANSYS_Mode_caller_test_xyz.py',
wdir='M:/test')
Reloaded modules: burro, burro.interactions,
burro.datetime, burro.os
Time elapsed: 36.50805449485779
```

Figure B.2: ANSYS is finished end message

B.2.2. Part 2: Fluid-structure-interaction

Now that the input files required for the hydroelastic analysis are constructed via the steps described in part 1 the next part of the analysis can be started.

The first required script for this part is named ”$TBD.py$”, the second required file is the Telste and Noblesse script aptly named ”$TelsteNoblesse\_fileIO.exe$”. Both of these files have to be located in the same file location as the files created in part 1.

The user now has to provide input values for the script, Table B.3.

Abbreviation	**Definition**	**Lower limit**	**Upper limit**	**Unit**
wav_dir	Incident wave direction	$-\infty$	$+\infty$	$[deg]$
$ampl$	wave amplitude	-∞	$+\infty$	$[m]$

Table B.3: Part 2: input values

The user also has to restate the length, width and height for the structure as used in part 1. A physical representation of the inputs is provided in Figure B.3. A clarification of input values are provided below which cannot be presented in the form of a figure.

- start_freq: Determines the initial wave frequency considered in the hydrodynamic analysis in radians per second.
- step_size: step size that determines which frequencies to consider between the start and end frequency in radians per second.
- end_freq: frequency after the last accounted for frequency in radians per second.
- Omega_requested: the frequency for of the harmonic wave considered in radians per second.
- time: first entry is the starting time for the simulation, the second the end time, and the third the step size between the start- and end time. All have the unit seconds.

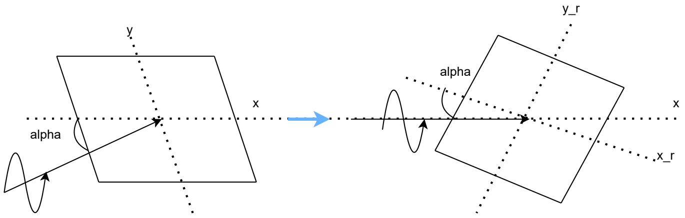

Figure B.3: Explanation of the incident wave direction (alpha) and wave amplitude (Sinusoidal vector)

B.2.3. Part 3: Post-processing commands

To determine whether the simulation has finished look for a similar message as provided in Figure B.2 in the IPython console.

In the FSI code, certain plots are always provided, while others depend on whether the user requests them in the input. Certain other plots can be made by typing the following command in the IPython console window.

The user can request a plot for the range of frequencies and all coefficients for the added mass and hydrodynamic damping, it also allows for the request of the wave excitation force values in the degree of freedoms provided. The command used to call a specific plot is explained below.

The user can request a plot by typing "$plot\_matrices(x, y, z, i)$" in the IPython console. In this expression parameter x describes whether the added mass (x = 0), hydrodynamic damping (x = 1) or the exciting wave force (x = 2) is requested. If the user wishes to plot matrix coefficients the y and z parameters state which row and column in the matrix is requested. For example: $plot\_matrices(0, 2, 2, i)$ will provide the added mass heave coefficient A33. When for instance the heave exciting force coefficient is requested the command $plot\_matrices(2, x, y, 2)$ is used. Note all counting starts at 0.

After completing the command and pressing the $enter$ button on the keyboard, the plot is constructed and shown in the IPython console.

C

Python script Harwell-Boeing

During the thesis a gap in available methods to transcribe a Harwell-Boeing files into a useable Python format was found. This was still required for the transcription of matrix files, combined with mapping files.

To provide others who might require a code to transcribe the HB files, without revealing the proprietary FSI code from the thesis. The Python code used to transcribe Harwell-Boeing format files to full matrices is provided in this appendix.

This code works for symmetric, sparse, and non-RHS matrix type files. The only input requirements are as follows:

- A .mat file created by Ansys via the HBMAT command.
- The file component of the hb_read function, defines the location of the matrix file.
- Optional: the user can provide the location of the mapping files in the second input for the hb_read input arguments.

Example code of how to use the function is provided at the end of the code.

Disclaimer: This software is provided by the copyright holder and contributors ”as is” and any express or implied warranties, including, but not limited to, the implied warranties or merchantability and fitness for a particular purpose are disclaimed. In no event shall the copyright owner or contributors be liable for any direct, indirect, incidental, special, exemplary, or consequential damages (including, but not limited to, procurement of substitute goods or services; loss of use, data, or profits; or business interruption). However caused and on any theory of liability, whether in contract, strict liability, or tort (including negligence or otherwise). Arising in any way out of the use of this software, even if advised of the possibility of such damage.

C.1. hb_read

Below follows the verbatim code.

```
    @author: T.A.Beinema
″″″

import numpy as np
import pandas as pd
from pathlib import Path

def hb_read(file, mapping=None) -> np.array:
    ″″″Read the output as generated by apdl command HBMAT.
```

```
    Mapping is also available

    file (path-like): Harwell-Boeiing formatted file
    mapping (path-like): Standard ANSYS mapping format, .mapping file
    ”””

    # Text file operations
    current_matrix_file = open(file,”r”)#”K.txt”,”r”)
    content = current_matrix_file.read()
    content = content.replace(”D”,”E”)

    # Constructing input
    #1) split into useable strings
    #2) Line 2: total, pointers,indices,matrix values, rhs info
    #3) Line 3: matrix type, number of rows, number of columns,
   #  NN-zero (for assembled = number of zero values), NELTVL (for assembled = 0)
    content_list = content.splitlines()
    line2 = content_list[1].split()
    n_pointers = int(line2[1])
    n_indices = int(line2[2])
    line3 = content_list[2].split()
    n_matrix_rows = int(line3[1])

    # State whether the format of the matrix supplied by ANSYS
    if line3[0] == ”RSA”:
        print(”Matrix in file is Real-valued, Symmetric, and Assembled”)
        symmetric = ’yes’
    else:
        print(”Matrix in file does not contain a RSA matrix”)


    # Matrix Assembly
    #1) Determine important positions based on the read .txt file
    #2) Use positions to determine the diagonals
    #3) Use positions and diagonals to determine the off-diagonals

    if symmetric in ”yes”:
        matrix = np.zeros((n_matrix_rows,n_matrix_rows))
        Diagonal_start = 4

        index_start = 5 + n_pointers -1
        index_end = index_start+ n_indices -1
        values_start = index_end + 1

      #Part that determines the correct diagonal values and writes them to the matrix
        count = 0
        for i in range(index_start,index_end+1):
           if i == int(content_list[count+Diagonal_start])+4+n_matrix_rows:
                matrix[count,count] = content_list[i + n_indices]
                count += 1

      #Part that determines the diagonal positions and writes them to the matrix
        #1) Determine the values that lie between diagonals
        #2) Determine the corresponding values
      #3) Write the values to the correct positions in the matrix (+mirror positions)
        count = 0
```

```
        for i in range(0,n_matrix_rows):
            k_start = int(content_list[i+Diagonal_start])
            k_end = int(content_list[i+Diagonal_start+1])
            ind_start = k_start + index_start
            ind_end = k_end + index_start -2


            if ind_start <= ind_end:
                for stepper in range(ind_start,ind_end+1):
                    value = stepper + values_start - (index_start)
             print(i,int(content_list[stepper])-1,stepper,value,content_list[value])
               matrix[i,int(content_list[stepper])-1] = content_list[value]

                    #Mirroring the off-diagonals
               matrix[int(content_list[stepper])-1,i] = content_list[value]


        print(”Matrix assembled!”)

#%% Check whether the diagonals are filled

    if symmetric in ”yes”:
        count_nz = 0
        for i in range(len(matrix)):
            if matrix[i,i] != 0:
                count_nz += 1
        if count_nz == n_matrix_rows:
            print(”Diagonals are all filled”)
        else:
            print(”Error: A diagonal value is zero”)



#%% Contribution of the mapping file
# In this part the contribution from the mapping file is added to the assembled matrix
#

    # Determine matrix row/column names
    if mapping != None:
        current_mapping_file = open(mapping,”r”)
        content_mapping = current_mapping_file.read()
        content_mapping_list = content_mapping.splitlines()

        mapping_node_dof = []
        for i in range(1,n_matrix_rows+1):
            node_dof = content_mapping_list[i].split()
            mapping_node_dof.append(node_dof)
        mapping_node_dof = np.array(mapping_node_dof)

        column_names = []
        for i in range(len(mapping_node_dof)):
         name =”Node ” +  mapping_node_dof[i,1] + ” ” + mapping_node_dof[i,2]
            column_names.append(name)
        column_names = np.array(column_names)

        matrix = pd.DataFrame(matrix, column_names, column_names)
```

```
    else:
        matrix = pd.DataFrame(matrix)

    return(matrix)



if __name__ == ’__main__’:

     ”””Test case for the hb_read function which reads the test Harwell-
Boeiing file K.txt and the mapping file K.mapping”””

    thisdir = Path(__file__).parent

    file = thisdir / ”static/test_data/K.txt”
    mapping = thisdir / ”static/test_data/K.mapping”
    df = hb_read(file, mapping)
```

D

Detailed flowchart numerical method

In this appendix an in-depth flowchart describing the steps taken in the numerical method is provided, see Figure D.1.

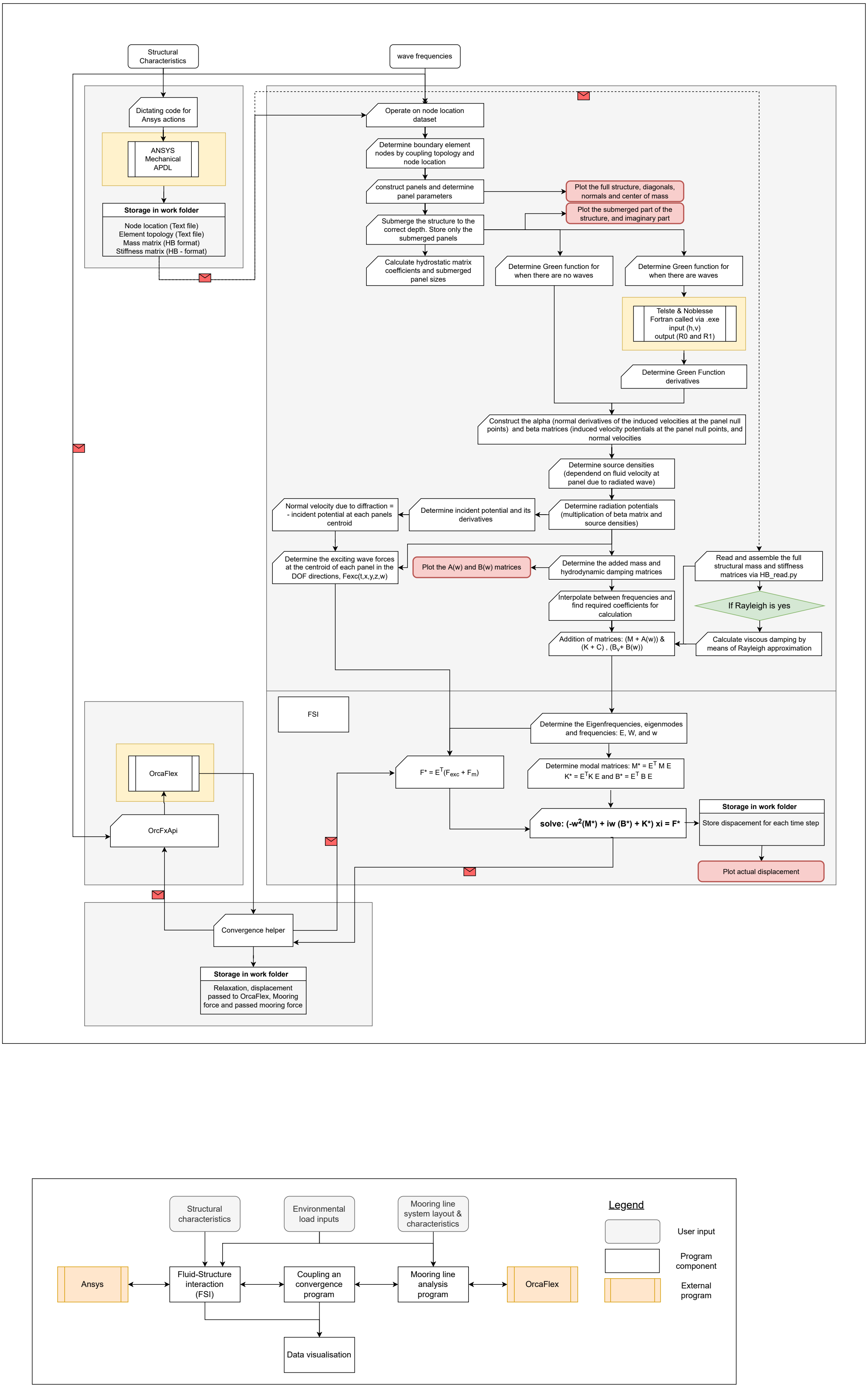

Figure D.1: Full method flowchart

References

[1] Ansys. *Solid 186*. URL: `https://www.mm.bme.hu/~gyebro/files/ans_help_v182/ans_elem/Hlp_E_SOLID186.html`. accessed: 20-06-2021.

[2] R. Bischop and W. Price. *Hydroelasticity of ships*. Cambridge University Press, 1979.

[3] R. Bishop, W. Price, and Y. Wu. "A general linear hydroelasticity theory of floating structures moving in a seaway". In: vol. 316, No.1538. Philosophical transactions of the Royal society of London. Apr. 1986. eprint: `https://www.jstor.org/stable/37612`.

[4] J. M. Blackledge. *Digital Image Processing*. Chichester, West Sussex: Horwood Publishing, 2005.

[5] X. Chen. "Hydrodynamics in Offshore and Naval Applications – Part I". In: vol. All Days. 6th International Conference on HydroDynamics. 2004.

[6] B. Chu, Y. Chen, Y. Zhang, G. Zhang, X. Xiang, and X. Zhang. "Numerical study on wave-induced hydro-elastic responses of a floating raft for aquaculture". In: *Ocean Engineering* 240 (2021), p. 109869. ISSN: 0029-8018. DOI: `https://doi.org/10.1016/j.oceaneng.2021.109869`. URL: `https://www.sciencedirect.com/science/article/pii/S0029801821012191`.

[7] COMSOL. *Rayleigh Damping*. URL: `https://doc.comsol.com/5.5/doc/com.comsol.help.sme/sme_ug_modeling.05.083.html`. (accessed: 09.01.2022).

[8] Comsol. *Mode superposition*. URL: `https://www.comsol.com/multiphysics/mode-superposition`. accessed: 02-03-2022.

[9] L. de Vries. *Communications on OrcaFlex and OrcFxAPI*. accessed: 11-11-2021.

[10] European Commision. *Communication from the Commission to the European Parliament, the European Council, the Council, the European Economic and Social Committee and the Committee of the Regions. The European Green Deal COM/2019/640 final*. URL: `https://eur-lex.europa.eu/legal-content/EN/TXT/?qid=1588580774040&uri=CELEX%5C%3A52019DC0640`. (accessed: 09.01.2022).

[11] O. M. Faltinsen. "Wave Loads on Offshore Structures". In: *Annual Review of Fluid Mechanics* 22.1 (1990), pp. 35–56. DOI: `https://10.1146/annurev.fl.22.010190.000343`. URL: `https://doi.org/10.1146/annurev.fl.22.010190.000343`.

[12] O. M. Faltinsen and F. C. Michelsen. *Motions of Large Structures in Waves at Zero Froude Number*. Det Norske Veritas, 1975.

[13] Frankfurt school-UNEP Centre/BNEF. *Global trends in renewable energy investment 2020.* URL: `https://www.fs-unep-centre.org/wp-content/uploads/2020/06/GTR_2020.pdf`. (accessed: 09.01.2022).

[14] C. Gerald and P. Wheatley. *Applied Numerical Analysis*. Featured Titles for Numerical Analysis. Pearson/Addison-Wesley, 2004. ISBN: 9780321133045. URL: `https://books.google.nl/books?id=BiOZQgAACAAJ`.

[15] git. *git – everything-is-local*. URL: `https://git-scm.com/`. accessed: 18-03-2022.

[16] A. Guha and J. Falzarano. "Development of a computer program for three dimensional analysis of zero speed first order wave body interaction in frequency domain". In: *International Conference on Offshore Mechanics and Arctic Engineering*. Vol. 55393. American Society of Mechanical Engineers. 2013, V005T06A094.

[17] J. Hess and A. Smith. "Calculation of potential flow about arbitrary bodies". In: *Progress in Aerospace Sciences* 8 (1967), pp. 1–138. ISSN: 0376-0421. DOI: `https://doi.org/10.1016/0376-0421(67)90003-6`. URL: `https://www.sciencedirect.com/science/article/pii/0376042167900036`.

[18] J. L. Hess. *A Higher Order Panel Method for Three-dimensional Potential Flow*. 1979.

[19] J. L. Hess and A. M. O. Smith. "Calculation of Nonlifting Potential Flow About Arbitrary Three-Dimensional Bodies". In: *Journal of Ship Research* 8.04 (Sept. 1964), pp. 22–44. ISSN: 0022-4502. DOI: `10.5957/jsr.1964.8.4.22`. eprint: `https://onepetro.org/JSR/article-pdf/8/04/22/2232748/sname-jsr-1964-8-4-22.pdf`. URL: `https://doi.org/10.5957/jsr.1964.8.4.22`.

[20] T. Humamoto and K. Fujita. "Wet-Mode Superposition For Evaluating the Hydroelastic Response of Floating Structures With Arbitrary Shape". In: International Ocean and Polar Engineering Conference. May 2002. eprint: `https://onepetro.org/ISOPEIOPEC/proceedings-pdf/ISOPE02/All-ISOPE02/ISOPE-I-02-044/1878951/isope-i-02-044.pdf`.

[21] D. V. Hutton. *Fundamentals of finite element analysis*. New York, United States of America: McGraw Hill, 2004.

[22] J. M. J. Journée and W. W. Massie. *Offshore Hydromechanics*. Delft, The Netherlands: Delft University of Technology, 2001, pp. 7–44.

[23] M. Kashiwagi. "A B-Spline Galerkin Scheme for Calculating the Hydroelastic Response of a Very Large Floating Structure in Waves". In: *Journal of Marine Science and Technology* 3.1 (1998), pp. 37–49.

[24] M. Kashiwagi. "A Direct Method Versus a Mode-Expansion Method For Calculating Hydroelastic Response of a VLFS In Waves". In: vol. All Days. International Ocean and Polar Engineering Conference. ISOPE-I-98-034. May 1998. eprint: `https://onepetro.org/ISOPEIOPEC/proceedings-pdf/ISOPE98/All-ISOPE98/ISOPE-I-98-034/1933497/isope-i-98-034.pdf`.

[25] J. T. Katsikadelis. *Boundary Elements. Theory and Applications*. Amsterdam, the Netherlands: Elsevier, 2002, pp. XIV+336. ISBN: ISBN-10: 0080441076.

[26] J. Katz and A. Plotkin. *Low-Speed Aerodynamics*. Cambridge, United Kingdom: Cambridge University, 2001.

[27] C. H. Kim. *Nonlinear Waves and Offshore Structures*. WORLD SCIENTIFIC, 2008. DOI: `10.1142/4906`. eprint: `https://www.worldscientific.com/doi/pdf/10.1142/4906`. URL: `https://www.worldscientific.com/doi/abs/10.1142/4906`.

[28] H. Lamb. *Hydrodynamics*. Cambridge, UK: Cambridge University Press, 1994.

[29] E. Loukogeorgaki, C. Michailides, and D. Angelides. ""Dry" and "wet" mode superposition approaches for the hydroelastic analysis of floating structures". In: June 2014.

[30] H. Maeda and T. Ikoma. *Numerical Models in Fluid-Structure Interaciton*. Delft, The Netherlands: WIT Transactions of State of the Art in Science and Engineering, 2005, pp. 7–44.

[31] H. Maeda, S. Miyajima, K. Masuda, and T. Ikoma. "Hydroelastic responses of pontoon type very large floating offshore structure". In: (Dec. 1996). URL: `https://www.osti.gov/biblio/449685`.

[32] S. Malenica and X. Chen. "On the Irregular Frequencies Appearing In Wave Diffraction-Radiation Solutions". In: *International Journal of Offshore and Polar Engineering* 8 (Jan. 1998).

[33] K. McTaggart and Defence R & D Canada - Atlantic. *Three Dimensional Ship Hydrodynamic Coefficients Using the Zero Forward Speed Green Function*. Technical memorandum. Defence R & D Canada - Atlantic, 2002. URL: `https://books.google.nl/books?id=8AMTDAEACAAJ`.

[34] W. H. Munk. *Origin and Generation of Waves*. ASCE, 1950.

[35] S. Nagata, H. Yoshida, and H. Isshiki. "The analysis of the wave-induced responses of an elastic floating plate". In: *Proceedings of 16th of the International Conference on Offshore Mechanics and Arctic Engineering - OMAE 6* (1997), pp. 163–169.

[36] NemoEng. *Floating solar power plant*. URL: `http://nemoeng.com/eng/surface/`. accessed: 22-02-2022.

[37] J. N. Newman. *Marine Hydrodynamics*. 40th ed. MIT Press, 2018. eprint: `https://mitpress.mit.edu/contributors/j-n-newman`. URL: `https://mitpress.mit.edu/contributors/j-n-newman`.

[38] NOS nieuws. *Systeem van zonnepanelen op water getest: ’Het beweegt mee met de golven’*. URL: `https://nos.nl/video/2407492-systeem-van-zonnepanelen-op-water-getest-het-beweegt-mee-met-de-golven`. accessed: 24-02-2022.

[39] Ocean Sun. *Benefits*. URL: `https://oceansun.no/benefits/`. accessed: 22-02-2022.

[40] S. Ohmatsu. “Numerical Calculation of Hydroelastic Responses of Pontoon type VLFS”. In: *Journal of the Society of Naval Architects of Japan* 1997.182 (1997), pp. 329–340. DOI: `10.2534/jjasnaoe1968.1997.182_329`.

[41] S. Oliveira-Pinto and J. Stokkermans. “Assessment of the potential of different floating solar technologies – Overview and analysis of different case studies”. In: *Energy Conversion and Management* 211 (2020), p. 112747. ISSN: 0196-8904. DOI: `https://doi.org/10.1016/j.enconman.2020.112747`. URL: `https://www.sciencedirect.com/science/article/pii/S0196890420302855`.

[42] Orcina. *General data: Implicit integration*. URL: `https://www.orcina.com/webhelp/OrcaFlex/Content/html/Generaldata,Implicitintegration.htm`. accessed: 09-01-2022.

[43] Orcina. *Lines*. URL: `https://www.orcina.com/webhelp/OrcaFlex/Content/html/Lines.htm`. accessed: 10-01-2022.

[44] Orcina. *OrcaFlex documentation*. URL: `https://www.orcina.com/resources/documentation/`. accessed: 09-01-2022.

[45] Orcina. *Rayleigh Damping: Guidance*. URL: `https://www.orcina.com/webhelp/OrcaFlex/Content/html/Rayleighdamping,Guidance.html`. (accessed: 09.01.2022).

[46] Orcina. *Theory: Irregular frequencies*. URL: `https://www.orcina.com/webhelp/OrcaWave/Content/html/Theory,Irregularfrequencies.htm`. accessed: 21-01-2022.

[47] Orcina. *Wind Spectra*. URL: `https://www.orcina.com/webhelp/OrcaFlex/Content/html/Windspectra.htm`. accessed: 20-01-2022.

[48] Orcina. *World-leading software from a world class company*. URL: `https://www.orcina.com`. accessed: 08-03-2022.

[49] B. Ponizy, F. Noblesse, M. Ba, and M. Guilbaud. “Numerical Evaluation of Free-Surface Green Functions”. In: *Journal of Ship Research* 38.03 (Sept. 1994), pp. 193–202. ISSN: 0022-4502. DOI: `10.5957/jsr.1994.38.3.193`. eprint: `https://onepetro.org/JSR/article-pdf/38/03/193/2231047/sname-jsr-1994-38-3-193.pdf`. URL: `https://doi.org/10.5957/jsr.1994.38.3.193`.

[50] QuickFEM. *IFEM*. URL: `https://quickfem.com/wp-content/uploads/IFEM.Ch31.pdf@online`. accessed: 31-03-2022.

[51] SEMAR. *Analysis of floating flexible fish cages with ORCAFLEX/PYTHON*. URL: `https://semar.no/wp-content/uploads/2017/10/SEMAR-AS-Analysis-of-floating-fish-farms-september-2017_General.pdf`. accessed: 09-01-2022.

[52] I. Senjanović, M. Tomic, N. Vladimir, and N. Hadžić. “An Analytical Solution to Free Rectangular Plate Natural Vibrations by Beam Modes – Ordinary and Missing Plate Modes”. In: *Transactions of FAMENA* 40 (Nov. 2016), pp. 1–18. DOI: `10.21278/TOF.40301`.

[53] B. Sliz-Szkliniarz. “Assessment of the renewable energy-mix and land use trade-off at a regional level: a case study for the Kujawsko–Pomorskie Voivodship”. In: *Land Use Policy* 35 (2013), pp. 257–270. DOI: `https://dx.doi.org/10.1016/j.landusepol.2013.05.018`.

[54] SolarisFloat. *The solution*. URL: `https://www.solarisfloat.com/the-solution/`. accessed: 22-02-2022.

[55] Spyder. *Spyder: the scientific python development environment*. URL: `https://www.spyder-ide.org/`. accessed: 12-01-2022.

[56] H. Suzuki, H. Riggs, M. Fujikubo, T. Shugar, H. Seto, Y. Yasuzawa, B. Bhattacharya, D. Hudson, and H. Shin. “Very Large Floating Structures”. In: vol. 2. Oct. 2007, paper OMAE2007–29758. DOI: `10.1115/OMAE2007-29758`.

[57] H. Suzuki, H. Riggs, M. Fujikubo, T. Shugar, H. Seto, Y. Yasuzawa, B. Bhattacharya, D. Hudson, and H. Shin. “Very Large Floating Structures”. In: vol. 2. Oct. 2007, paper OMAE2007–29758. DOI: `10.1115/OMAE2007-29758`.

[58] M. Takaki and X. Gu. “Motions of a Floating Elastic Plate in Waves (2nd Report)”. In: *Journal of the Society of Naval Architects of Japan* 1997.181 (1997), pp. 103–109. DOI: `10.2534/jjasnaoe1968.1997.103`.

[59] H. Tavana and M. Khanjani. “Reducing Hydroelastic Response of Very Large Floating Structure: A Literature Review”. In: *International Journal of Computer Applications* 71 (June 2013), pp. 13–17. DOI: `10.5120/12353-8658`.

[60] Z. Tay and C. M. Wang. “Reducing hydroelastic response of very large floating structures by altering their plan shapes”. In: *Ocean Systems Engineering* 2.1 (2012), pp. 61–81. DOI: `10.12989/OSE.2012.2.1.069`.

[61] G. team. *GCC, the GNU Compiler collection*. URL: `https://gcc.gnu.org/`. accessed: 23-03-2022.

[62] B. U. of technology and Economics. *ANSYS Mechanical APDL command Reference - BME-MM*. URL: `https://www.mm.bme.hu/~gyebro/files/ans_help_v182/ans_cmd/Hlp_C_CmdTOC.html`. accessed: 14-03-2022.

[63] J. G. Telste and F. Noblesse. “Numerical Evaluation of the Green Function of Water-Wave Radiation and Diffraction”. In: *Journal of Ship Research* 30.02 (June 1986), pp. 69–84. ISSN: 0022-4502. DOI: `10.5957/jsr.1986.30.2.69`. eprint: `https://onepetro.org/JSR/article-pdf/30/02/69/2230444/sname-jsr-1986-30-2-69.pdf`. URL: `https://doi.org/10.5957/jsr.1986.30.2.69`.

[64] D. Turnkey and V. Fthenakis. “Environmental impacts from the installation and operation of large-scale solar power plants”. In: *Renewable and Sustainable Energy Reviews* 15 (2011), pp. 3261–3270. DOI: `https://dx.doi.org/10.1016/j.rser.2011.04.023`.

[65] United Nations. *Paris Agreement*. URL: `https://unfccc.int/sites/default/files/english_paris_agreement.pdf`. (accessed: 09.01.2022).

[66] S. van Hoof. *Hydroelastic wave deformation of very flexible floating structures*. URL: `http://resolver.tudelft.nl/uuid:6652a9ee-61a6-4c4a-9b28-ef4fda1010f9`. accessed: 24-03-2022.

[67] B. Veritas. *Offshore Standard DNV-OS-FS201*. URL: `https://rules.dnv.com/docs/pdf/DNVPM/codes/docs/2010-10/Os-F201.pdf`. (accessed: 09.01.2022).

[68] S. Viswanathan, C. Holden, O. Egeland, and M. Greco. “An Open-Source Python-Based Boundary-Element Method Code for the Three-Dimensional, Zero-Froude, Infinite-Depth, Water-Wave Diffraction-Radiation Problem”. In: *Modeling, Identification and Control* 42.2 (2021), pp. 47–81. DOI: `10.4173/mic.2021.2.2`.

[69] C. M. Wang, E. Watanabe, and T. Utsunomiya. *Very Large Floating Structures*. New York, United Stated of America: Taylor and Francis, 2008, pp. 59–60.

[70] Wassee. *Solid vs. Shell vs Solid-Shell Elements*. URL: `https://featips.com/2021/02/21/solid-vs-shell-vs-solid-shell-elements/`. accessed: 18-03-2022.

[71] E. Watanabe, T. Utsunomiya, and C. Wang. “Hydroelastic analysis of pontoon-type VLFS: a literature survey”. In: *Engineering Structures* 26.2 (2004), pp. 245–256. ISSN: 0141-0296. DOI: `https://doi.org/10.1016/j.engstruct.2003.10.001`. URL: `https://www.sciencedirect.com/science/article/pii/S0141029603002256`.

[72] Y. Watanabe. “VLFS’96”. In: vol. 25-28. Proceedings of international workshop on Very Large Floating Structures. Oct. 1996. eprint: `https://repository.tudelft.nl/islandora/object/uuid:e2e8a787-2791-42fa-9b67-9c6816b98b34/`.

[73] J. V. Wehausen. “The Motion of Floating Bodies”. In: *Annual Review of Fluid Mechanics* 3.1 (1971), pp. 237–268. DOI: `10.1146/annurev.fl.03.010171.001321`. URL: `https://doi.org/10.1146/annurev.fl.03.010171.001321`.

[74] Wikipedia. *Programming language*. URL: `https://en.wikipedia.org/wiki/Programming_language`. accessed: 20-03-2022.

[75] Wikipedia. *Very large floating structure*. URL: `https://en.wikipedia.org/wiki/Very_large_floating_structure`. accessed: 14-03-2022.

[76] K. Yago and H. Endo. "Model Experiment and Numerical Calculation of the Hydroelastic Behavior of Mat-Like VLFS". In: *VLFS'96* 1996 (1996), pp. 209–214.

[77] Y. Yasuzawa, K. Kagawa, D. Kawano, and K. Kitabayashi. "Dynamic response of a large flexible floating structure in regular waves". In: *Ocean Space Utilization*. Vol. 6. Proceedings of the 1997 16th International Conference on Offshore Mechanics and Arctic Engineering. Part 1-B (of 6) ; Conference date: 13-04-1997 Through 17-04-1997. ASME, 1997, pp. 187–194.